315557
132 p

Investigation of Next-Generation Earth Radiation Budget Radiometry

Final Report
NASA Grant NAG-1-2094

Submitted To:

Robert B. Lee III
Radiation Sciences Branch
Atmospheric Sciences Division
National Aeronautics and Space Administration
Hampton, Virginia 23685

By:

Professor J. R. Mahan
Department of Mechanical Engineering
Virginia Polytechnic Institute and State University
Blacksburg, Virginia 24061

July 28, 1999

ACKNOWLEDGEMENTS

I would like to begin by expressing my most sincere thanks to my advisor, Dr. J. R. Mahan, for the opportunities that he has provided for my personal and professional growth, and for his unwavering encouragement and enthusiasm. My time as his student and research assistant has been a true pleasure for me.

A special thanks to Dr. Kory J. Priestley for his willingness to make time in his demanding schedule to serve as my mentor in NASA's LARSS program, for his ample help in completing the work presented in this thesis, and for his refreshing sense of humor and perspective.

I would also like to thank Dr. Curtis H. Stern for his willingness to serve on my committee.

I would also like to gratefully recognize the financial support of this research by NASA's Langley Research Center under Grant NAG-1-2094.

A special thanks to my friends: Félix Nevárez, whose help has been instrumental in the completion of this research, and to Ben Hall who has been with me through it all.

I thank my wonderful family for their constant love and support. They have always made success as easy as following in their footsteps.

Thanks especially to my fiancé, Juan, for standing behind my every decision, and for his abundant optimism, encouragement, and love.

Above all, thanks be to God, from whom all blessings flow.

(Signed) Katherine L. Coffey, November 30, 1998

NEXT-GENERATION EARTH RADIATION BUDGET INSTRUMENT CONCEPTS

Katherine L. Coffey

(ABSTRACT)

The current effort addresses two issues important to the research conducted by the Thermal Radiation Group at Virginia Tech. The first research topic involves the development of a method which can properly model the diffraction of radiation as it enters an instrument aperture. The second topic involves the study of a potential next-generation space-borne radiometric instrument concept.

Presented are multiple modeling efforts to describe the diffraction of monochromatic radiant energy passing through an aperture for use in the Monte-Carlo ray-trace environment. Described in detail is a deterministic model based upon Heisenberg's uncertainty principle and the particle theory of light. This method is applicable to either Fraunhofer or Fresnel diffraction situations, but is incapable of predicting the secondary fringes in a diffraction pattern. Also presented is a second diffraction model, based on the Huygens-Fresnel principle with a correcting obliquity factor. This model is useful for predicting Fraunhofer diffraction, and can predict the secondary fringes because it keeps track of phase.

NASA is planning for the next-generation of instruments to follow CERES (Clouds and the Earth's Radiant Energy System), an instrument which measures components of the Earth's radiant energy budget in three spectral bands. A potential next-generation concept involves modification of the current CERES instrument to measure in a larger number of wavelength bands. This increased spectral partitioning would be achieved by the addition of filters and detectors to the current CERES geometry. The capacity of the CERES telescope to serve for this purpose is addressed in this thesis.

TABLE OF CONTENTS

List of Tables

List of Figures

1.0 Introduction

2.0 Efforts to monitor global climate change

3.0 Problems in optics

4.0 Modeling diffraction in the Monte-Carlo ray-trace environment

5.0 Next generation instrument concepts

6.0 Conclusions and recommendations

LIST OF TABLES

LIST OF FIGURES

1.0 INTRODUCTION

The Earth/atmosphere system is evolving due to human activities and to natural events. The IPCC (Intergovernmental Panel on Climate Change) has concluded that "the balance of evidence suggests a discernible human influence on global climate through emissions of carbon dioxide and other greenhouse gases" [IPCC, 1997]. Activities such as deforestation, construction, biomass burning, and agricultural and industrial activities, as well as volcanic eruptions, all alter the composition of the Earth/atmosphere system by changing the planetary reflectance, adding aerosols to the atmosphere, and increasing and altering atmospheric gases. The Earth's environment has been polluted as never before in the past century, and various independent measurements indicate that the Earth's temperatures are changing, although how much is not exactly known. Burroughs [1997] reports that there has been a general warming trend of between 0.3 and 0.6 ° C in the Earth's meteorological temperature throughout the twentieth century; most of this change concentrated in the period between 1920 to 1940 and since the mid-1970's. Discrepancies exist between satellite and terrestrial measurements of Earth's temperatures, and it is always possible that some of the detected changes may be attributed to the advances in measurement devices rather than truly being due to actual changes in the Earth's temperatures. Finally, the possibility exists that observed changes are a natural part of the behavior of the dynamic Earth/atmosphere system. We approach the end of the twentieth century with more questions than answers with regard to the health of our planet. Scientists continue in the search for answers to the myriad questions about some of the most challenging issues that have ever faced our planet.

There is no question that human activity has altered the composition of the Earth's atmosphere. Human activity has sent huge quantities of pollutants such as carbon monoxide, sulfur dioxide, nitrogen oxides, hydrocarbons, and particulate matter into the atmosphere. Scientists have observed many notable changes in atmospheric gases in the second half of this century. Stratospheric ozone, important for its ability to absorb ultraviolet solar energy thus shielding the Earth, is being depleted due to human activity such as the emission of nitrous oxide and chlorofluororcarbons. One study conducted at Mauna Loa Observatory in Hawaii showed that the concentration of carbon dioxide in the atmosphere has increased by about 10 percent since 1958. Using the evidence of air bubbles trapped in polar ice, and recent observations such as those at Mauna Loa, some scientists estimate that the atmospheric concentration of carbon dioxide has increased by up to 25 percent since the early 1800's. Although there are other sources of atmospheric carbon dioxide (i.e. the decay of vegetation and volcanic eruptions), it is believed that the major culprit is the burning of fossil fuels [Ahrens, 1992]. These are but a few of the various upsets to the balance of the Earth/atmosphere system brought on by human activity.

Other evidence found in ice cores, as described by Burroughs, sways opinion in an opposite direction and adds weight to the intriguing question of how much detected changes are truly a result of human activity. These ice cores, taken from the Greenland ice sheet, reveal a history of huge fluctuations in the Earth's climate that occurred independent of man's influence. The ice cores show that the climate has been fairly stable over the past 10,000 years, but during previous years, as far back as 100,000 years ago, a picture of a highly erratic climate emerges. Assuming that the detected upward trend of less than one degree Celsius measured over this past century is an accurate figure, the earlier changes revealed by the ice cores were five to ten times greater, and occurred over only a few years rather than over the span of a century. The evidence revealed by these Greenland ice cores has provided a new perspective in climatic thinking. Where it was previously believed that big changes in climate could only occur over a long period of time due to the thermal inertia of the oceans, it is now conceivable that the climate could undergo huge shifts in short periods of time. Because of such recent discoveries, some climatologists believe that these natural fluctuations must be strongly considered in the study of global warming. As emphasized by Burroughs, without a better understanding of the extent of past natural climatic change it is not realistic to plan on the basis that current changes are the consequence of human activities.

The detected slight rise in the Earth's temperature, the fact that the activities of mankind are altering the Earth's environment as never before, and the knowledge that the Earth's climate has undergone dramatic changes in the past independent of man's influence, all combine to pose a unique challenge to the science community in determining whether the current warming is linked to human activities, or is the result of natural mechanisms in the climate. In the quest for answers to these questions, some of the most useful tools are GCMs, or Global Circulation Models, which can be used to study cause-and-effect scenarios in the Earth/atmosphere system [Wielicki, *et al.*, 1995]. GCMs are computer models that mathematically model the extremely complex physics of the Earth/atmosphere system. These models incorporate many approximations and simplifications, and there is much room for improvement as many unknowns still exist. The importance of GCMs which can yield trustworthy conclusions as to the cause/effect of global warming is paramount. Information revealed by these GCMs is used by organizations such as the IPCC (Intergovernmental Panel on Climate Change), which serves to assess scientific information about climate change relevant for the formulation of international and national policy. Because of their importance, there is much interest in the refinement of GCMs. Refinement can be accomplished by utilizing findings from continued studies of the Earth/atmosphere system.

National and international efforts are being made to address these uncertainties. NASA's most recent contribution to these efforts is the Mission to Planet Earth, which is part of the United States Global Change Research Program (USGCRP). This research effort consists of a series of space-based remote sensing platforms, the largest of which is the Earth Observing System (EOS) [Anon, 1993]. EOS involves a series of Earth-orbiting satellites containing a variety of instruments designed to provide critical global observations of the Earth/atmosphere system, computing facilities, and science researchers, and is committed to data collection for at least a 15-year period. The EOS system is particularly effective, because a single satellite contains multiple instruments measuring many independent physical processes that can be observed simultaneously for a given scene type. Chapter 2.0 describes several NASA instruments, the measurements that they are used to obtain, and the data products they provide. This will serve as background to describe the current research effort. Figure 1.1 summarizes the many interrelated factors involved in the study of global warming and climate change.

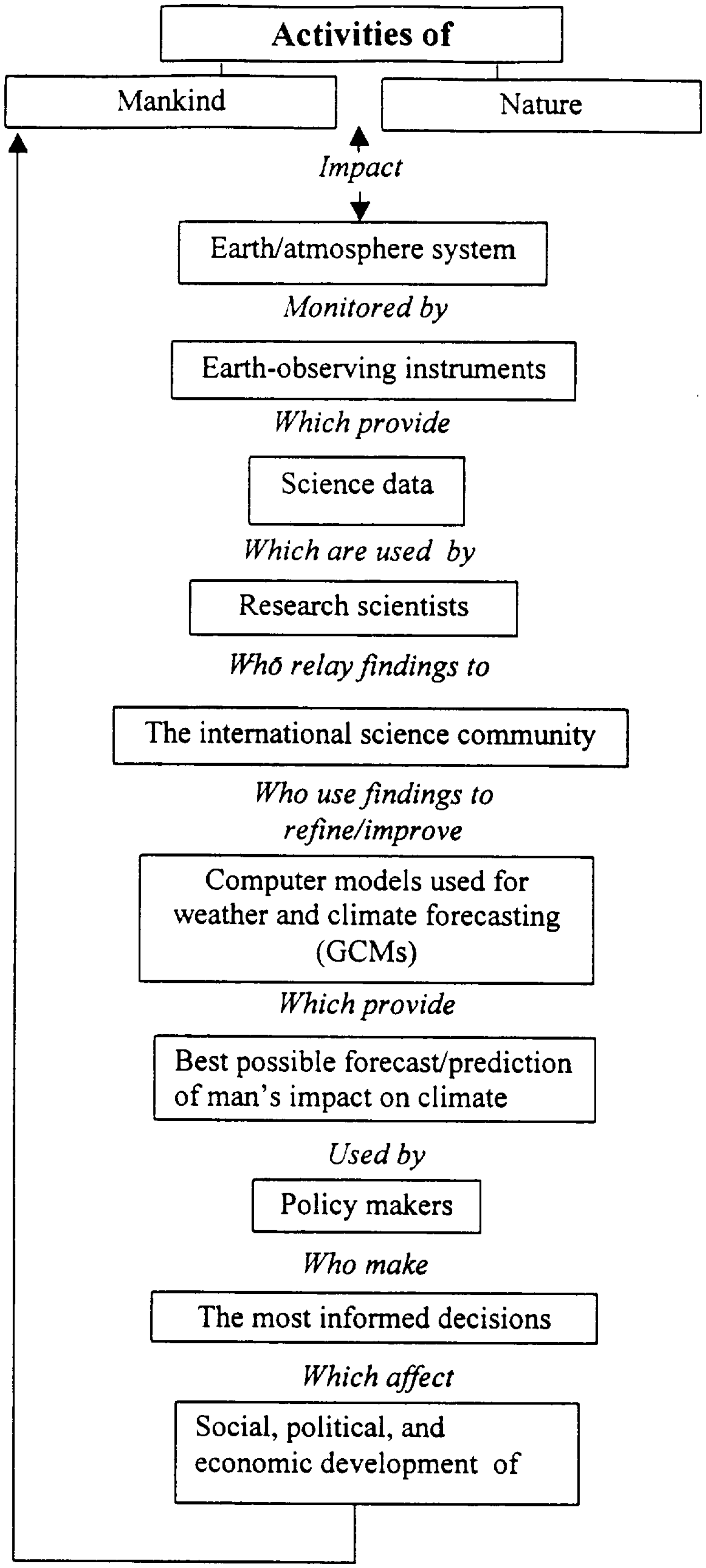

Figure 1.1 Factors involved in the study of global warming and climate change.

2.0 EFFORTS TO MONITOR GLOBAL CLIMATE CHANGE

2.1 The Earth radiation budget

Averaged over the entire Earth and over the span of a year, the sun delivers approximately 340 W/m^2 of shortwave radiation. Approximately 99 percent of this energy is below 3.8 μm, with one percent below 0.3 μm. Of the arriving solar energy, about 30 percent, or 100 W/m^2, is reflected back into space. This reflected energy is called the Earth's albedo. The solar energy which is not reflected back into space (240 W/m^2) is absorbed by the Earth/atmosphere, which heats up and emits longwave radiation. The Earth's temperatures currently range between approximately 240-300 K with 99 percent of its emitted energy at wavelengths longer than 4.6 μm and only two percent above 60-70 μm [Lenoble, 1993]. Ahrens [1992] explains that "Earth's temperature" can mean a variety of things. For instance, the Earth's observed average surface temperature is about 288 K. On the other hand, if Earth is viewed as behaving as a blackbody, where it absorbs solar radiation and emits infrared radiation at equal rates, its radiative equilibrium temperature is approximately 255 K. Thus care should be taken when reporting and interpreting changes in the "Earth's temperature".

Since the solar and terrestrial radiation are present in wavelength bands which barely overlap, the two can be measured separately. By subtracting the total emitted and total reflected energy from the solar contribution, the net radiation budget, or the net amount absorbed by the Earth at a given time and location can be computed. If the net amount at a given time and location is positive that particular area of the Earth tends to warm, whereas if the net is negative that area cools. This spatial variation in temperature is what drives the weather of our planet. If this difference is averaged temporally and spatially, the net radiation budget is approximately zero. However, if some disturbance (due to human activity or to natural events) were to occur which disturbed this equilibrium, a time-dependent climate change would occur, and the temperature of the Earth would change (increase or decrease) until radiative balance was once again established. One of the goals of Earth-observing instruments is to determine whether this sort of imbalance is occurring, and if so, to identify its causes. One of the steps in this process is to measure the parameters necessary to derive the global net radiation energy budget.

2.2 Earth-observing instruments

The use of satellites is an especially effective measurement method in the quest for the answers to the fundamental question of whether the temperatures of the Earth are changing, as they can provide global coverage and thus make measurements used to derive the global TOA (Top-of-the-Atmosphere) radiant energy budget. Satellite-based observation began in the early 1960's with the onset of the Space Age, and has continued ever since.

As the generations of Earth-observing instruments have developed, they have served in the continued gathering of data initiated by previous instruments, in making increasingly advanced measurements and in using increasingly sophisticated algorithms in data reduction. As with most improvements there are trade-offs, as these upgrades do not come without a price. In the process of replacing one instrument with another having greater capability, the organization leading the investigation risks the disturbance of the collection of continuous science data. Detected changes in measurements which may be due to the transition in instruments could be misinterpreted as changes in the Earth's energy budget. This risk is minimized as much as possible, and instruments are replaced as the motivations for improvement outweigh the risks. To help minimize risk, new-generation and past-generation instruments' missions are made to overlap so that calibrations can be transferred, if at all possible. Instrument improvement is achieved by using the lessons learned from previous missions, and the progressive state of knowledge about the Earth/atmosphere system that reveals data products which may be more useful. Change is also motivated by the organization's desire to stay atop the latest technology. In the case of the National Aeronautics and Space Administration, change is often driven by the fact that "NASA Headquarters and Administration appear to want to view NASA as technology developers rather than scientific leaders" [Barkstrom, 1998]. So for various reasons, the push is on to conduct successful experiments using state-of-the-art technology and to gather useful information that can be used to advance our knowledge about the Earth/atmosphere system while planning constantly for the future generations of instruments to be used to monitor our planet. At the same time, Earth-observing experiments must continue to gather a complementary set of data throughout the generations of instruments so that the studies are sufficiently long-term to monitor change over the decades.

2.3 Earth-observing instruments leading to the current research effort

2.3.1 ERBE

In 1979, the National Aeronautics and Space Administration began ERBE (the Earth Radiation Budget Experiment), a mission that was to measure the most basic parameters in monitoring the Earth's climate. ERBE was launched aboard the NASA ERBS (Earth Radiation Budget Satellite) in 1984, and aboard NOAA-9 and NOAA-10 in 1984 and 1986. The ERBE instrument is a scanning thermistor bolometer radiometer consisting of three channels sensitive in the short (0.2-5.0 μm), the long (5.0-50 μm) and the total (0.2-100 μm) wavelength bands. The principal goals of this mission were to measure broadband radiances at the Top-of-the-Atmosphere (TOA), to convert these anisotropic radiances to TOA fluxes using Angular Distribution Models (ADMs) and the Maximum Likelihood Estimation (MLE) technique [Wielicki and Green, 1989], and to derive the global TOA radiation energy budget. ERBE collected thirteen years of data, and provided what NASA calls the most accurate data of the Earth's outgoing longwave and solar reflected shortwave radiation ever obtained, as well as answers to some long-standing questions about climate forcing and feedback mechanisms in the Earth/atmosphere system. Among these important findings, ERBE data showed that the annual average effect of clouds is to cool the current climate system. This did not, however, end the debate as to whether clouds act to decrease global warming. "A common misconception is that because clouds cool the present climate, they will likewise act to moderate global warming. What is actually important is the change in the net cloud radiative forcing, associated with a change in climate, that governs cloud feedback" [Weilicki *et al.*, 1995]. In the process of answering questions, these answers prompted further questions and the next generation of instruments evolved. The insight into the influence of clouds gained by ERBE data served as a basis for naming the monitoring of clouds and their influence on the Earth's radiant energy system as a top priority in the next generation of instruments, CERES.

2.3.2 CERES

The Clouds and the Earth's Radiant Energy System (CERES) is a suite of broadband scanning radiometers based on the ERBE instrument, but featuring many improvements [Wielicki, 1996; Bongiovi, 1993; Haeffelin, 1996; Priestley, 1997; Smith, 1998]. The CERES instrument incorporates full two-dimensional directional sampling by scanning in both elevation and in azimuth angle. It includes the same short and total wavelength channels of ERBE, but the longwave channel was replaced by a "window" channel, sensitive in the region of 8.0-12.0 μm. The first CERES instrument, the PFM (Proto-Flight Model), was launched in late 1997 aboard TRMM (Tropical Rainfall Measuring Mission), as part of NASA's Earth Observing System (EOS). Two more CERES instruments are scheduled to be launched aboard the spacecraft EOS-AM and EOS-PM in the late 1990's and the beginning of the 21st century, and these and follow-on instruments will extend measurements for a total of fifteen years. CERES data will serve to extend the thirteen years of ERBE data by measuring broadband radiances at the top of the atmosphere which will be converted to TOA fluxes. The CERES Pathfinder Project was organized to analyze CERES data products and to "bridge the gap" between ERBE and CERES missions. In addition to TOA fluxes, more sophisticated parameters are being determined. The CERES instruments fly on satellites containing cloud imagers that make simultaneous measurements of the same scene being viewed by CERES. CERES data are being used with this cloud imager data to infer surface fluxes and to provide the vertical profile of radiative divergence. Data collected during CERES azimuthal rotations is being used to build angular distribution models (ADMs), striving to meet the mission goals to reduce the ADM errors by a factor of four over ERBE. CERES is expected to provide TOA fluxes that are two to three times more accurate than those of ERBE data [Wielicki *et al.*, 1996]. Over the course of the development and launch of CERES, and with the use of CERES science data, NASA has identified the desirable features of the next generation of instruments. In summer, 1998, NASA outlined these features and named this potential future instrument, PERSEPHONE.

2.3.3 PERSEPHONE

NASA developed the preliminary conceptual design of PERSEPHONE under the criterion that the next-generation instrument be smaller, less resource intensive, less costly, and requires less build time. In the spirit of these requirements, and in the continued quest for the understanding of climate forcing and feedback mechanisms, NASA has identified increased spectral partitioning of radiance as the principal feature of this potential next-generation instrument. This partitioning will involve dividing the measured energy into a larger number of spectral bands rather than simply measuring in the shortwave, total, and window channels as in ERBE and CERES. Since radiant energy is spectrally and spatially altered as it passes through the Earth/atmosphere system before arriving at the detector, and since most atmospheric constituents and surface properties are selective absorbers (i.e. they strongly affect radiation in limited spectral regions), measurement of energy in these narrower spectral bands will yield a deeper understanding of our Earth's climate system [Barkstrom, *et al.*, 1998].

In order to achieve the goal of refined spectral partitioning while keeping cost at a minimum, NASA has proposed that the current CERES telescope be modified to serve several detectors. Each detector would measure energy in a different spectral band by placing the desired filters in its optical path. While expanding the capability of the current CERES telescope, NASA wishes to improve the calibration accuracy and spatial and angular sampling capability while maintaining the current envelope of size, mass, and electrical power. In addition, NASA wishes to maintain the same (or better) quality of the Optical Point Spread Function (OPSF) on all detectors as that of the current CERES telescope. The OPSF describes the radiation throughput to the detector as a function of the angle at which collimated radiation enters into the instrument. These concepts will be described more thoroughly in Chapter 5.0.

Modification of the CERES telescope to meet the criterion outlined above creates new challenges that will require the state-of-the-art in technology to overcome. Barkstrom, *et al.* [1998] identify the three most serious challenges that must be overcome in order for this redesign to succeed. The first issue involves the need for an increase of detector sensitivity by more than an order of magnitude over the current CERES detector since the redesign calls for the division of energy into smaller spectral intervals. The other two issues involve the need to isolate the different spectral bands without loss of calibration accuracy, and the need for calibration sources for the narrower spectral intervals.

In addition to these issues, a redesign of the optics may be required in order to achieve an approximately uniform radiative flux over all detectors. One of the topics of research for the current master's thesis involves the determination of whether a redesign is required, and if so, further study of a potential optical prescription that will yield acceptable performance.

2.4 The Thermal Radiation Group

The Thermal Radiation Group of the Mechanical Engineering Department at Virginia Tech has been involved in the numerical modeling of Earth-observing instruments since the early 1970's, in addition to other research projects. Much of this work was funded under NASA grants, in support of the work done by the Radiation Sciences Branch, Atmospheric Sciences Division of NASA Langley Research Center. Under the direction of Dr. J. R. Mahan, master's and Ph.D. students of the Thermal Radiation Group have worked to develop high-level, dynamic, electrothermal, end-to-end numerical models of both ERBE and CERES instruments. These models are capable of simulating the response of these instruments to simulated Earth scenes [Haeffelin, *et al.*, 1997]. The end-to-end models include an optical/thermal-radiative module and a thermistor bolometer dynamic electrothermal module. The optical/thermal-radiative module is used to model the optics of the instrument using the Monte-Carlo ray-trace (MCRT) method as it applies to radiation heat transfer. The output from this module is then used as input to the second electrothermal module, a finite-difference or finite-element code characterizing the electrothermal behavior of the detector to various inputs.

In addition to this work, over the course of the past few years a Ph.D. student in the Thermal Radiation Group, Félix Nevárez, has been developing a flexible, ray-trace-based numerical tool that can be used to build the radiative model of any instrument. In the past, students have built a highly specific code for the instrument at hand, such as those described for the CERES and ERBE instruments. This new tool brings with it the capability to build in a matter of weeks what could have taken up to several years using previous capabilities. The optical prescription for the PERSEPHONE instrument has been studied using this tool.

In addition to this topic of investigation, the author has investigated an entirely separate issue, the proper modeling of diffraction of radiant energy as it enters an instrument as treated in the Monte-Carlo ray-trace environment. This issue is important in many of the computer modeling efforts conducted by the Thermal Radiation Group, but has been neglected in the past. It is believed that a higher level of sophistication in the modeling of diffraction will benefit modeling efforts by future generations of students of the Thermal Radiation Group.

2.5 Goals of the current research

The goals of the current research effort are to:

1. Develop a radiative model of the CERES instrument using the new ray-trace tool being developed in the Thermal Radiation Group. This model will be used to:
    - serve as validation of the new ray-trace tool by comparing results to results from a previous radiative model and experimental results.
    - study the current CERES telescope to determine whether changes will be required for the successful implementation of the multiple detector concept for potential next-generation instruments.
    - investigate a new optical prescription which may better serve the needs of the proposed next-generation instrument concepts.
2. Investigate the importance of the modeling of diffraction of radiant energy as it enters instruments of the type modeled by the Thermal Radiation Group.
3. Investigate, develop, and test means of numerically modeling diffraction in the Monte-Carlo ray-trace environment.

3.0 PROBLEMS IN OPTICS

Much of the work done by the Thermal Radiation Group involves the development of radiative models of radiometric instruments. The Monte-Carlo ray-trace (MCRT) method is generally used, but the design objectives vary with the measurements being sought. For instance, the design of a solar aureolemeter used to measure the concentration and size distribution of atmospheric aerosols is a continuing topic of investigation in the Thermal Radiation Group. This is an imaging instrument that measures the circumsolar radiation pattern produced by atmospheric aerosols. These measurements are important because the scattering produced by aerosols in the region around the sun is much greater than that due to other atmospheric constituents. The image quality is of principle concern in the design of this instrument [Deepak and Adams 1983; Nakajima, *et al.*, 1983]. On the other hand, the CERES instrument is not an imaging instrument, but a radiometer. Energy throughput, rather than the image quality, is the principle concern in the design of this instrument. As described by Walkup [1996], the area in which the two disciplines of imaging and radiometry merge is imaging radiometry, illustrated in Figure 3.1. This best describes the type of investigations conducted within the Thermal Radiation Group.

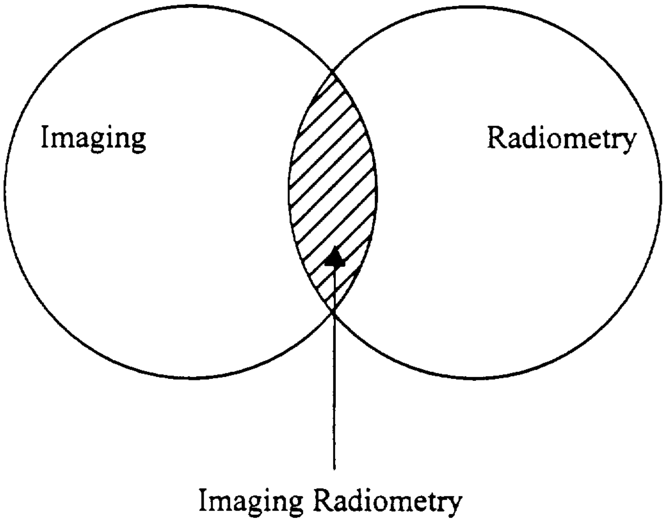

Figure 3.1 Combination of imaging and radiometry disciplines, (borrowed from Walkup [1996]).

3.1 Ideal versus real behavior in optical systems

Much of the work presented in this thesis in some way pertains to the deviation of the true performance of instruments from simplified models of their ideal behavior. The ideal behavior of optical systems is often called Gaussian optics. This first-order theory is used for preliminary design specifications, and can be used for mirror placement and for locating the ideal image point in an optical system. Gaussian optics describes a point-to-point, object-to-image relationship. That is, when rays leave a point within the object plane, they will arrive at a single point in the image plane. True optical performance of instruments deviates from this idealized behavior. The degree of this deviation can be described by five different aberrations: spherical aberration, coma, astigmatism, field curvature, and distortion. For the purposes of the current effort, it is important to describe spherical aberration in an optical system. For a detailed description of the other aberrations, refer to Walkup [1996].

3.1.1 Spherical aberration

Spherical aberration is the only aberration that occurs on-axis. Because of this aberration, rays reflected from conic reflectors do not converge to the ideal infinitely small spot size as they cross the optical axis at the Gaussian image plane. Instead, a blur circle of finite size is formed at the focal plane. Rays that traverse the telescope near the optical axis behave ideally, passing through the Gaussian image point, while those reflecting far from the optical axis do not. The point at which this blur circle is a minimum is called the "circle of least confusion," as illustrated in Figure 3.2. It is important in the design and assembly of an imaging telescope that this circle of least confusion fall in the detector plane. For a non-imaging telescope such as CERES, the telescope is assembled such that the circle of least confusion is located at the plane containing the precision aperture that serves to shape the image cast on the detector beneath.

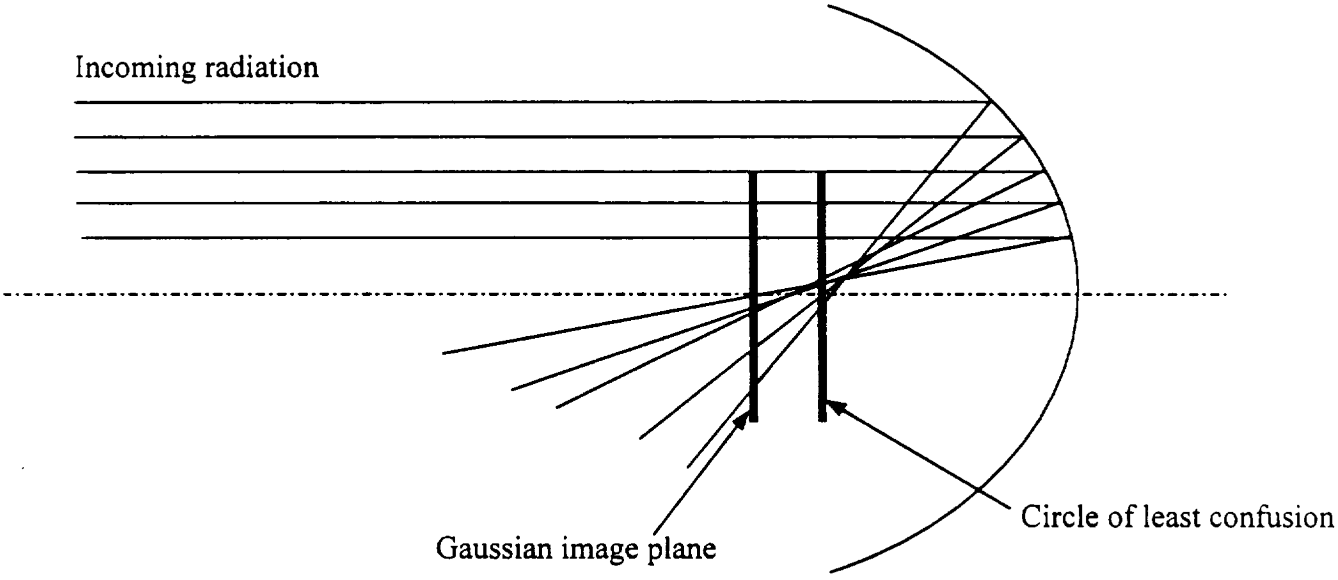

Figure 3.2 Illustration of spherical aberration (borrowed from Walkup [1996]).

3.2 Ideal versus real propagation of electromagnetic waves

The idealized behavior of the propagation of electromagnetic energy is sometimes referred to as the ideal ray approximation. This model ignores diffraction, and rays are modeled as straight lines that are perpendicular to the propagating wavefronts. As electromagnetic waves enter apertures or pass by obstacles, the ideal ray approximation does not account for diffraction effects that are known to occur. The correction of this idealization in instrument modeling is a major topic of this thesis. The following discussion of diffraction serves to provide the necessary background for understanding the work presented in Chapter 4.0.

3.2.1 Diffraction

3.2.1.1 Basic ideas

Diffraction and interference are actually one and the same: the constructive and destructive interference of in-phase or out-of-phase waves arriving at the same point. The convention has developed to call this additive wave property *interference* when it deals with only a few waves, and to call it *diffraction* when it involves many waves [Hecht and Zajac, 1974]. Diffraction occurs when electromagnetic waves pass through apertures or past obstacles, causing the waves to deviate from their original lines of travel. The degree to which this divergence occurs depends upon the wavelength of the entering radiation relative to the aperture dimensions. For the case where the wavelength of the approaching wave is much less than the aperture dimensions, diffraction effects are slight. In this case, the ideal ray approximation is valid. The resulting intensity on an observation screen placed behind the aperture is in the shape of a top hat, with no light arriving outside the area which is formed by the projection of the aperture area on the screen. This case is illustrated in Figure 3.3 (a). When the wavelength of the light is on the order of the aperture size, diffraction effects are more pronounced as shown in Figure 3.3 (b). If the entering energy is monochromatic, a pattern of alternating minima and maxima will form on an observation screen placed behind the aperture. Energy will spread out to areas that would be predicted to be in shadow by the ideal ray approximation. The shape and span of the resulting diffraction pattern depends on the aperture size, the wavelength of the entering energy, and the distance between the observation screen and the aperture. Finally, when the wavelength of the approaching energy is much greater than the aperture dimensions, the aperture behaves as a point source that emits spherical waves, (i.e. a slit behaves as a line of point sources) as illustrated in Figure 3.3 (c). In this case, the energy will spread out in the region where a shadow would be predicted, but no pattern of maxima and minima will be observed.

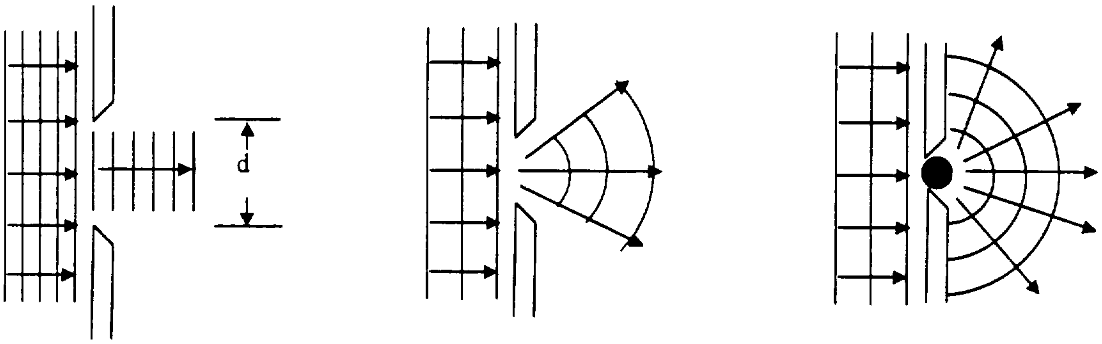

$\lambda << d$ $\lambda \approx d$ $\lambda >> d$

(a) (b) (c)

Figure 3.3 The behavior of radiation as it passes through an infinite slit: (a) the wavelength of entering radiation is much less than the slit width, (b) the wavelength is approximately equal to the slit width, and (c) the wavelength is much greater than the slit width (borrowed from Serway [1994]).

The diffraction models that are presented in Chapter 4.0 are used to simulate the behavior of monochromatic, coherent radiant energy as it passes through an aperture, and the results are compared to closed-form analytical solutions of the expected interference pattern for validation. Upon validation, these models will then be used to simulate diffraction for cases in which the approaching energy is neither coherent nor monochromatic. Such is the case for applications such as instruments used to measure the Earth's radiation energy budget.

3.2.1.2 The two diffraction regimes

Diffraction can be classified into two regimes: Fresnel, or near-field, and Fraunhofer, or far-field, diffraction. Fraunhofer diffraction occurs when the light source and the observation screen upon which the diffraction pattern is observed are both effectively at infinite distances from the aperture causing the diffraction. Fresnel diffraction occurs when either (or both) the source or the screen are at finite distances from the aperture. In the development of a radiative model of an instrument, one must determine how crucial the modeling of diffraction is. The first step in this assessment is to determine which of the two diffraction regimes governs the diffraction. For the case in which energy is entering through a rectangular slit, and the source is at infinity, the parameter

$$\Delta\xi = a\left(\frac{2}{\lambda z}\right)^{\frac{1}{2}}, \tag{3.1}$$

where a is the slit width, z is the distance between the aperture and the observation screen, and λ is the wavelength of the entering energy, is used for the purpose of categorizing diffraction as Fraunhofer or Fresnel [Wyatt, 1987; Haskell, 1970]. $\Delta\xi = 1$ is taken to be the transitional configuration between the two regimes. For cases in which $\Delta\xi > 1$, Fresnel diffraction prevails, while for cases in which $\Delta\xi < 1$, Fraunhofer diffraction prevails. Figure 3.4 illustrates this transition, brought on by moving the observation screen away from the aperture. In this case, the point source is at infinity with respect to the slit. As the observation screen is moved away from the aperture, the rays become approximately parallel upon their arrival at the observation screen, meeting the criterion for Fraunhofer diffraction. Note that a similar transition would occur if the wavelength of the entering radiation were increased while holding the parameters z and a constant. Such is the case in the practical application presented in Chapter 4.0.

The diffraction patterns shown in Figure 3.4 are based on the closed-form analytical solution reported by Haskell [1970]. The intensity along the screen is given in terms of the Fresnel integrals

$$C(u) = \int_0^u \cos\left[\frac{1}{2}\pi u^2\right] du, \tag{3.2 a}$$

and

$$S(u) = \int_0^u \sin\left[\frac{1}{2}\pi u^2\right] du, \tag{3.2 b}$$

and the parameters

$$\xi_1 = \frac{1}{2}\Delta\xi[(\xi_o / \Delta\xi) - 1], \tag{3.3}$$

$$\xi_2 = \frac{1}{2}\Delta\xi[(\xi_o / \Delta\xi) + 1], \tag{3.4}$$

where $\Delta\xi$ is as defined in equation 3.1 and

$$\xi_o = -2x\left(\frac{2}{\lambda z}\right)^{\frac{1}{2}}. \tag{3.5}$$

Thus the intensity along an observation screen, as illustrated in Figure 3.4 is given by

$$I(x) = \frac{1}{2}[C(\xi_2) - C(\xi_1)]^2 + \frac{1}{2}[S(\xi_2) - S(\xi_1)]^2. \tag{3.6}$$

Equation 3.6 can be used to determine diffraction patterns in either the Fresnel or Fraunhofer regime. However, Fraunhofer diffraction can be described by simplified equations found in Laufer [1996].

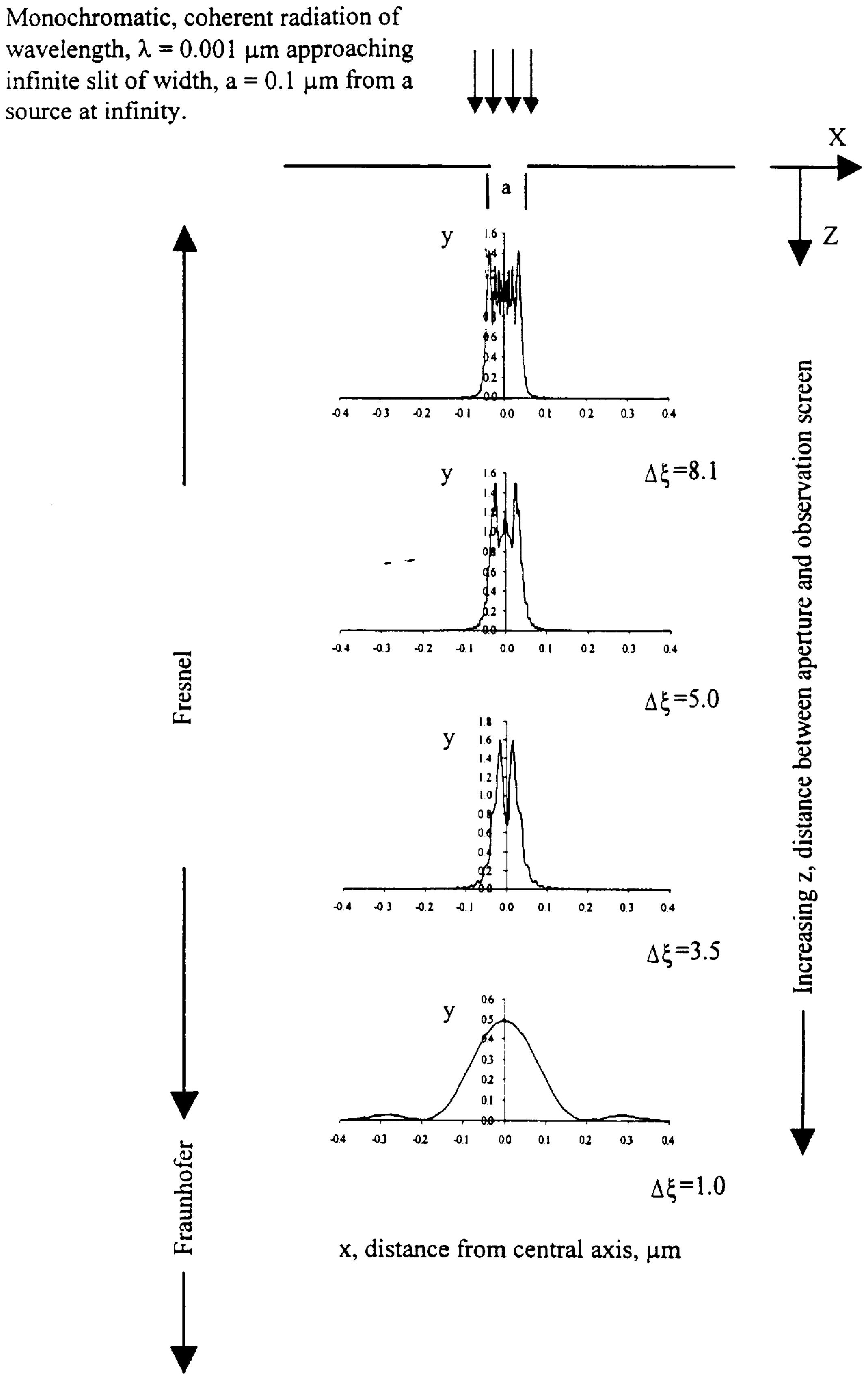

Monochromatic, coherent radiation of wavelength, λ = 0.001 μm approaching infinite slit of width, a = 0.1 μm from a source at infinity.

Figure 3.4 Illustration of the transition from Fresnel to Fraunhofer diffraction and the resulting change in the intensity distribution, I(x) where y = I(x)

Table 3.1 summarizes the characteristics of the two diffraction regimes. The modeling capabilities mentioned refer to the models that are presented in Chapter 4.0.

Table 3.1 Comparing characteristics of Fraunhofer and Fresnel diffraction.

Fraunhofer	**Fresnel**
♦ Far-field	♦ Near-field
♦ Simpler analytical solutions.	♦ Complex analytical solutions.
♦ Instrument throughput not good.	♦ Instrument throughput good.
♦ Possibility of modeling phase using new ray-trace approach (Model 2) and MCRT method.	♦ Cannot model phase using MCRT method.
♦ Good modeling is more important, ideal ray trace deviates greatly from actual behavior (Figure 3.5 (a)).	♦ Good modeling is not always as important, ideal ray trace approximates the true behavior well in very near field (Figure 3.5 (b)).

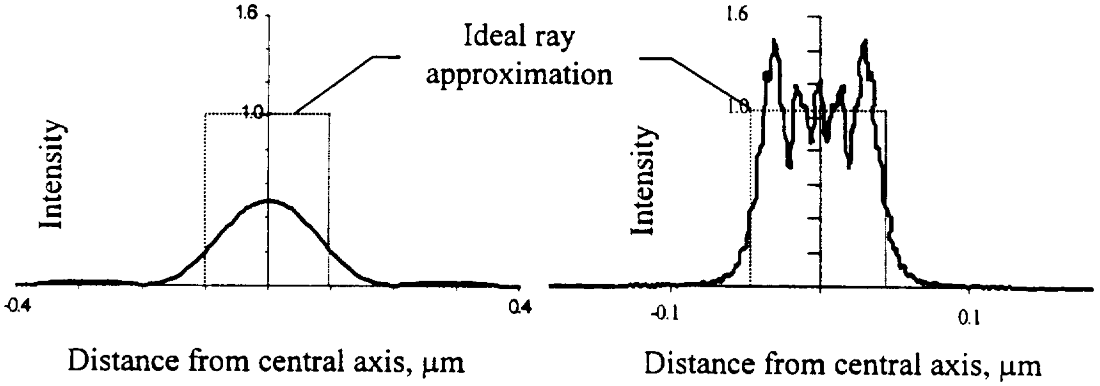

(a) (b)

Figure 3.5 Illustration of the deviation of the ideal ray approximation from the true intensity pattern resulting from the passage of energy through a slit 0.1 μm wide (a) for a Fraunhofer diffraction situation, and (b) for a Fresnel diffraction situation.

Figures 3.5 (a) and (b) illustrate the importance of modeling diffraction well in the Fraunhofer regime, and the reduced importance of modeling diffraction well in the

Fresnel regime. Because energy is distributed far into the geometrical shadow in Fraunhofer cases, much of the on-axis energy is dispersed out of the optical path. For this reason, Fraunhofer diffraction is generally avoided in imaging systems. Ideally, an effort should be made to ensure that diffraction occurs in the Fresnel region in the early design stages of an instrument [Wyatt, 1987].

3.2.1.3 A brief history of diffraction

The diffraction of electromagnetic waves has puzzled and challenged scientists, engineers and physicists for more than five centuries, and some of these challenges remain even today. The authors of most optics and physics books state that diffraction is one of the most complicated problems to be dealt with in optics. Diffraction is of academic importance, as it serves as evidence of the wave nature of light. It is of practical significance to engineers and scientists as it limits the resolving power of optical devices, and often results in less than ideal instrument throughput.

Challenges posed by the phenomenon of diffraction are interwoven throughout the history of optical science. Every generation of scientists since the 1400s has made a contribution to further our understanding of diffraction. The following briefly summarizes the stages of diffraction knowledge, borrowing from the historical summary by Hecht and Zajac [1974], and other authors. Throughout this historical summary, many important principles are described which serve as background for the diffraction models presented in Chapter 4.0.

The first reference to the phenomena of diffraction was made in the work of Leonardo Da Vinci (1452-1519). It was not until 1665 that diffraction was accurately described by Professor Francesco Maria Grimaldi in his observations of bands of light within the shadow of a rod illuminated by a small source [Born, 1970]. Soon after, Robert Hooke (1635-1703) performed experiments in which he also observed diffraction patterns. These observations of diffraction prompted the beginning of the wave theory of light, and the great debate as to whether light is corpuscular (stream of particles) or wave-like. Christian Huygens (1629-1695), a proponent of the wave theory, continued to extend the wave theory of light. One of his significant contributions, Huygens' principle which states that "every point on a primary wavefront serves as the source of spherical secondary wavelets such that the primary wavefront at some later time is the envelope of these wavelets" is illustrated in Figure 3.6 (a). This model, which treats the secondary wavelets as radiating equally in all directions, and the envelope of the wavelets as the intensity at an observation screen behind the aperture, is unable to predict the expected interference pattern due to the diffraction of energy. It also predicts a backward propagating wave, which is not observed in reality. Thomas Young (1773-1829) was the next important contributor to the wave theory of light despite ridicule from many of his colleagues who supported the corpuscular theory. Young provided the first clear demonstration of the wave nature of light in 1801. His double slit experiment showed that light coming from a single source, arriving at a point by two separate paths, combines both constructively and destructively, resulting in an interference pattern on an observation screen placed behind the two slits, as illustrated in Figure 3.6 (b).

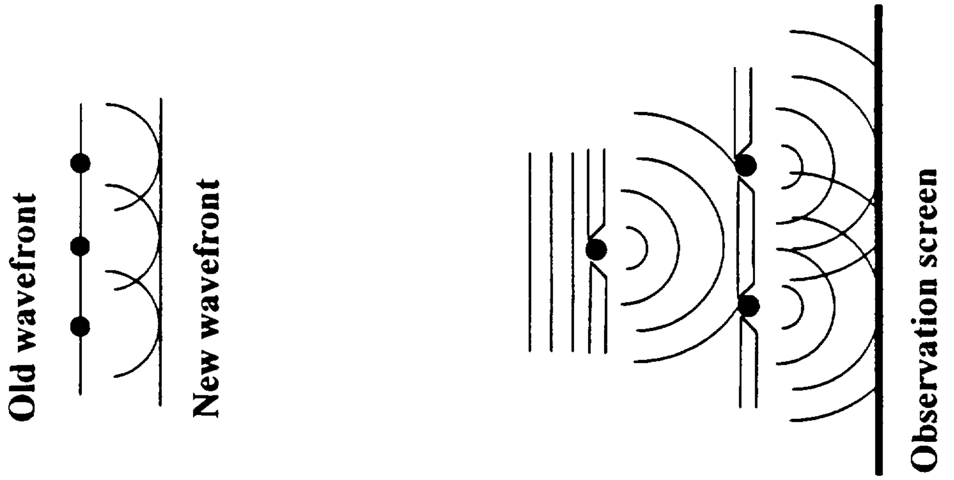

(a) (b)

Figure 3.6 (a) Illustration of Huygens' principle for plane waves propagating to the right (excluding the backwards-propagating wave), and (b) illustration of Young's double-slit experiment.

Augustin Jean Fresnel (1788-1827) added to Huygens' ideas in order to provide a model which could predict the intensity variations expected by diffracted energy. He added an undefined angular dependence factor, K, called the obliquity factor, which serves to model the directionality of the emission of secondary wavelets coming from a point source. The Huygens-Fresnel principle states that "every unobstructed point of a wavefront, at a given instant in time, serves as a source of secondary wavelets of the same frequency as the primary wave. The amplitude of the optical field at any point beyond is the superposition of all of these wavelets (considering their amplitudes and relative phases)". Fresnel began to describe diffraction on a mathematical basis and was able to predict diffraction patterns of light when it passed by obstacles. Kirchoff was the first to put the conceptual Huygens-Fresnel principle on a more mathematical basis, proposing a specific form of the obliquity factor, K which is used in Chapter 4.0. Instead of conceptual arguments to describe diffraction phenomena, mathematical descriptions began to be sought and used more extensively. The determination of an exact solution for a particular diffracting configuration is amongst the most difficult to be dealt with in optics [Hecht and Zajac, 1974]. The first such solution was published in 1896 by Arnold Sommerfeld (1868-1951). This solution utilized the electromagnetic theory of light, and involved an infinitely thin, opaque, perfectly conducting plane screen. Note that rigorous solutions such as the one published by Sommerfeld exist for very few configurations of practical interest today. Because of this, numerical methods based on conceptual diffraction models and other approximations are often used to determine the effect of diffraction on configurations of interest.

3.2.1.4 Modern methods of dealing with diffraction

A number of methods for modeling and/or characterizing diffraction in an optical instrument have been developed in this century, taking advantage of advancements in computing power. Some of these methods are described briefly in the following paragraphs, and references are cited which provide more extensive details.

Airy disk construction

Circular baffles, apertures, or obscurations are quite common in optical systems. For such configurations, the importance of diffraction in their optical performance can be approximated by a simple calculation. The size of the diffraction blur or Airy disk, named in honor of British mathematician, Lord George Biddell Airy (1801-1892), is given by

$$D_1 = 2.44\,\lambda\,f\,, \tag{3.7}$$

where D_1 is the diameter of the diffraction blur, λ is the wavelength of the entering energy, and f is the focal length of the optical system divided by the aperture diameter [Riedl, 1997]. For the case of energy entering through a circular aperture, D_1 defines the area on the observation screen containing 84 percent of the incident energy, assuming no other aberrations are present. The diameter, D_2, which defines the area that will contain 91 percent of the incident energy is given by

$$D_2 = 4.48\,\lambda\,f\,. \tag{3.8}$$

It is important to note in instrument design that there is no point in decreasing the diffraction blur size below the size of the blur circle due to the geometrical aberrations present in the optical system. Likewise, an optical system can never perform better than the limits that are predicted by diffraction, thus optical designers may reach a point where further minimization of geometrical aberrations would be in vain. Another important situation, a circular aperture with a central obscuration, is commonly found in telescopes such as CERES. Details of the treatment of this situation are provided by Riedl [1997] and by Walker [1998]. Note that the addition of a circular obscuration in the center of a circular aperture causes the incident energy to become more dispersed, thus the Airy disk diameters are larger. The degree of this dispersion of energy out of the desired optical path depends on the diameter of the obscuration relative to the diameter of the aperture, characterized by the percent obscuration. The larger the percent obscuration, the more the incident energy is dispersed. For this reason, systems with obscurations greater than 50 percent are rarely used [Walker, 1998]. For further discussions regarding the influence of diffraction on instrument imaging performance, the interested reader is referred to Braun [1970], Tschunko and Sheehan [1971], and Boivin [1977].

Method of moments

The method of moments can be used to approximate the diffraction pattern of energy entering an aperture. This method, based on the method of weighted residuals, is a common tool within the electrical engineering culture, and can be applied to treat the propagation of electromagnetic waves of any wavelength. For details of this method see Hubing [1991]. Graves *et al.* [1976] address the modeling of the electromagnetic field penetration through a circular aperture in both the near and far field using this method. Results are shown to compare well with theory.

Geometrical theory of diffraction

The geometrical theory of diffraction provides a means of supplementing standard geometric optics with the ability to model diffraction. Keller [1957, 1962] and Balanis and Peters [1968] published descriptions and sample applications of this method, which treats diffraction as an edge effect, as originally proposed by Thomas Young [Keller, 1962]. In addition to the usual rays, the geometric theory of diffraction introduces new diffracted rays which originate as a ray strikes an edge or vertex. As an example of the application of this method, the treatment of radiation as it enters an aperture is described by Keller [1957, 1962]. Rays which strike an edge become diffracted rays. When the incident ray is normal to the edge, the diffracted rays produced are also normal to the edge (i.e. all lie in the same plane), and leave in all directions within that plane, as shown in Figure 3.7 (a). When waves approach the edge obliquely, the diffracted wave fronts are defined by cones emanating from the edge, as illustrated in Figure 3.7 (b). These obliquely diffracted rays follow the *law of edge diffraction*, which states that a diffracted ray and the corresponding incident ray make equal angles with the edge at the point of diffraction. The incident and diffracted rays lie on opposite sides of the plane normal to the edge at the point of diffraction [Keller, 1962]. All rays are assigned an initial phase upon their arrival to the aperture opening, and their final phase upon arrival to an observation screen is proportional to the optical length of a ray from this point. Keller [1957, 1962] and Balanis and Peters [1968] demonstrate good agreement when comparing results from the application of the geometrical theory of diffraction with the closed-form analytical solution of the expected diffraction pattern for several cases.

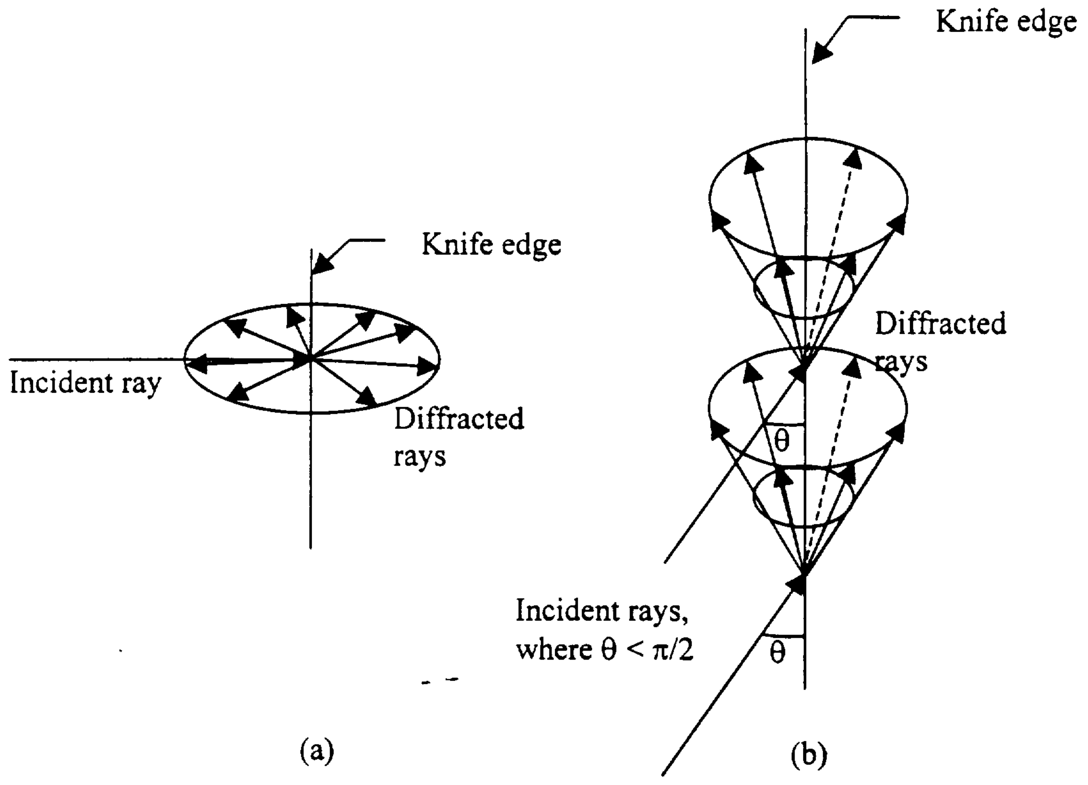

Figure 3.7 Illustration of the formation of diffracted rays, (a) when an incident ray strikes perpendicular to the edge, and (b) when incident rays strike the edge obliquely (borrowed from Keller [1962]).

The geometrical theory of diffraction was implemented in the GUERAP II code, a computer program for the analysis of the stray radiation rejection capabilities of optical systems, as briefly described by Boyce [1977]. A subsequent version of this code, GUERAP III, replaced the use of this methodology with a newer technique, referred to in this thesis as the statistical method for dealing with diffraction [Morbey and Hutchings, 1993].

Statistical method for dealing with diffraction

This method is based upon Heisenberg's uncertainty principle and the particle theory of light, and is convenient for use in the Monte-Carlo ray-trace environment [Chou, 1974]. This approach does not keep track of phase, so the resulting pattern approximates the minima and maxima which occur alongside the central maxima. Heinsch and Chou [1971] and Likeness [1977] briefly describe the concepts of this approach, omitting most of the details necessary for its implementation. The details needed for the application have been rediscovered by the author of this thesis and are discussed at length in Chapter 4.0.

Use of Huygens' principle to model diffraction

The use of Huygens' principle to model an aperture as many point sources emitting isotropically in all directions has been implied by a technique described by Sinnott [1987]. The diffraction pattern resulting from the passage of starlight through a telescope is desired. The Monte-Carlo technique is applied, sending random parallel rays through the telescope. Ray path lengths are determined upon their arrival at an observation screen, and the net phase at a given point is given by the sum of the phase of all rays arriving at that point. Results are given as a two-dimensional scattergram, and are shown to compare qualitatively with analytical results (i.e. the spatial distribution of energy compares with the expected diffraction distribution). Results are not, however, quantitatively compared with theory (i.e. comparison of the relative magnitude of secondary maxima to central maxima is not made). Further discussion and modification of this technique are proposed in Chapter 4.0.

4.0 MODELING DIFFRACTION IN THE MONTE-CARLO RAY-TRACE ENVIRONMENT

In the Theory of Heat Radiation, Max Plank [1959] states that "so far as their physical properties are concerned, heat rays are identical with light rays of the same wavelength". His book, which contains much of the basis upon which modern radiation heat transfer is based, does not consider the phenomenon of diffraction "on account of its complicated nature". Plank goes on to say "[i]t will be assumed that the linear dimensions of all parts of space considered, as well as the radii of curvature of all surfaces under consideration, are large compared with the wavelengths of the rays considered. With this assumption we may, without appreciable error, entirely neglect the influence of diffraction caused by the bounding surfaces, and everywhere apply the ordinary laws of reflection and refraction of light". Many of the instruments modeled by the Thermal Radiation Group do not adhere to this restriction, rather some of the instrument dimensions are on the order of the wavelength of the entering radiation. In such cases, general methods used to model radiation heat transfer must be supplemented with some means of dealing with diffraction in the development of the complete radiative model of an instrument.

Much of the work done in the Thermal Radiation Group involves the development of radiative models of instruments using the Monte-Carlo ray-trace (MCRT) method. This is a statistical approach which simulates the behavior of radiant energy as it enters and passes through an instrument. A complete description of this method can be found in Walkup [1996]. To model radiant energy as it enters an instrument in the MCRT environment, the entering energy is divided into a large number of discrete energy bundles. These bundles are fired uniformly and randomly into the aperture. For example, for the case of a rectangular aperture with corner coordinates of (X_o,Y_o) and width and length (W,L), illustrated in Figure 4.1, a given energy bundle will enter at location $X=X_o+R_xL$, $Y=Y_o+R_yW$, where R_x and R_y are random numbers uniformly distributed between 0 and 1. Up to this point, radiative models created in the Thermal Radiation Group ignored diffraction effects and the entering energy bundles were directed parallel into the instrument and treated as collimated energy. It is desirable to develop a means of modeling the true behavior of this radiation as it enters and passes through the instrument. This proper modeling of the diffraction of radiant energy as it enters radiometric instruments is addressed in this chapter by presenting two candidate modeling approaches.

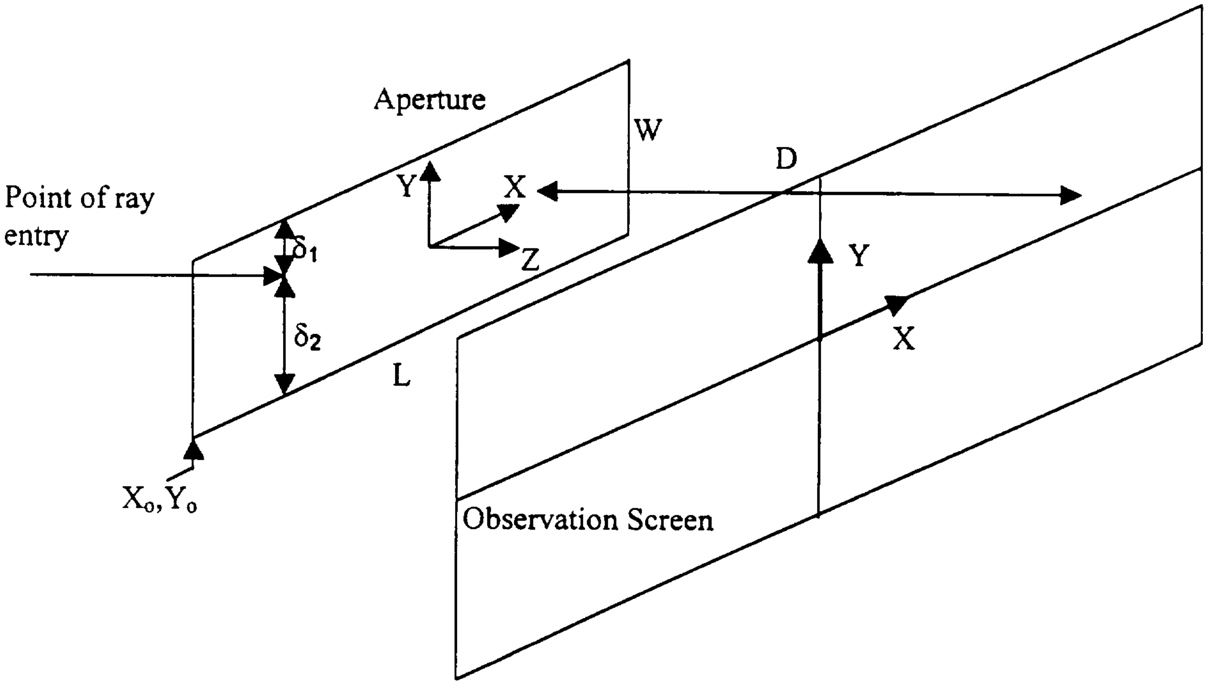

Figure 4.1 Illustration of physical parameters important to the description of the statistical model of diffraction.

4.1 Model 1: The statistical approach

The statistical approach to modeling diffraction was originally published by Heinisch and Chou [1971], and later modified and republished by Likeness [1977]. This approach treats diffraction of energy as it enters through an aperture in a statistical manner, and is designed for application in the Monte-Carlo ray-trace environment. It is based on Heisenberg's uncertainty principle and the particle theory of light. Neither of the two references that describe this approach includes many details of its implementation. The details necessary to successfully implement this approach, as developed by the current author are presented. Note that these details may differ from those used by the original developers of this method.

4.1.1 Appropriate application of the statistical approach

Rays are directed into the aperture as appropriate in the Monte-Carlo environment, and the distances δ_1 and δ_2 from the point of entry to the aperture edges are calculated for each entering ray, as illustrated in Figure 4.1. Experience tells us that entering rays will be diffracted; however, the extent to which this diffraction occurs depends upon the wavelength of the entering radiation relative to the dimensions of the aperture through which it enters. When modeling the diffraction of rays as they pass through an aperture which is much larger than the wavelength of the entering radiation, only rays in a limited region, or no rays at all, should be diffracted. In some such cases it will be acceptable to neglect diffraction altogether and use an ideal ray approximation. Wyatt [1987] suggests that this approximation is only acceptable when $\Delta\xi > 10.0$ (where $\Delta\xi$ is given by equation 3.1). However, diffraction patterns shown in Figure 3.4 indicate that this rule may be too restrictive. Regardless, when modeling a case in which the entering wavelength is much shorter than the dimensions of the aperture through which it enters, but where the ideal ray approximation would not be appropriate, Likeness [1977] suggests that the statistical diffraction model be applied to within 50λ to 500λ from the edge, while Morbey and Hutchings [1993] suggest application to within 100λ.

If the dimensions of the aperture are on the order of the wavelength of the entering energy, all entering rays must be diffracted. The statistical approach treats diffraction as an edge effect, and the question arises as to which edge (or if both edges) of the aperture should affect the entering energy bundle. A method of dealing with such cases appropriately is needed. Four methods were investigated and are presented in this chapter. However from this point forward, the parameter δ is used as a general parameter that takes on both values, δ_1 and δ_2, depending on the ray that is being traced and the method being used.

4.1.2 Description of the statistical approach

This approach is based in part on the Heisenburg uncertainty principle, which states that when making simultaneous measurements of a particle's momentum, p, and position, x, the product of the uncertainties in these two measurements cannot be less than $\frac{\hbar}{2}$, where $\hbar = \frac{h}{2\pi}$, and h is Planck's constant (6.63×10^{-34} J•s).

That is,

$$\Delta p \times \Delta x \geq \frac{\hbar}{2}, \tag{4.1}$$

where Δ indicates the amount of uncertainty in a particular measurement. Since a particle's position is described in three dimensions, we can write the uncertainty principle in three ways:

$$\Delta p_x \times \Delta x \geq \frac{\hbar}{2}, \tag{4.2}$$

$$\Delta p_y \times \Delta y \geq \frac{\hbar}{2}, \tag{4.3}$$

and

$$\Delta p_z \times \Delta z \geq \frac{\hbar}{2}. \tag{4.4}$$

We model Heisenburg's uncertainty principle as an equality,

$$\Delta p_y \times \Delta y = \frac{\hbar}{2} = \frac{h}{4\pi}, \tag{4.5}$$

and take the uncertainty in position (in the y direction) of an entering energy bundle to be δ, the distance from the point of entry to the aperture edge. Thus

$$\Delta p_y = \frac{h}{4\delta\pi}. \qquad (4.6)$$

Referring to the construction of Figure 4.2, the uncertainty in momentum in the y direction is interpreted in terms of an angle of diffraction. We define ϕ^* as the maximum angle of diffraction where the angle of diffraction, ϕ_d, is less than or equal to $\pm\,\phi^*$. Thus ϕ^* defines the range of values that ϕ_d can take on.

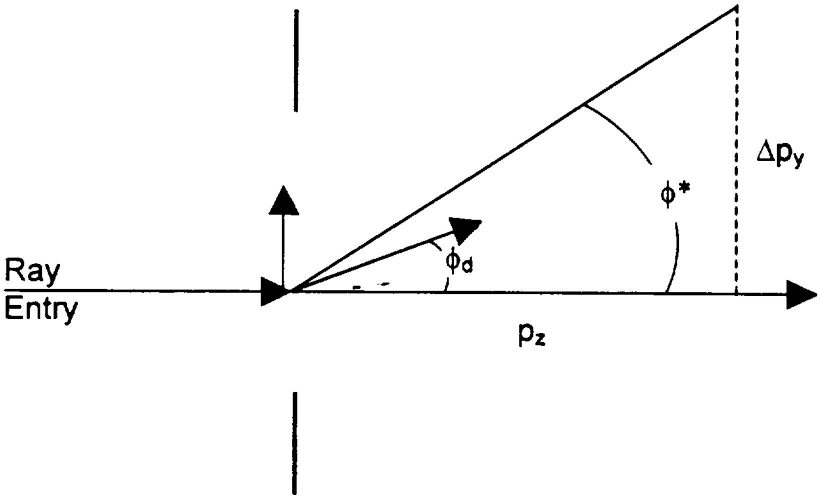

Figure 4.2 Illustration of possible spread of diffraction angles in the application of the statistical approach to modeling diffraction.

Using this construction we can write

$$\tan(\phi^*) = \frac{\Delta p_y}{p_z}. \qquad (4.7)$$

Using the equalities $p_z = \frac{h}{\lambda}$, the wave number, $k = \frac{2\pi}{\lambda}$, and equation 4.6, and substituting into equation 4.7 yields

$$\tan(\phi^*) = \frac{\Delta p_y}{p_z} = \frac{1}{2k\delta}, \qquad (4.8)$$

or

$$\phi^* = \tan^{-1}\left(\frac{1}{2k\delta}\right). \qquad (4.9)$$

Likeness proposed the use of a normal distribution as the probability density function of the diffracted energy, where the most probable path of an entering energy bundle is straight ahead (mean, $\mu=0$), and the standard deviation is taken to be $\phi^* = \tan^{-1}\left(\frac{1}{2k\delta}\right)$. Thus

$$p(\phi_d) = \frac{1}{\sqrt{2\pi}\ \phi^*}\exp\left[-\frac{1}{2}\left(\frac{\phi_d}{\phi^*}\right)^2\right]; \qquad (-\infty \le \phi_d \le \infty) \qquad (4.10)$$

is the probability that a ray will be diffracted at an angle ϕ_d from its original line of travel due to the influence of a single aperture edge. In order to make use of this probability density function in a Monte-Carlo ray-trace environment, we integrate the probability density function with respect to ϕ_d from $-\infty$ to ϕ_d to obtain the cumulative distribution function (c.d.f). A c.d.f., $P_x(x)$, has the useful property that "if x is a random number, and we have the c.d.f, $P_x(x)$, and if $P_x(x)$ is continuous, the random variable Y produced by the transformation $Y=P_x(x)$ has a uniform distribution over the interval (0,1)" [Gibbons and Chakraborti, 1992]. For a more detailed discussion of this c.d.f. property, see Walkup [1996]. We must interpret this integral in terms of the physical limits, where the range of angles that ϕ_d can subtend after entering the aperture is limited to $\left(-\frac{\pi}{2} \le \phi_d \le \frac{\pi}{2}\right)$, as illustrated in Figure 4.3.

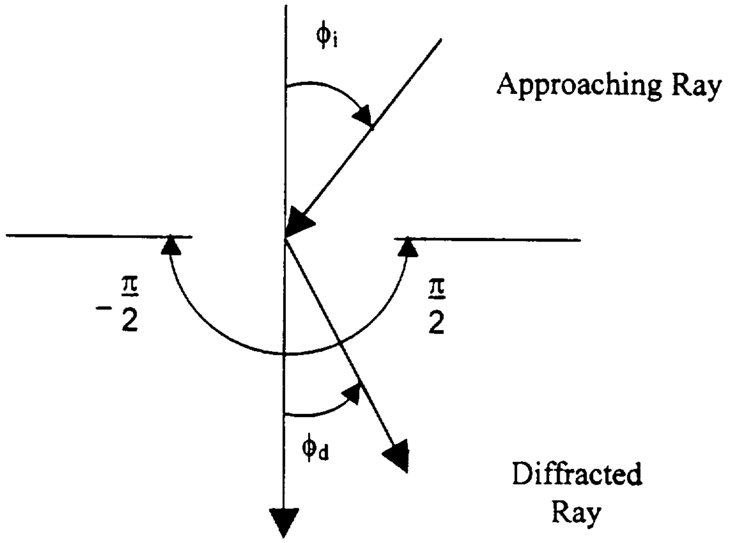

Figure 4.3 Illustration of approaching and diffracted ray angles.

We must therefore do a substitution such that when $|\phi_d| \geq \frac{\pi}{2}$, $p(\phi_d) = 0$. Such is the case when evaluating $p(\tan(\phi_d))$ as illustrated in Figure 4.4.

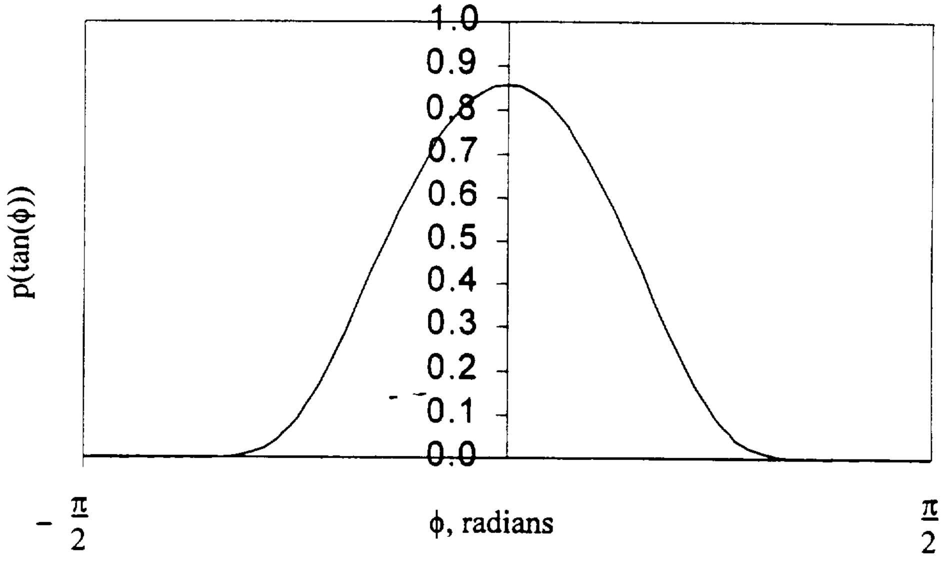

Figure 4.4 Probability density function of $\tan(\phi_d)$

The c.d.f., which ranges uniformly between (0-1), becomes

$$P[\tan(\phi_d)] = \int_{\phi'_d=-\infty}^{\phi_d} p(\tan\phi'_d)\ d(\tan\phi'_d) = \text{Random number uniformly distributed} \qquad (4.11)$$

between 0 and 1, where

$$p[\tan(\phi'_d)] = \frac{1}{\sqrt{2\pi}\ \phi^*}\exp\left[-\frac{1}{2}\left(\frac{\tan(\phi'_d)}{\phi^*}\right)^2\right]. \qquad (4.12)$$

Thus

$$P[\tan(\phi_d)] = \frac{1}{\sqrt{2\pi}\ \phi^*}\int_{-\infty}^{\phi_d}\exp\left[-\frac{1}{2}\left(\frac{\tan(\phi'_d)}{\phi^*}\right)^2\right] d(\tan(\phi'_d)). \qquad (4.13)$$

Making the substitution

$$a^2 = \frac{1}{2\,(\phi^*)^2}, \quad a = \frac{1}{\sqrt{2}\;\phi^*},$$

there results

$$P[\tan(\phi_d)] = \frac{1}{\sqrt{2\pi}\;\phi^*} \int_{-\infty}^{\phi_d} \exp\left[-a^2 \tan^2(\phi'_d)\right] d[\tan(\phi'_d)]. \tag{4.14}$$

A second substitution, $u = a\tan(\phi'_d)$, thus $du = a d[\tan(\phi'_d)]$ yields

$$P[\tan(\phi_d)] = \frac{1}{\sqrt{2\pi}\;\phi^*} \int_{-\infty}^{a(\tan\phi_d)} \exp\left(-u^2\right) \frac{du}{a} = R_\phi, \tag{4.15}$$

where R_ϕ is a random number uniformly distributed between 0 and 1. Rearranging and multiplying both sides of equation 4.15 by 2, there results

$$2\sqrt{2}\;\phi^* a R_\phi = \frac{2}{\sqrt{\pi}} \int_{-\infty}^{a(\tan\phi_d)} \exp(-u^2)\; du. \tag{4.16}$$

Substituting $a = \frac{1}{\sqrt{2}\;\phi^*}$ on the left-hand side yields

$$2R_\phi = \frac{2}{\sqrt{\pi}} \int_{-\infty}^{a(\tan\phi_d)} \exp(-u^2)\; du. \tag{4.17}$$

Equation 4.17 can be rewritten

$$2R_\phi = \frac{2}{\sqrt{\pi}} \int_{-\infty}^{0} \exp(-u^2)\; du \; + \; \frac{2}{\sqrt{\pi}} \int_{0}^{a(\tan\phi_d)} \exp(-u^2)\; du \tag{4.18}$$

or

$$2R_\phi = -\frac{2}{\sqrt{\pi}} \int_{0}^{-\infty} \exp(-u^2)\; du \; + \; \frac{2}{\sqrt{\pi}} \int_{0}^{a(\tan\phi_d)} \exp(-u^2)\; du. \tag{4.19}$$

Then invoking the definition and properties of the error function,

$$\mathrm{erf}(x) \equiv \frac{2}{\sqrt{\pi}} \int_{0}^{x} \exp(-\eta^2)\; d\eta, \quad \mathrm{erf}(-x) = -\mathrm{erf}(x), \quad \mathrm{erf}(\infty) = 1, \quad \mathrm{erf}(0) = 0,$$

we find that

$$2R_\phi = -\mathrm{erf}(-\infty) + \mathrm{erf}[a\tan(\phi_d)] = 1 + \mathrm{erf}[a\tan(\phi_d)]. \tag{4.20}$$

Finally, substituting $a = \dfrac{1}{\sqrt{2}\ \phi^*}$ yields

$$2R_\phi - 1 = \operatorname{erf}\left(\frac{\tan(\phi_d)}{\sqrt{2}\ \phi^*}\right). \tag{4.21}$$

Equation 4.21 is used to determine the angle at which the entering ray is diffracted. An additional programming step may be required in order to arrive at a value for ϕ_d. If using a programming language without a built-in error function (such as FORTRAN), an infinite series approximating the error function and the root-finding bisection method can be used to find the value of x when erf(x) is known. This infinite series, given by

$$\operatorname{erf}(x) = \frac{2}{\sqrt{\pi}}\left(x - \frac{x^3}{3\cdot 1!} + \frac{x^5}{5\cdot 2!} - \frac{x^7}{7\cdot 3!} + \ldots\right), \tag{4.22}$$

when expanded to eleven terms approximates the error function quite well when erf(x) ≤ 0.992869. Additional terms do not provide much improvement, as shown in Figure 4.5. If erf(x) is between 0.992869 and 1, this infinite series deviates from erf(x), and x can be approximated as 2 (or any other number greater than 2). The subroutine used is provided in Appendix A. Note that the results obtained using this subroutine were compared to results found using FORTRAN Powerstation, which includes a built-in error function. The resulting diffraction patterns were identical, thus it can be concluded that either the necessary approximations had no effect on the results, or that FORTRAN Powerstation makes the same approximations.

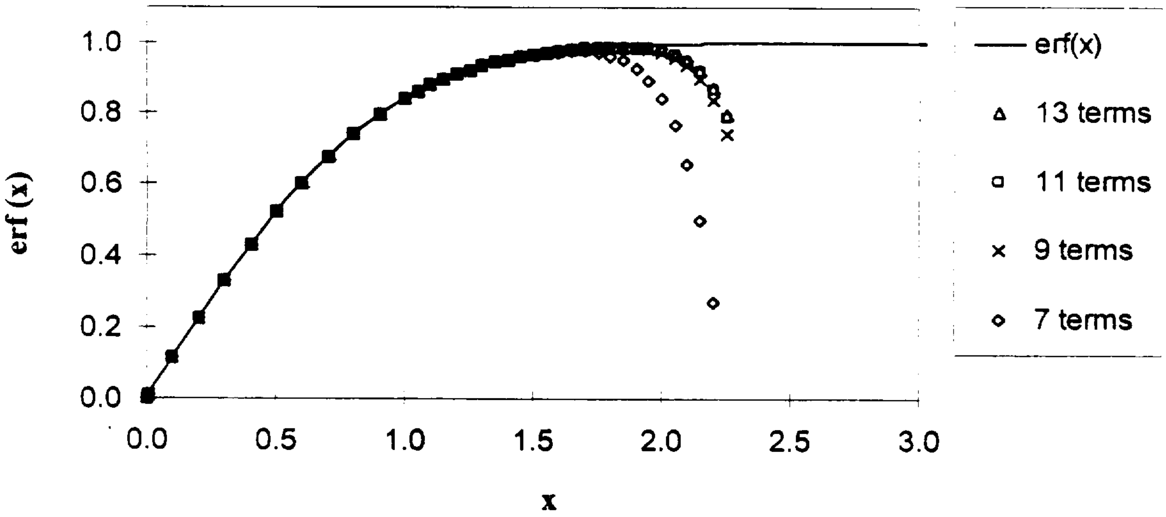

Figure 4.5 Approximating the error function with an infinite series with an increasing number of terms.

4.1.3 Determining the diffraction pattern

As previously noted, for cases in which the wavelength of the entering radiation is of the same order as the dimensions of the aperture through which rays enter, each entering ray must be diffracted in some way. The angle of diffraction depends on the method chosen and the point of ray entry. After being diffracted in some way, the energy bundle continues until it is intercepted by the observation screen, and this point of interception is determined. In order to keep track of the spatial distribution of rays as they arrive at the observation screen illustrated in Figure 4.1, the screen is divided into a large number of strips in the y direction, serving as discrete "bins". Each time that a diffracted ray arrives at one of these bins, a counter is incremented for that particular bin. This provides the distribution of diffracted energy along the y direction. The number of rays arriving in each bin is normalized with respect to the bin with the most arriving rays. This normalized curve is then scaled such that the area beneath the resulting curve is approximately the same as that beneath the curve of the analytical solution (here this has been done "by eye"). This was similar to the approach used by Heinsch and Chou [1971], as they report using a scaling factor, f, which is determined by trial and error to give the best possible match with the analytical solution. The statistical approach does not keep track of phase, thus the results obtained do not model the side fringes of the analytical interference pattern, rather they form a single smooth curve that averages these fringes. Keeping track of phase would not result in a diffraction pattern with the details of the side fringes, for reasons that will become clear after the presentation of the second model. These results are adequate for most modeling efforts as it will usually suffice to know the approximate distribution of diffracted energy, which can be modeled quite well. This approach is applicable to both Fraunhofer and Fresnel diffraction.

4.1.4 Modeling diffraction in a practical example

4.1.4.1 GERB linear-array cavity detector

A project that has recently been the topic of much research in the Thermal Radiation Group involves a thermal radiation detector originally designed for GERB (Geostationary Earth Radiation Budget) [Mahan and Langley, 1996; Weckmann, 1997; Mahan *et al.*, 1998; Sánchez, 1998; Sorensen, 1998]. This detector consists of a linear-array detector housed within the wedge-shaped, mirrored cavity shown in Figure 4.6. Radiant energy from an Earth scene enters the cavity through a 60 μm wide slit. The detector is used to measure the arriving radiation in the wavelength interval between from 0.32 and 40 μm. This represents a case in which neglecting diffraction effects in the radiative model may lead to highly erroneous results.

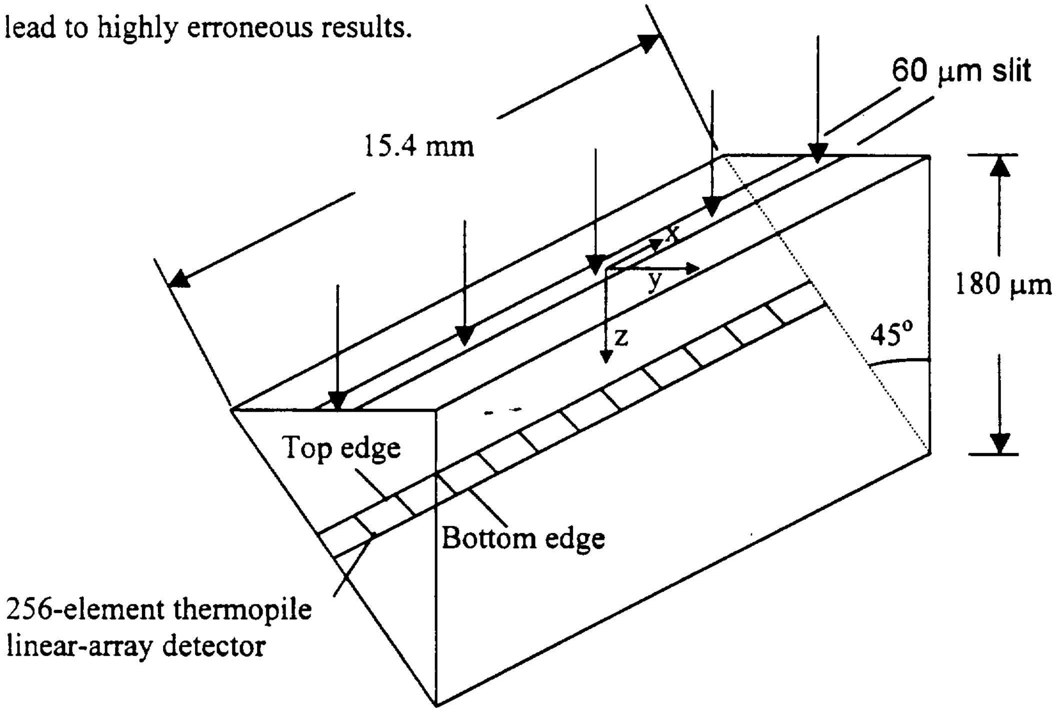

Figure 4.6 Cavity detector developed by members of the Thermal Radiation Group.

The first step in assessing diffraction effects in the cavity detector involves determining the regime into which the occurring diffraction falls. We imagine an xy plane passing through the thermopile detector along its top edge, and use $\Delta\xi$ to determine the diffraction regime at this plane. We see that when the entering wavelength (λ) is 0.4 μm, $\Delta\xi = 17.3$. Likewise, when λ=4.0 μm, $\Delta\xi = 5.5$ and when λ=40 μm, $\Delta\xi = 1.7$. Since $\Delta\xi > 1.0$ over the total range of wavelengths to be measured, diffraction within the cavity will always occur in the Fresnel region. Note that if we were to study diffraction on an xy plane passing through the bottom edge of the detector, Fresnel diffraction would still prevail over the measured wavelengths. Figure 4.7 illustrates the changing diffraction pattern which will occur on the linear-array detector as radiant energy of three wavelengths enters the GERB cavity detector.

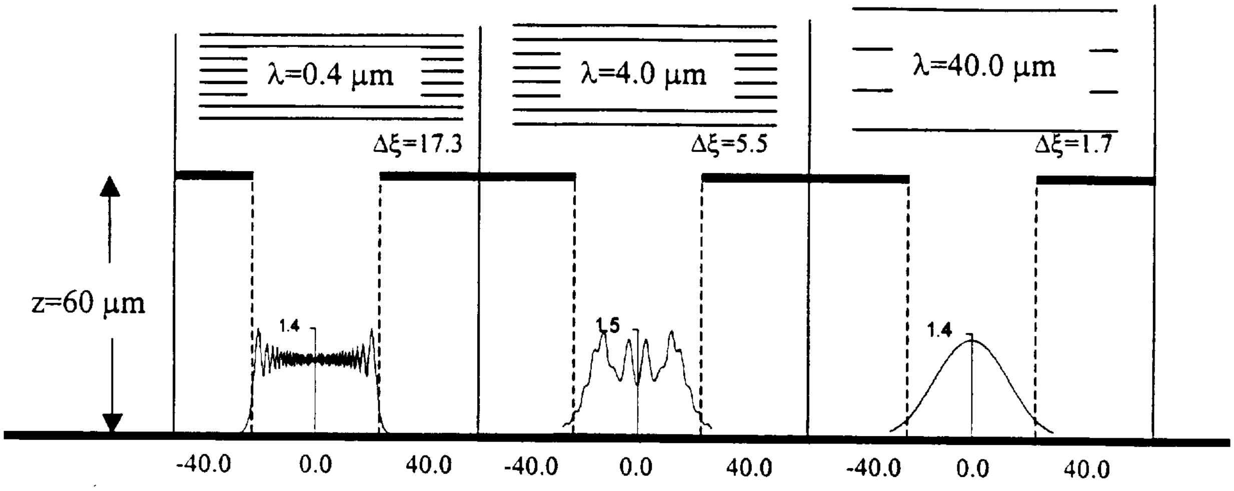

All slit widths = 60 μm

Figure 4.7 Diffraction patterns expected at the top edge of the linear-array detector over the range of wavelengths of interest.

4.1.4.2 Application of the statistical approach

The statistical approach was applied to model the diffraction of energy as it enters the GERB detector geometry. A radiative model of the GERB cavity detector which ignores diffraction effects already exists, so the effort reported here serves as a final step in the development of a complete radiative model.

The diffraction patterns obtained from the application of the statistical approach are compared to the closed-form analytical diffraction patterns in order to validate the use of the statistical method. This is also a study of an intermediate step within the statistical method. Recall that as an energy bundle enters a slit aperture, the distances from the point of entry to each edge, δ_1 and δ_2, are calculated. It was previously stated that we take the unknown in the entering energy bundle's position as δ. We must establish which δ is to be used; that is, we must decide which edge is assumed to diffract the entering energy bundle when the slit is on the order of the wavelength of the entering energy. In cases such as the aperture of the cavity detector in Figure 4.6, which is essentially an infinite slit, it is expected that both edges should affect the momentum of the entering energy bundle in the same direction (in the present case, the y direction). Neither of the two references cited address this situation, so four possible approaches were tested.

4.1.4.3 Four methods of application of the statistical model

We have developed four methods for using the statistical model to describe diffraction. The first method involves summing the angles of diffraction due to both edges of the slit as they influence a single ray. As a ray enters, the angle of diffraction due to each edge is determined using equation 4.21, one independent of the other, and the two diffraction angles are algebraically summed to give the final diffraction angle of the entering ray.

The second method involves splitting the rays as they enter through the aperture. As a single ray enters, this single ray becomes two rays. One ray is diffracted by the first edge, located δ_1 from the point of entry. The other ray is diffracted by the opposite edge, δ_2 from the point of entry.

The third method involves allowing the side that is closest to the point of entry to diffract the entering ray, ignoring the other side.

The final method involves defining the angle of diffraction of an entering ray as the angle at which the ray is diffracted due to the influence of the edge that is furthest from the point of entry, ignoring the closest edge.

All four of these approaches were implemented for five different cases involving the GERB cavity detector of Figure 4.6. The angle of approach ϕ_i (illustrated in Figure 4.3) was zero for all cases studied. These cases involved radiation entering at wavelengths of 0.4, 4.0, 40.0, 100.0, and 160.0 μm; corresponding to values of $\Delta\xi$ of 17.3, 5.5, 1.7, 1.1, and 0.86, respectively. Note that the cavity detector is not intended to measure wavelengths beyond 40.0 μm. Diffraction was studied at 100 and 160 μm in order to test the statistical method in both the Fresnel and Fraunhofer regions, as well as in the transition region. The FORTRAN code used to conduct this study is provided in Appendix A.

4.1.4.4 Results

Figures 4.8 through 4.12 provide the results of the study described in Section 4.1.4.3. Figure 4.8 involves modeling diffraction in the extremely near-field. This case approximates the diffraction situation that occurs in the GERB cavity-detector when used to measure radiation at the shortest measured wavelength of 0.32 μm. In this case, any of the four methods yields reasonable results. However, results from the summing angles, splitting rays, and closest side approaches approximate the analytical solution particularly well and are practically identical. According to the previously described criterion by Wyatt [1987], this is the only configuration for which the ideal ray approximation would be appropriate. Figure 4.9 also involves diffraction in the very near-field. In this case both the summing angles and the closest side approach yield the best results. Figure 4.10 presents the results from modeling diffraction in the barely near-field, and again the summing angles and closest side approaches work the best. This case models the diffraction situation that occurs in the GERB cavity-detector when used to measure radiation at the longest measured wavelength of 40 μm. Figure 4.11 involves modeling diffraction in the transition region. In this case the results obtained from the summing angles approach are superior to those obtained from application of all of the other three cases. Finally, Figure 4.12 involves diffraction in the far-field. In this case, either the summing angles or the closest side approach works reasonably well.

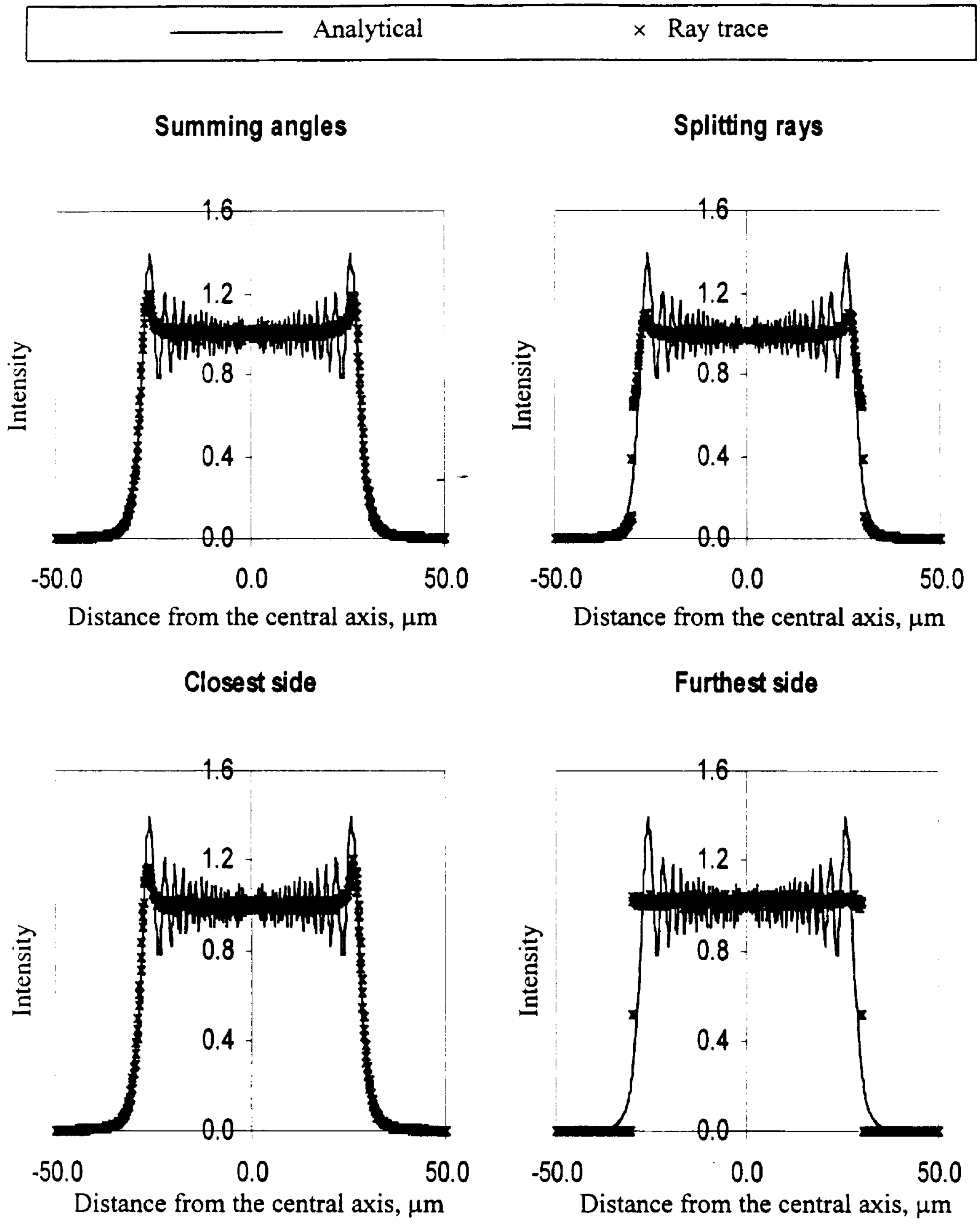

Figure 4.8 Comparison between the results using all four methods of implementing the statistical approach to diffraction, and the closed-form analytical description of the diffraction of radiation entering the cavity detector when the entering wavelength is 0.4 μm, the slit width is 60 μm, and the distance to the screen is 60 μm.

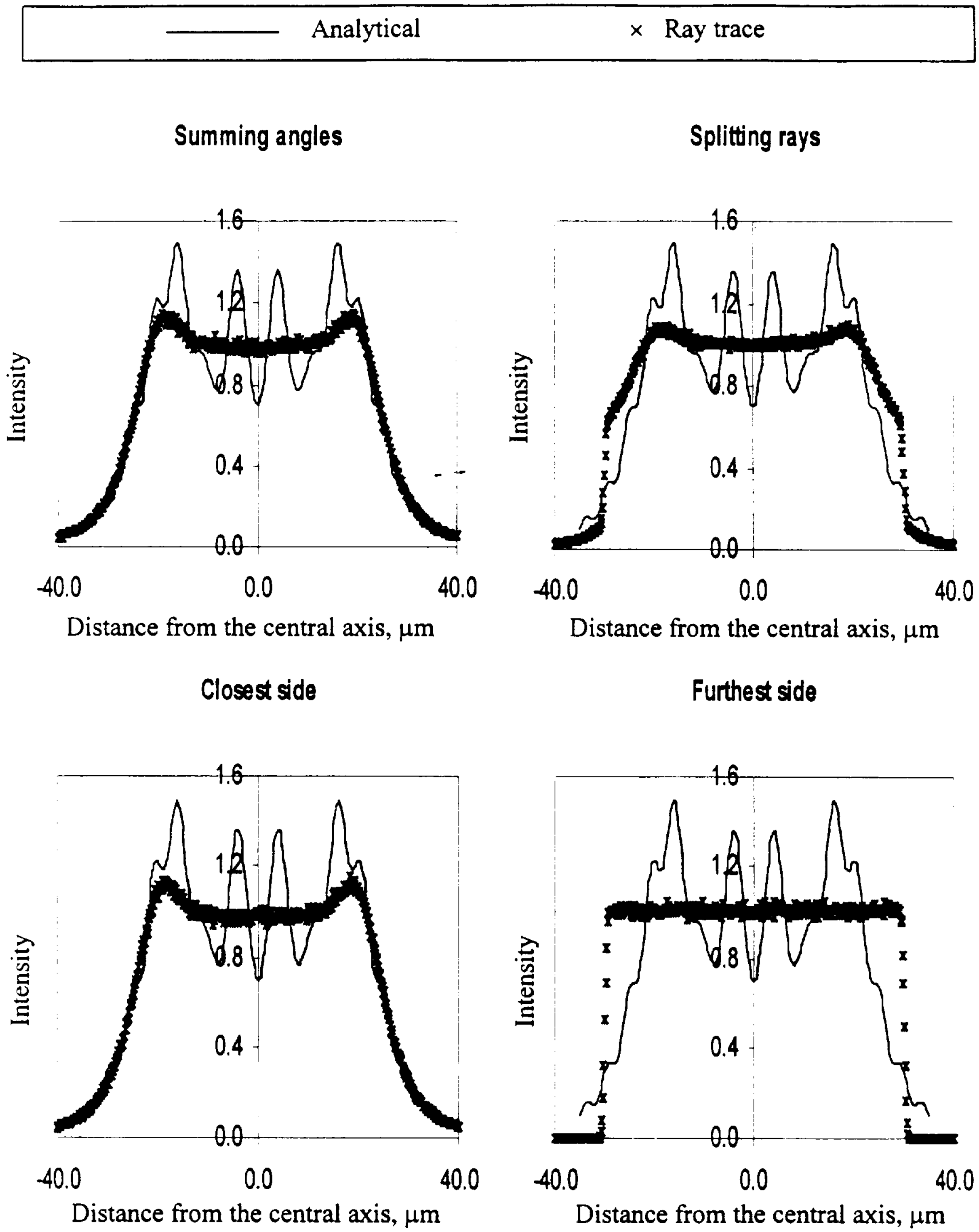

Figure 4.9 Comparison between the results using all four methods of implementing the statistical approach to diffraction, and the closed-form analytical description of the diffraction of radiation entering the cavity detector when the entering wavelength is 4.0 µm, the slit width is 60 µm, and the distance to the screen is 60 µm.

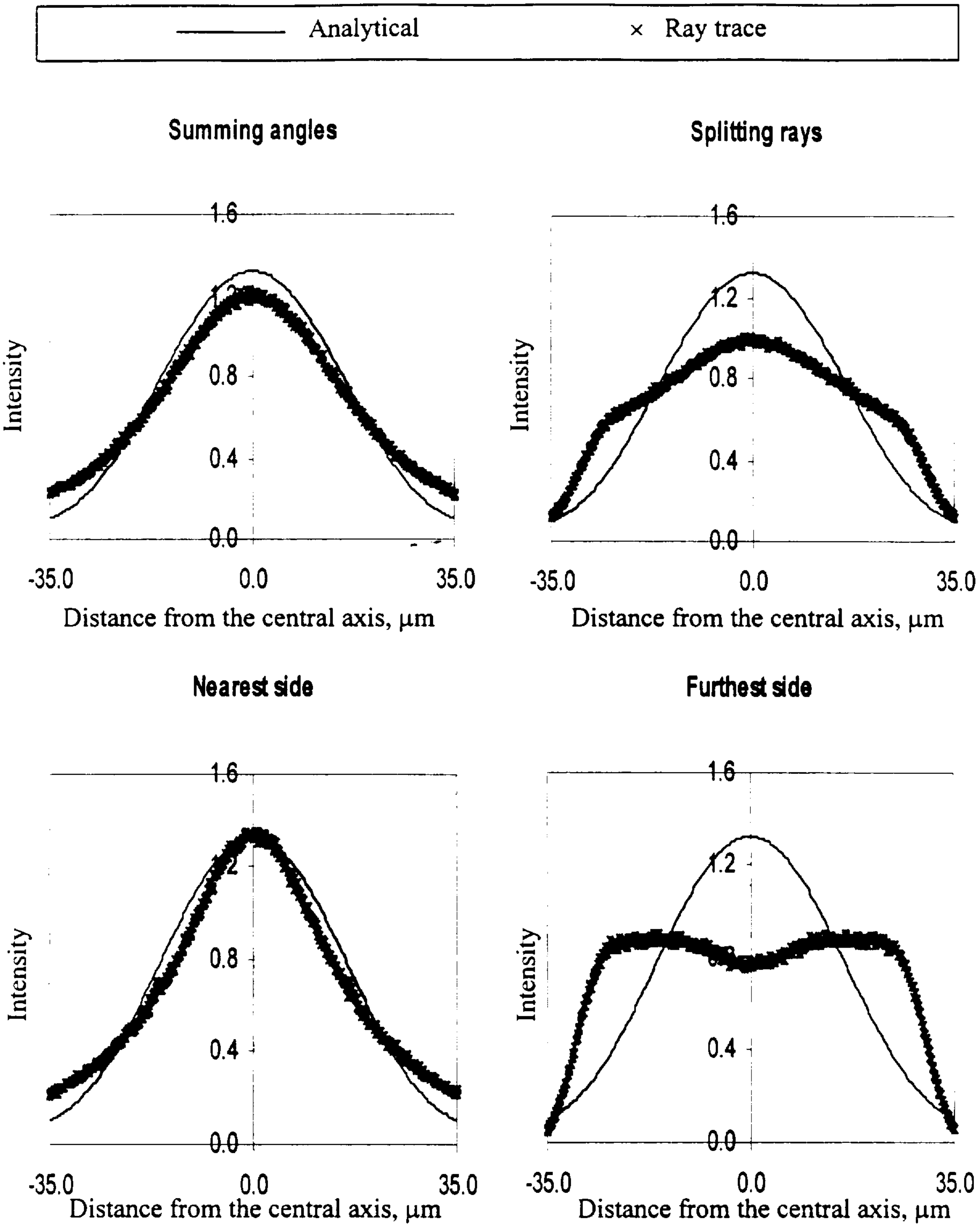

Figure 4.10 Comparison between the results using all four methods of implementing the statistical approach to diffraction, and the closed-form analytical description of the diffraction of radiation entering the cavity detector when the entering wavelength is 40 µm, the slit width is 60 µm, and the distance to the screen is 60 µm.

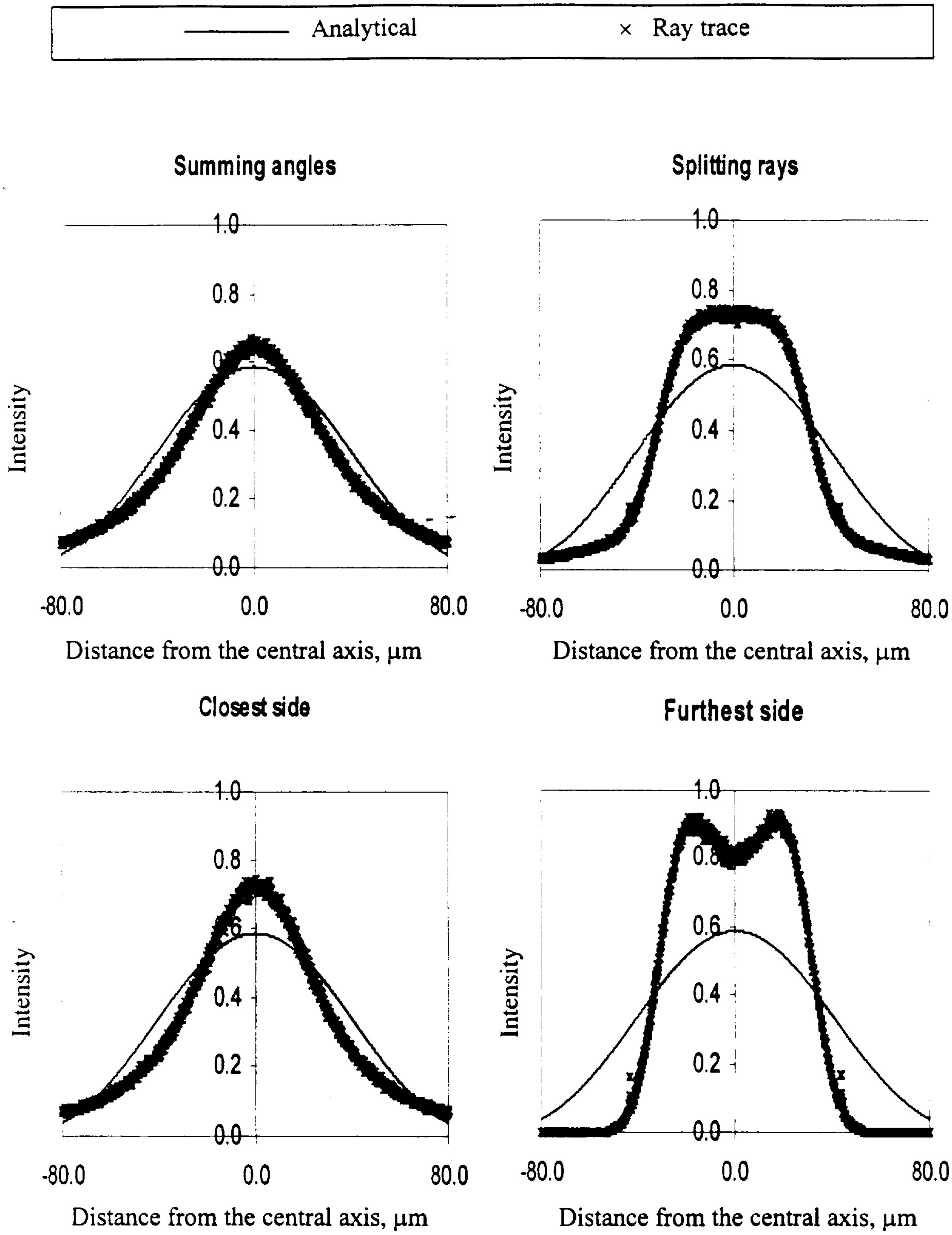

Figure 4.11 Comparison between the results using all four methods of implementing the statistical approach to diffraction, and the closed-form analytical description of the diffraction of radiation entering the cavity detector when the entering wavelength is 100.0 μm, the slit width is 60 μm, and the distance to the screen is 60 μm.

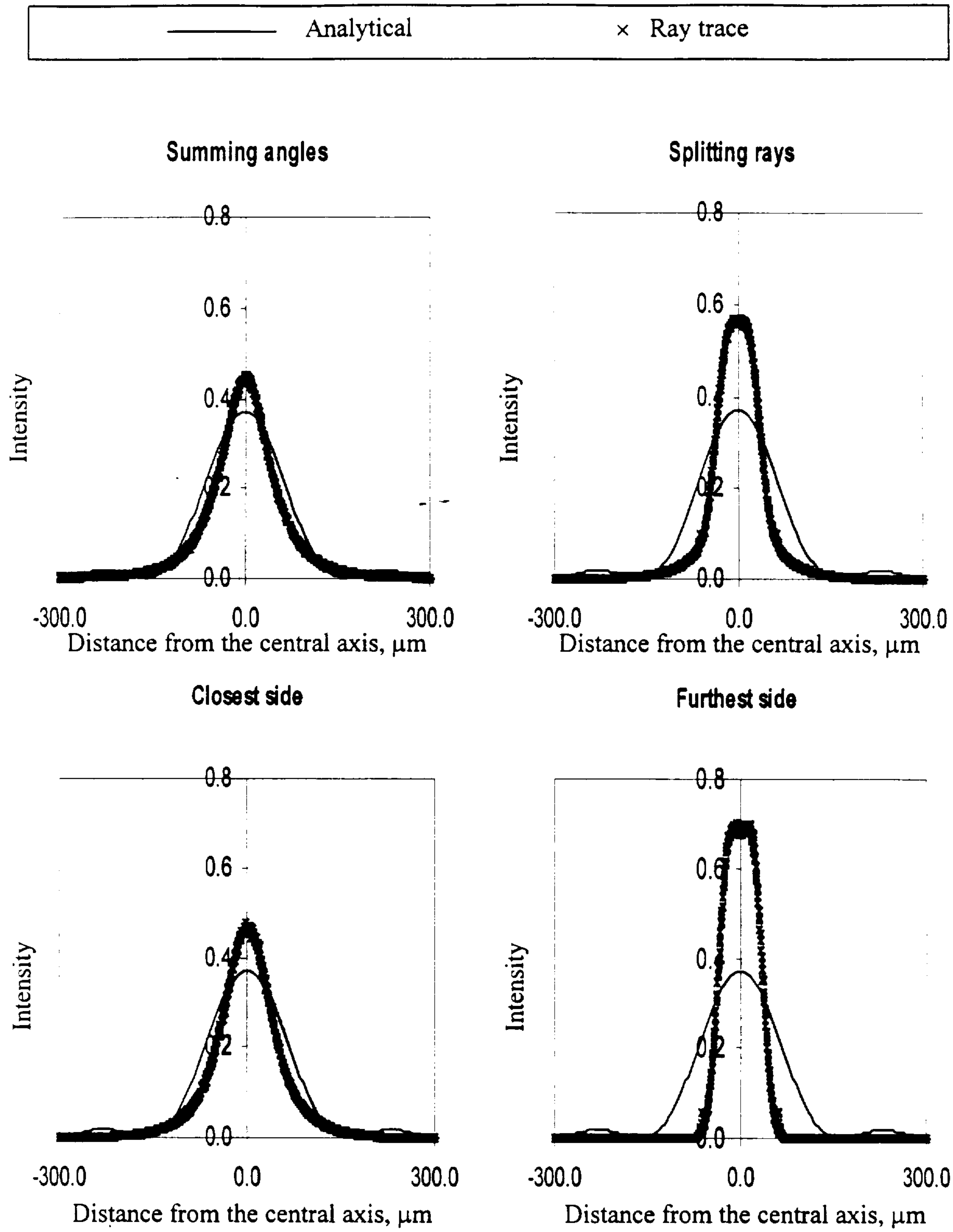
Summing angles

Splitting rays

Closest side

Furthest side

Figure 4.12 Comparison between the results using all four methods of implementing the statistical approach to diffraction, and the closed-form analytical description of the diffraction of radiation entering the cavity detector when the entering wavelength is 160.0 μm, the slit width is 60 μm, and the distance to the screen is 60 μm.

4.1.5 Conclusions: Method of choice in application of statistical model

Results in Figures 4.8 through 4.12 show that the summing angles approach consistently yields good results, while the other three methods only yield acceptable results for certain cases. The results obtained while using the summing angles approach serve as validation of the statistical approach to the numerical modeling of diffraction.

4.2 Background for understanding diffraction Model 2

This presentation serves to provide an understanding of the nature of diffraction, and as background for understanding the second diffraction model. It borrows heavily from the presentation of Fraunhofer diffraction by an infinite slit by Serway [1994].

The first step in the determination of a diffraction pattern resulting from an infinite slit involves dividing the slit into a large number (n) of zones of width (Δy) where $\Delta y = a/n$, as illustrated in Figure 4.13.

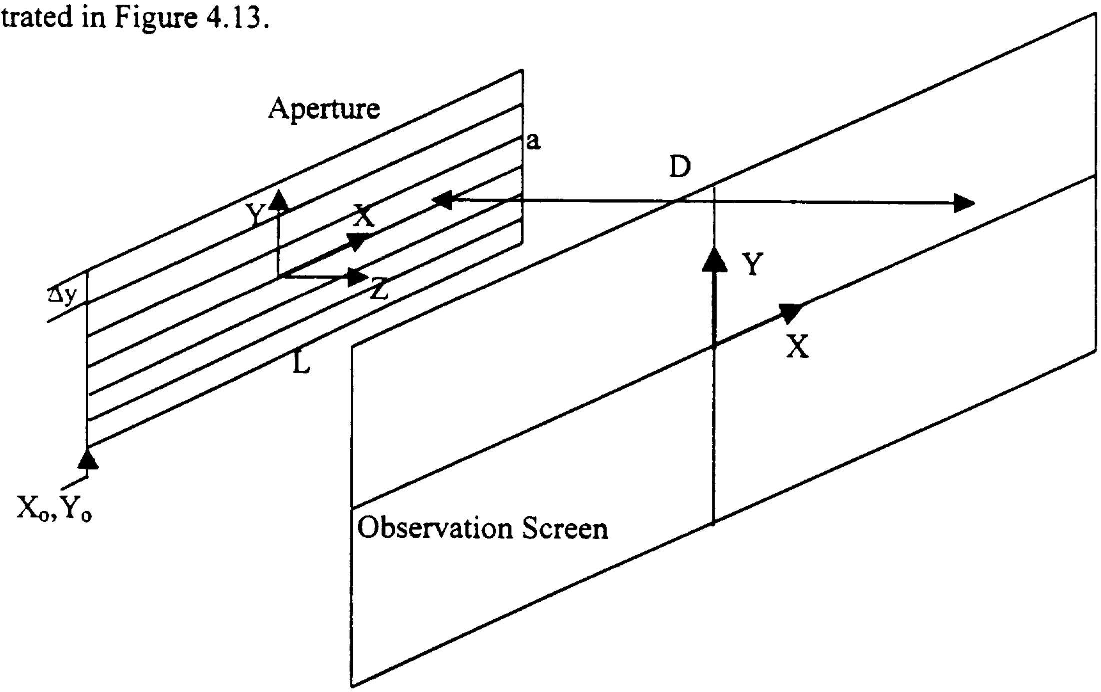

Figure 4.13 Illustration of division of aperture into zones.

Each zone is to serve as a source of coherent radiation such that each contributes an incremental electric field amplitude, ΔE, at any point on the observation screen. If this approach were modeled in a ray-trace environment, instead of treating the most probable path for an entering energy bundle as straight ahead with a spread of paths following a normal distribution as in the statistical method, this method would treat each as having an equal probability of going in any direction. If a sufficient number of energy bundles were directed into the aperture at a given zone, the result would be an even distribution over the entire observation screen due to that zone.

Diffraction occurs because adjacent areas on an aperture all behave as independent sources. The energy leaving a given point on the aperture and arriving at a given point P on an observation screen will differ in phase from energy arriving to the same point P from another point on the aperture. The difference in path length, δ, of rays coming from adjacent zones and arriving at the same point on an observation screen can be determined. This difference in path length is indicative of the difference in phase, since the phase of a ray is proportional to the distance it travels. Suppose that an infinite slit of width a is divided into two halves, as pictured in Figure 4.14.

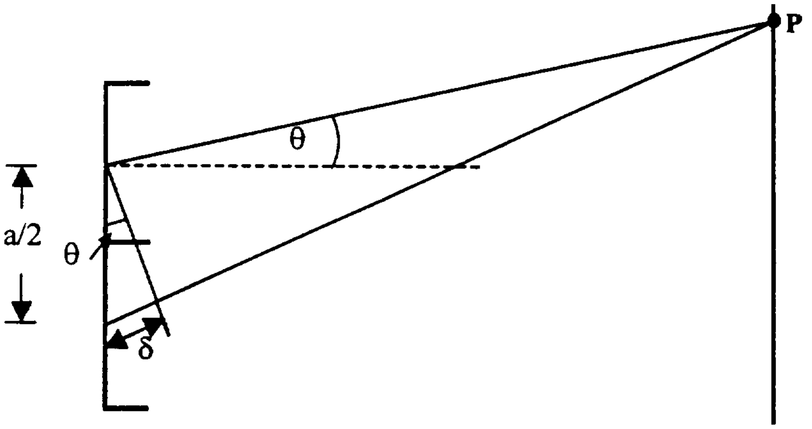

Figure 4.14 Illustration of the determination of the difference in path length traveled by rays entering from different halves of an aperture.

The difference in path length between waves entering the two halves is given by

$$\delta = \frac{a}{2}\sin\theta . \tag{4.23}$$

In general, if a slit aperture is divided into n parts, the difference in path length between adjacent areas is given by

$$\delta = \frac{a}{n}\sin\theta . \tag{4.24}$$

Since the width (Δy) of the strips into which the aperture is divided is given by a/n,

$$\delta = \Delta y \sin\theta . \tag{4.25}$$

The incremental electric field amplitudes between adjacent zones are out of phase with one another by the amount ΔB, given by

$$\Delta B = \frac{2\pi\delta}{\lambda}, \tag{4.26}$$

where λ is the wavelength of the entering radiation, and δ is the difference in path length traveled by energy bundles leaving adjacent areas and arriving at the same point on the screen. Using phasor diagrams to determine the intensity at a given point, the total electric field is obtained by summing the contributions from all zones at a given point on the observation screen. The chord length, $E_{\theta P}$, is taken to be the amplitude of the electric field at P. Figure 4.15 (b) illustrates the addition of phasors for an infinite slit divided into four areas, shown in 4.15 (a). When the number of divisions on the aperture goes to infinity, the phasor diagrams become smooth curves, as illustrated in 4.15 (c).

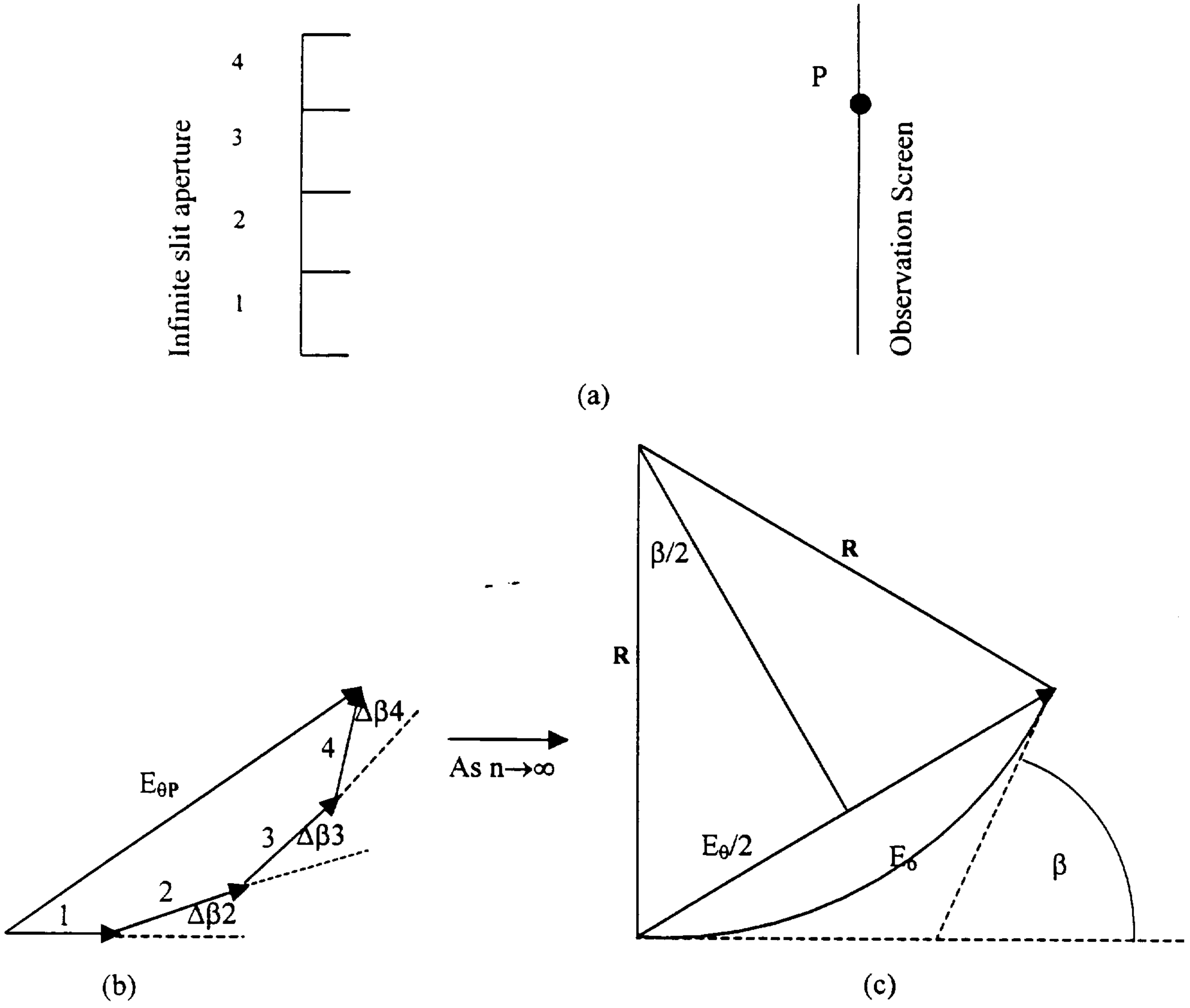

Figure 4.15 Determination of the amplitude of the electromagnetic field at a point on an observation screen placed in front of an infinite slit aperture. (a) Illustration of slit division, (b) phasor diagram construction, and (c) smooth curve that the phasor diagram becomes as the number of slit divisions goes to infinity.

Taking the arc length to be E_o, R to be the radius of curvature, and the total phase angle from the top to the bottom of the aperture to be β, simple geometric relations show that

$$\sin\frac{\beta}{2} = \frac{E_\theta/2}{R} \qquad (4.27)$$

Substituting the fact that the arc length, E_o, is given by Rβ yields

$$E_\theta = E_o\left[\frac{\sin(\beta/2)}{(\beta/2)}\right]. \tag{4.28}$$

Since intensity is proportional to the square of the electric field, we can then write

$$I_\theta = I_{max}\left[\frac{\sin(\beta/2)}{(\beta/2)}\right]^2, \tag{4.29}$$

where I_{max} is the intensity of the central maximum. Because we are discussing the entire slit, $\Delta y = a$, thus $\delta = a \sin\theta$. Substituting into equation 4.26, β in this case is given by

$$\beta = \frac{2\pi a \sin\theta}{\lambda}. \tag{4.30}$$

4.3 Model 2: Application of the modified Huygens-Fresnel principle

4.3.1 Basic description of Model 2

The second model proposed for use in the modeling of diffraction in the Monte-Carlo ray-trace environment is based on concepts presented in Section 4.2. It involves firing rays into an aperture, and modeling each point of ray entry as a source itself. The original plan for this approach was to model the point of entry of a ray as a source as defined by the Huygens-Fresnel principle, whereby the diffracted ray would have equal probability of going in any direction and each ray would carry with it an amplitude of unity. The distance traveled by the emitted ray before being intercepted by an observation screen was to be determined, and the phase assigned to this ray would be proportional to its length of travel. After many rays had been traced, the resulting intensity distribution was to be determined using a method that will be described shortly. The results obtained from the application of this approach did not agree with theory, as the secondary peaks were too high relative to the central maxima. A modified approach was then implemented in which the point of entry is modeled as a source which emits a ray in any forward direction. The amplitude of the optical field at any point on the observation screen is taken to be the superposition of all the rays arriving to that point (considering their amplitudes and relative phases). This approach is different from the initial approach in that all rays do not carry the same amplitude of unity. Instead, the magnitude of each ray is determined by an obliquity factor which is a function of the angle of ray diffraction.

4.3.2 The obliquity factor

The obliquity factor serves to properly model the variations in amplitude with angle over the surface of the secondary wavelets emanating from a source point, modeled incorrectly by the Huygens-Fresnel principle [Hecht and Zajac, 1974]. Kirchoff proposed that the obliquity factor, K, be given by

$$K(\phi_i, \phi_d) \cong \frac{1}{2}(\cos\phi_i + \cos\phi_d), \qquad (4.31)$$

where ϕ_i is the angle of incident radiation and ϕ_d is the angle of diffraction, as illustrated in Figure 4.3 [Mayes and Melton, 1994]. Later modified by Rayleigh and Sommerfeld, and then by Miller, the suggested obliquity factor became

$$K(\phi_d) = \cos(\phi_d). \qquad (4.32)$$

For the present purposes, use of either of these factors provides comparable results. Figure 4.16 shows the weighting to be placed on an diffracted ray as a function of diffraction angle when the incident energy approaches normal to the slit, as suggested by Huygens, Kirchoff, Rayleigh and Sommerfeld and Miller.

Figure 4.17 demonstrates how a source point of radiant entry would be modeled if we were to apply the Huygens-Fresnel principle alone. When weighted by the Rayleigh/Sommerfeld obliquity factor, the entry point is modeled as illustrated in Figure 4.18.

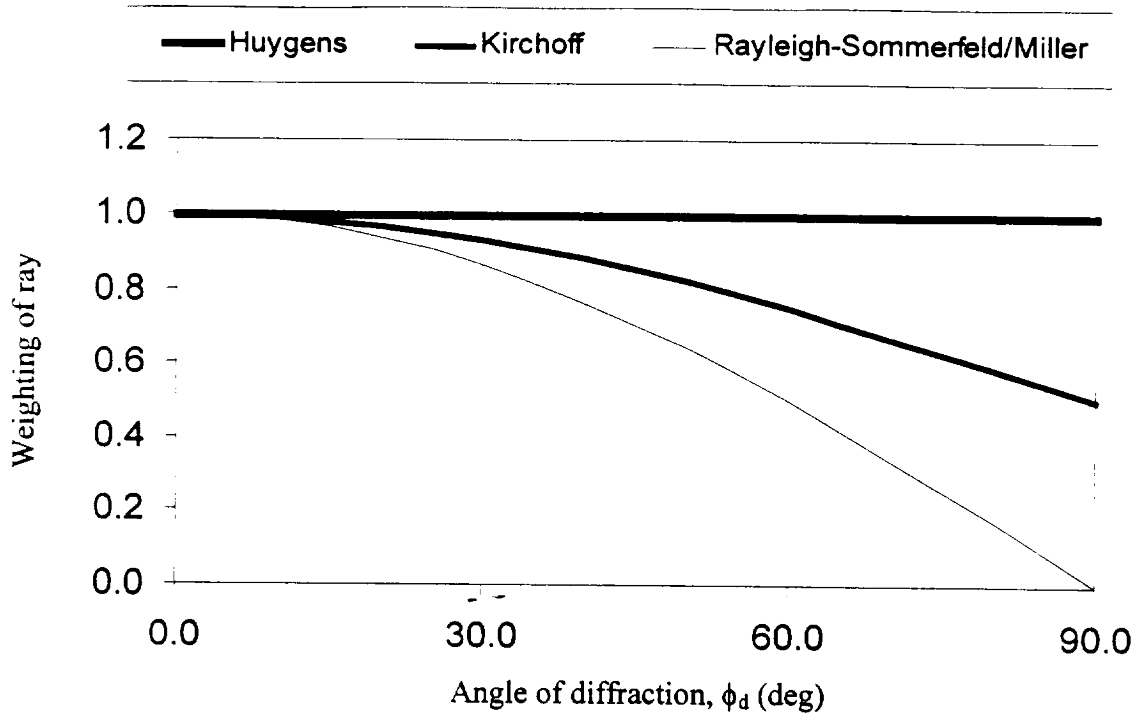

Figure 4.16 Weighting to be placed on rays when using two different obliquity factors, or none at all.

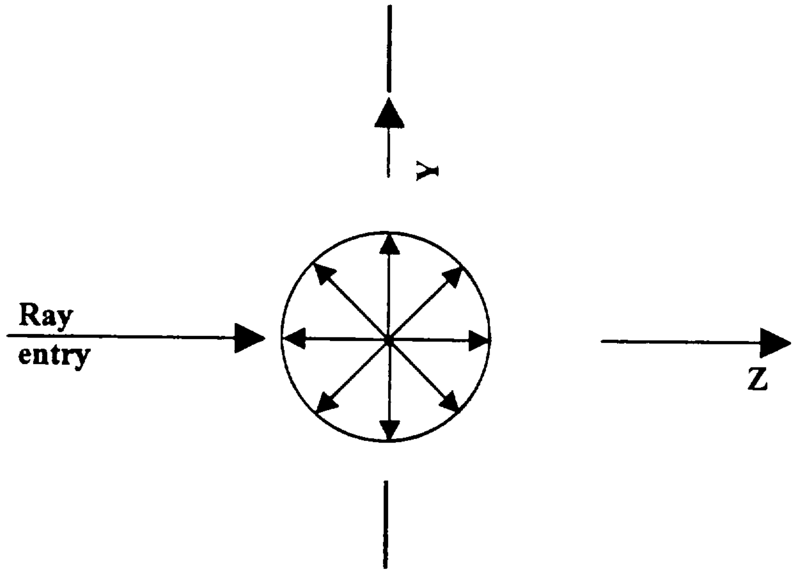

Figure 4.17 Model of a point source of rays entering a slit when employing the Huygens-Fresnel principle with no obliquity factor.

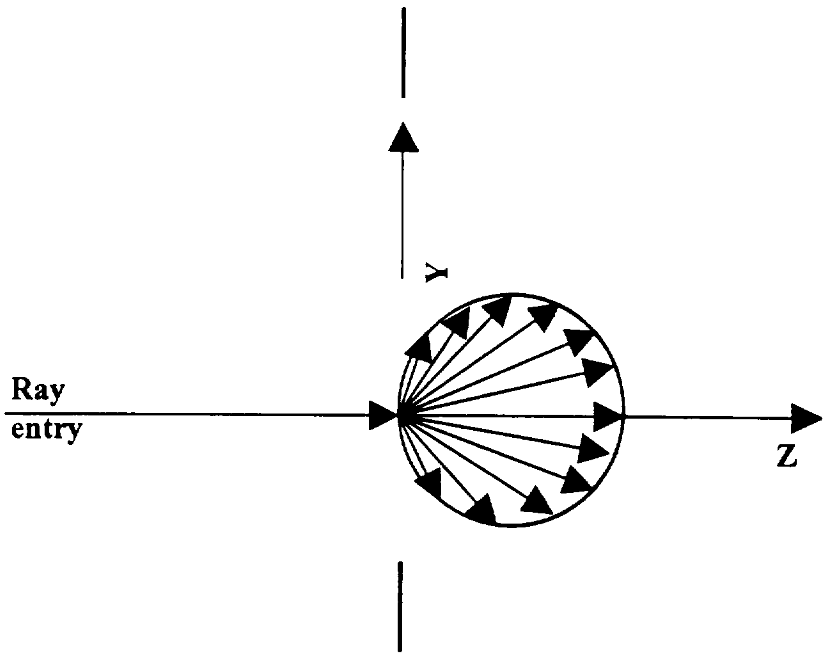

Figure 4.18 Model of a point source of rays entering a slit when employing the Huygens-Fresnel principle with the Rayleigh/Sommerfeld obliquity factor applied.

4.3.3 Application of Model 2

The implementation of Model 2 in the Monte-Carlo ray-trace environment for the prediction of the far-field diffraction pattern involves firing energy bundles uniformly and randomly across the aperture towards the observation screen which is divided into a large number of bins, as in the statistical model. In this case, however, the angle of diffraction is chosen so that all angles are equally probable (diffusely scattered) rather than following a normal distribution. The length of the path that each energy bundle travels and the angle at which it is diffracted are substituted into a modified form of equations 4.26 and 4.29. Taking the amplitude of the electric field of a given energy bundle to be

$$E_{eb} = K(\phi_i, \phi_d)\frac{\mathrm{Sin}(\beta)}{\beta}, \tag{4.33}$$

where

$\beta = 2\ell\frac{\pi}{\lambda}$ and ℓ is the path length. After a large number of rays has been fired (e.g. one million), the final intensity in a given bin on the observation screen is the square of the sum of all of these electric fields due to energy bundles arriving at this bin from all parts of the aperture, given by

$$I_{bin} = \left[\sum E_{eb}(\text{bin})\right]^2 . \tag{4.34}$$

Determining I_{bin} for all bins on the observation screen and dividing by the maximum intensity arriving in any of the bins provides the normalized intensity along the observation screen. This technique was tested on two configurations, chosen so that the diffraction would be in the Fraunhofer diffraction regime.

4.3.4 Results from the application of Model 2

The results from the application of Model 2 are presented as normalized intensity compared with the normalized closed-form analytical solution. Figure 4.19 presents the results from application of this approach to an infinite, 0.3-mm-wide slit with energy entering at the wavelength of 0.58 μm, and an aperture-to-screen distance of 2 m.

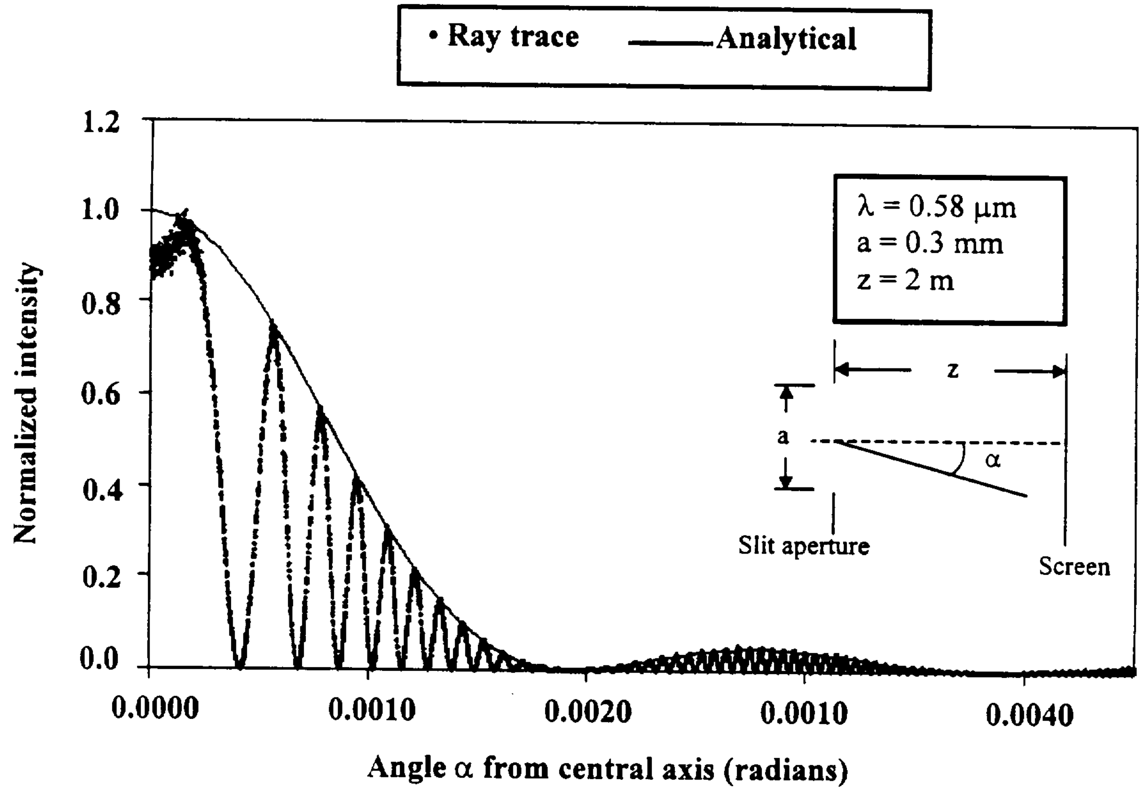

Figure 4.19 Comparison of results from application of modified Huygens-Fresnel principle and analytical solution for far-field diffraction from an infinite slit.

Note that this approach produces a pattern with high-frequency oscillations in intensity, whose peaks lie within an envelope that matches the closed-form analytical solution quite well.

It is interesting to study the application of Model 2 to other aperture shapes, such as a circular aperture. A circular observation screen divided into bins consisting of equal-area rings is placed behind this aperture, and the same procedure is followed to obtain a plot of intensity with angle from the central axis. The case studied involved a circular aperture 0.2 mm in diameter with entering energy of wavelength 9 μm, and aperture to observation screen distance of 16 m.

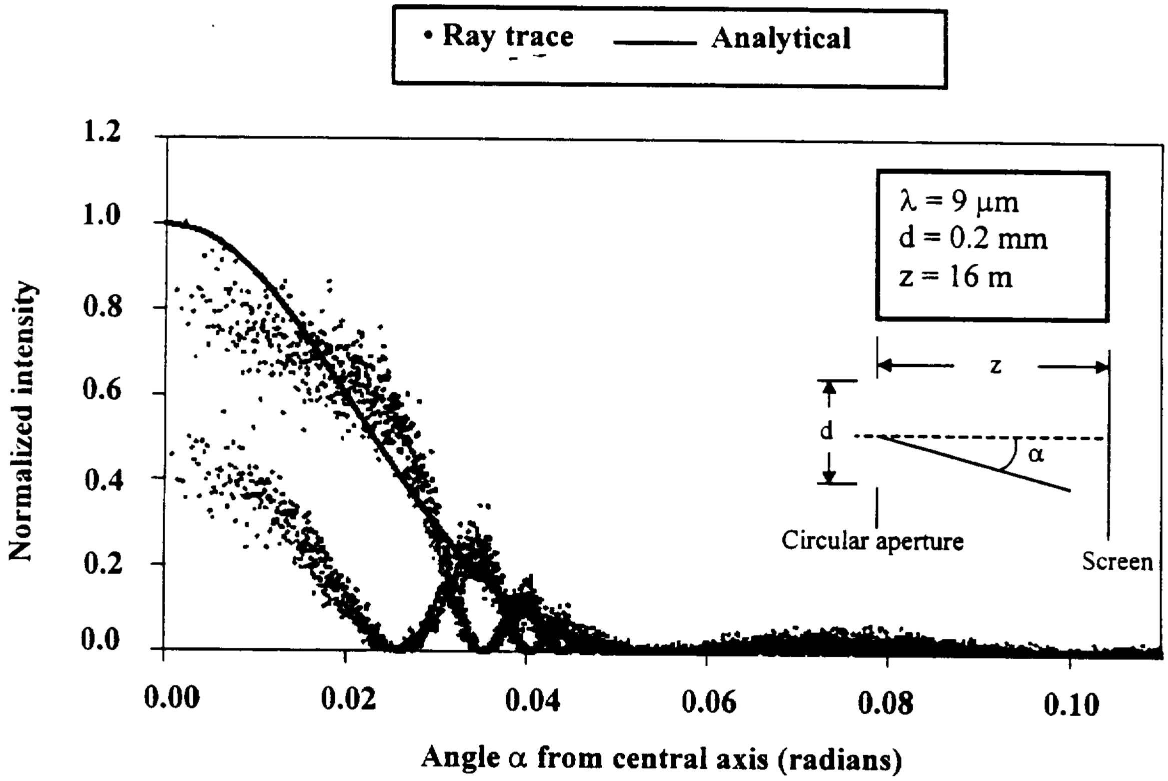

Figure 4.20 Comparison of results from application of modified Huygens-Fresnel principle and analytical solution for far-field diffraction from a circular aperture.

The resulting intensity pattern shown in Figure 4.20, when compared to the analytical solution, is more difficult to interpret than that for the infinite slit. For this case, two oscillating patterns, or orders, occur which together form an envelope that approximately matches the analytical solution. The oscillating intensity patterns seen in both cases occur for reasons that are not clear. For the case of the slit, the resulting pattern is similar to that formed by radiation passing through multiple closely-spaced slits [Hecht and Zajac, 1974]. The agreement between the diffraction predicted by this model, and the closed-form analytical solution will occur in certain cases when the Fraunhofer condition applies, described in Sections 4.3.5 through 4.3.7. Otherwise, the simplifying assumptions break down, and we can no longer expect good results from this application of the modified Huygens-Fresnel principle [Hecht and Zajac, 1974]. The FORTRAN code used to generate these results is provided in Appendix B.

4.3.5 Limitations of the Huygens-Fresnel principle and of Model 2

Because Model 2 is based upon the modified Huygens-Fresnel principle, it is important to understand the limitations of this principle. As stated by Hecht and Zajac [1974], in cases in which the aperture is very large, and the point of observation is far away, the Huygens-Fresnel principle should, and does, work very well. However, for cases involving a very small aperture, or when the point of observation is in the vicinity of the aperture, deviation from the behavior predicted by the Huygens-Fresnel principle should be appreciable. Here, the size of the aperture refers to the aperture dimensions relative to the wavelength of the entering radiation. These limitations imply that Model 2 may properly model diffraction only for configurations where $\Delta\xi < 1.0$, and where the aperture width-to-wavelength ratio (a/λ) exceeds some minimum value. In order to investigate these limitations, several cases were studied in which the value of $\Delta\xi$ and the aperture width were held constant, while the ratio of a/λ was varied. These cases were studied by comparing the closed-form analytical solution of the diffraction pattern with the results predicted by Model 2.

The case study involved modeling diffraction by an infinite, 60 μm-wide slit. The wavelength of the entering radiation and the aperture-to-observation screen distance were varied so that $\Delta\xi$ was a constant 0.4. Five cases were studied, whereby a/λ was assigned the values of 4.0, 1.5, 1.0, 0.5, and 0.25. The results from this study are provided in Section 4.3.6.

4.3.6 Results from case study

Model 2-predicted results shown in Figure 4.21 agree well with the analytical solution (the envelope containing the peaks of the oscillating pattern predicted by Model 2 approximately match the closed-form analytical solution). For this case, the entering wavelength is four times smaller than the aperture width and the observation points are far from the aperture; as expected, the Huygens-Fresnel principle works well. Figure 4.22 demonstrates the declining performance of the Huygens-Fresnel principle as the wavelength of the entering radiation approaches the width of the slit. Here the central maxima is outlined by the peaks of the oscillating pattern predicted by Model 2, but the secondary fringes are lost entirely. The results shown in Figure 4.23 are for the case in which the entering radiation is of the wavelength equal to the slit width. These results are beginning to lose the ability to predict even the shape of the central maxima. As the entering wavelength is made larger than the slit width, Model 2 produces highly erroneous results, as illustrated in Figures 4.24 and 4.25.

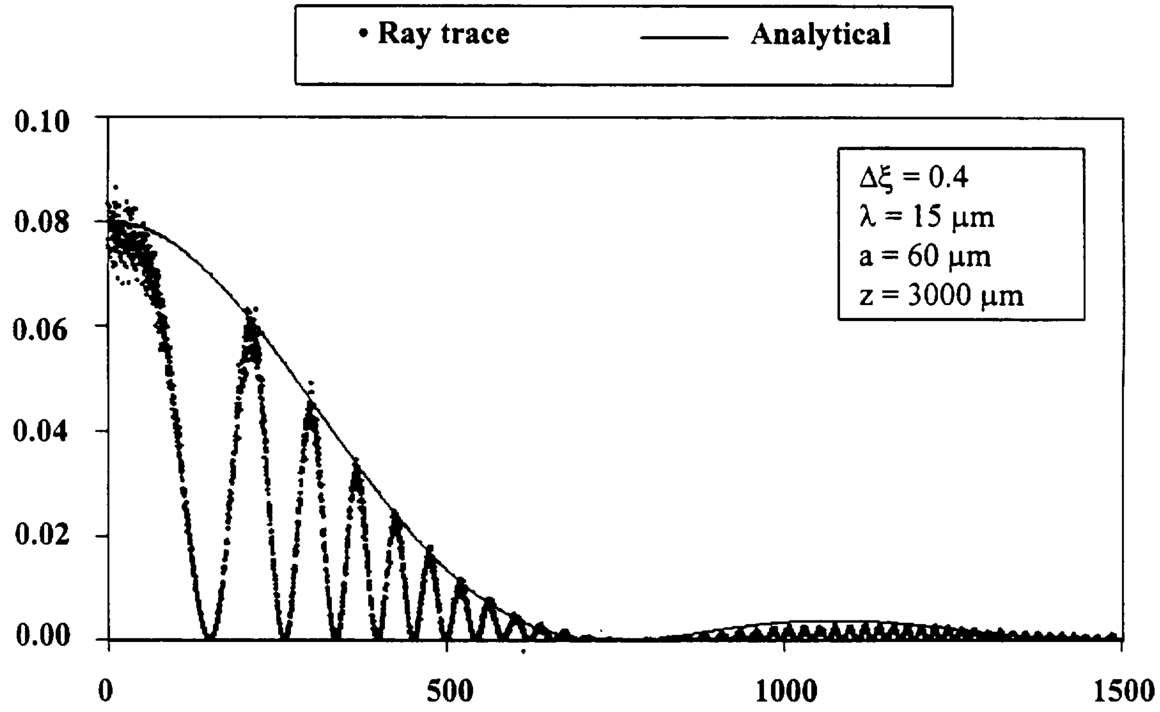

Figure 4.21 Comparison of results from application of modified Huygens-Fresnel principle and analytical solution for far-field diffraction from an infinite slit aperture for which $\Delta\xi = 0.4$ and $a/\lambda = 4.0$.

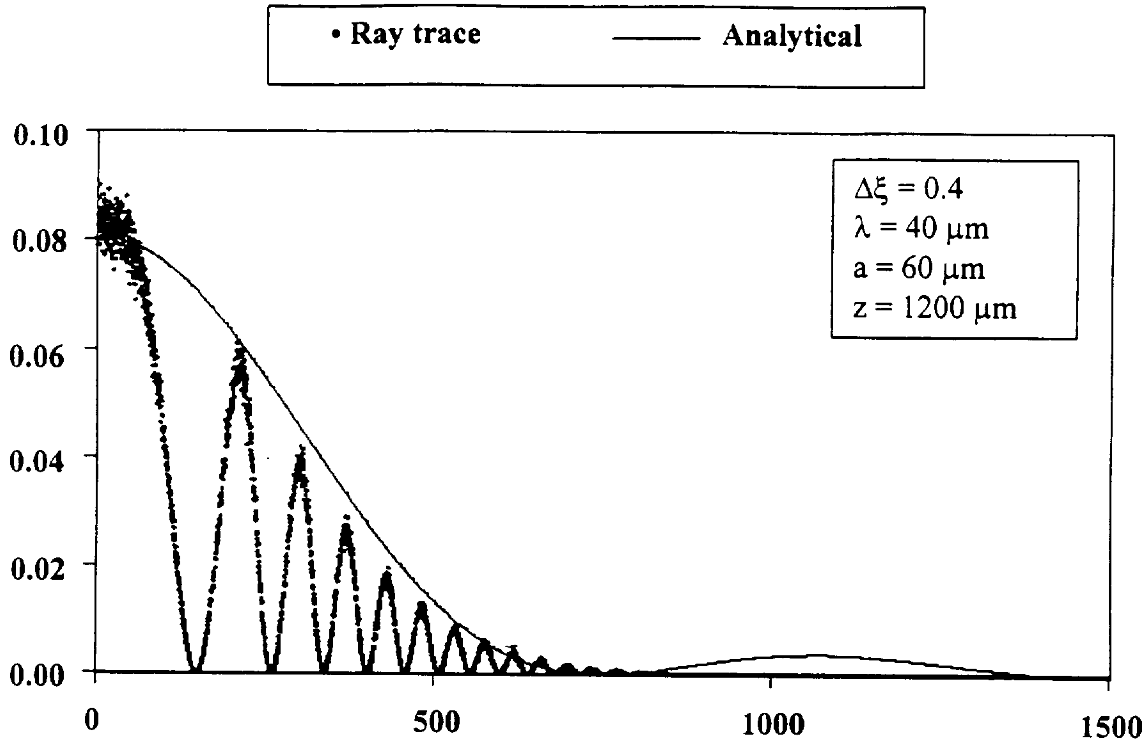

Figure 4.22 Comparison of results from application of modified Huygens-Fresnel principle and analytical solution for far-field diffraction from an infinite slit aperture for which Δξ = 0.4 and a/λ = 1.5.

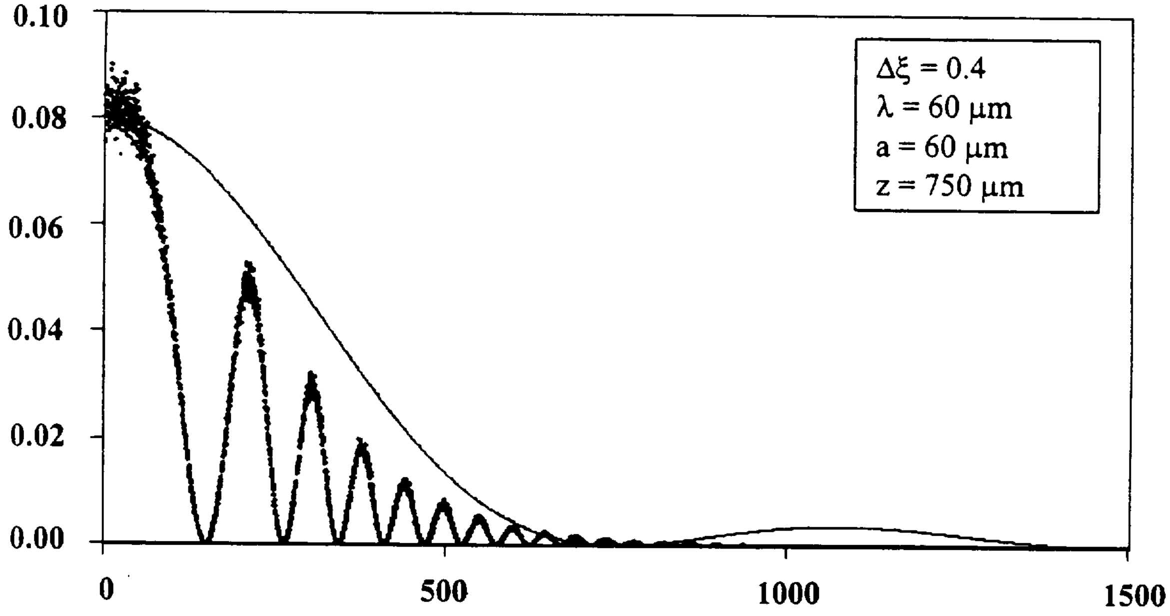

Figure 4.23 Comparison of results from application of modified Huygens-Fresnel principle and analytical solution for far-field diffraction from an infinite slit aperture for which Δξ = 0.4 and a/λ = 1.0

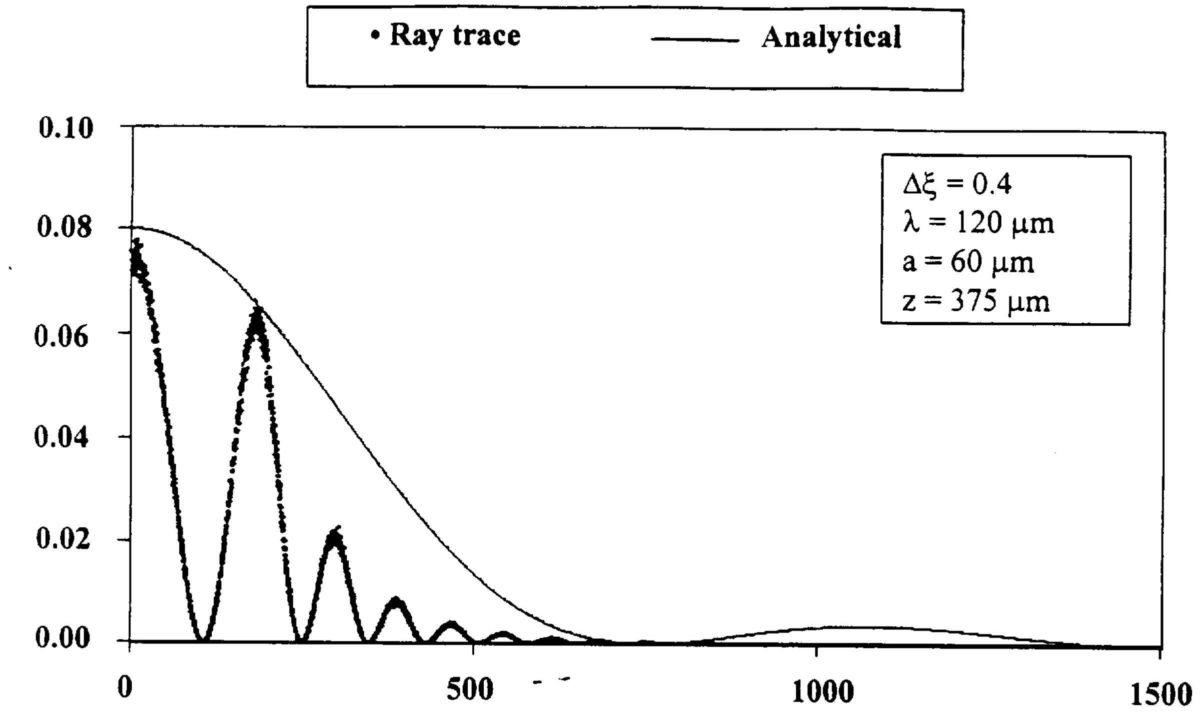

Figure 4.24 Comparison of results from application of modified Huygens-Fresnel principle and analytical solution for far-field diffraction from an infinite slit aperture for which $\Delta\xi = 0.4$ and $a/\lambda = 0.5$.

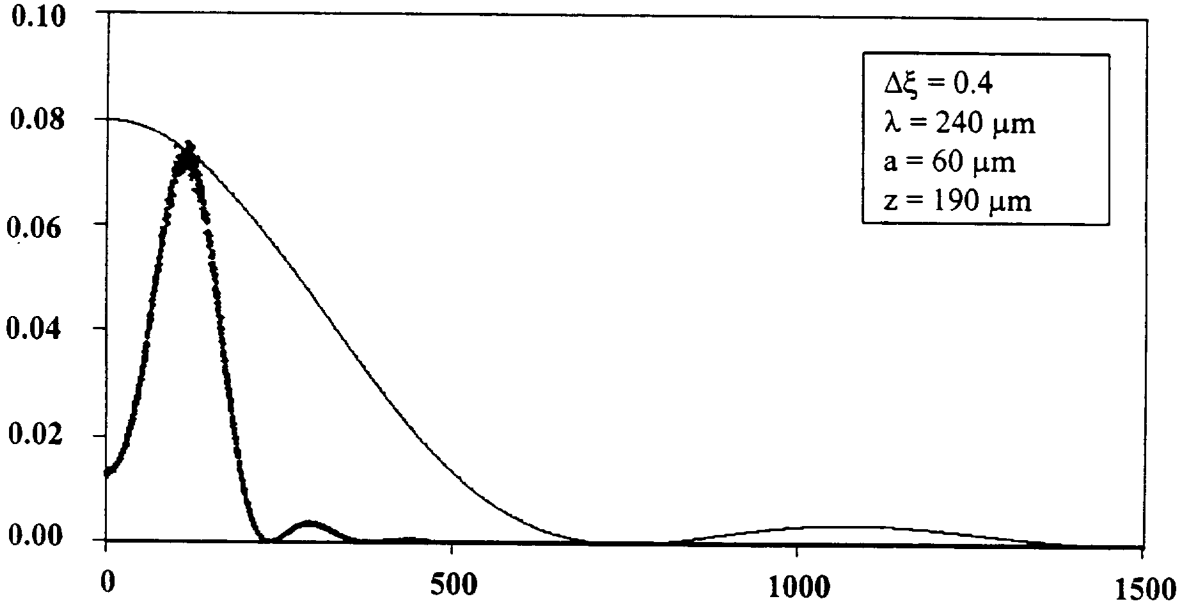

Figure 4.25 Comparison of results from application of modified Huygens-Fresnel principle and analytical solution for far-field diffraction from an infinite slit aperture for which $\Delta\xi = 0.4$ and $a/\lambda = 0.25$.

4.3.7 Conclusions: Model 2

The results from the case study described in Section 4.3.6 suggest that Model 2 will approximate the diffraction pattern of radiant energy entering an aperture, including the secondary maxima only if $\Delta\xi < 1.0$, and $a/\lambda >> 1.0$. Results indicate that as long as $a/\lambda >$ 1.0, application of Model 2 will not lead to highly erroneous results, but the details of the secondary fringes may be lost. However, if $a/\lambda < 1.0$, Model 2 should not be applied as its underlying principles are no longer sound.

4.4 Conclusions: Model 1 versus Model 2

The statistical model is the most general choice for the modeling of diffraction in a Monte-Carlo environment, as it can approximate interference patterns caused by the diffraction of energy for both near and far-field conditions. This model cannot be modified to predict the fringes about the central maxima by keeping track of phase angle (β) as is done in the second model. This impossibility is due to the requirement that all points on the aperture contribute equally to all bins on the observation screen for the formation of an interference pattern. In other words, the number of arriving rays (coming from any randomly located point on the aperture) must be the same for each bin, but the resulting intensity is given by the sum of the intensity from each individual ray, weighted by its phase angle. In the statistical approach, this criterion is not met, as the distribution of energy from a given point on the aperture is not diffusely distributed, but follows a normal distribution. Model 2 can only be used with good results for a restricted set of conditions, otherwise the underlying assumptions break down and it behaves very poorly.

4.5 Potential future investigations of diffraction models

The model based upon the modified Huygens-Fresnel principle (Model 2), and the cause of the oscillating intensity pattern it predicts, should be further investigated. Other case studies similar to the one presented in Section 4.3.6 could be conducted to determine the generality of the conclusions in Section 4.3.7. Another unexplored aspect of the diffraction of radiant energy by an aperture involves the behavior of radiation as it approaches an aperture (prior to entry through the aperture), and the possibility of backwards diffraction. The geometric theory of diffraction described in Chapter 3.0 does model both forward and backward diffraction of energy as it approaches an aperture, and may be capable of properly modeling this behavior. Useful future work could also involve the development of an approach to scale ray-trace results to match the analytical curve for the statistical method, as the current method involves simply scaling the results "by eye" until the area under the ray-trace curve appears to match that of the analytical curve.

5.0 NEXT-GENERATION INSTRUMENT CONCEPTS

Studies of the potential next-generation earth radiation budget instrument, PERSEPHONE, as described in Chapter 2.0, require the use of a radiative model of the CERES and/or modified CERES telescope. The first task of the current effort was to develop such a model which is flexible enough to perform the required studies. Repeating the research objectives of this thesis topic, the first goal is to determine the maximum number of detectors that can be placed in the current CERES telescope without the loss of Optical Point Spread Function (OPSF) quality. The other principal objective is to investigate the possibility of using hyperbolic mirrors in place of the current spherical mirrors in order to maximize the number of channels that can be fitted into the current CERES envelope, thus maximizing the science data return. Descriptions of these studies, and their results are presented in this chapter.

5.1 Development of the radiative model of the CERES optics

Members of the Thermal Radiation Group have developed several radiative models of the CERES and ERBE telescopes. Meekins [1990] completed a Monte-Carlo-based numerical model to study the optical and radiative characteristics of the ERBE scanning radiometer. Bongiovi [1993] later modified Meekins' code, adding baffles in order to model the CERES instrument. Bongiovi's code consists of 16,632 lines of commented FORTRAN code, and is specific to the CERES geometry. Modification of this code to conduct the study at hand would be a formidable task. Instead, a new radiative model was developed using a tool which is being developed by Félix Nevárez, a doctoral student in the Thermal Radiation Group. This tool consists of a C^{++} class library which can represent quadric surfaces, such as cylinders, spheres, planes, and cones with specified surface absorptivity and specularity ratio. The radiative model of an instrument can be developed by modeling each interior instrument surface using one of the library-defined surfaces with appropriate dimensions, and stacking these surfaces to model the entire instrument. After the complete geometry is described, a Monte-Carlo engine module is called, and a user-specified number of energy bundles is directed through the instrument. The paths of these energy bundles are determined by following the rules of the Monte-Carlo ray-trace method as it applies to radiation heat transfer. The output from the execution of this C code is a file of the distribution of energy bundles arriving on a surface of interest.

5.1.1 Modeling the CERES geometry

In the present instrument study, the surface of interest is the plane which would contain an array of thermistor bolometer detectors, located beneath the precision aperture pictured in Figure 5.1 (b). Figure 5.1 (a) demonstrates how the CERES telescope is broken down into 46 basic surfaces. The numbering scheme corresponds to the numbering used in the code provided in Appendix C. Note that with the use of this new tool, the author needed only to write 616 lines of commented C code which calls the C^{++} library functions, and 224 lines of FORTRAN code for post-processing the output files, for a total of 840 lines of code. When compared to Bongiovi's 16,632 lines of FORTRAN required to achieve the same task, this new code proves to be a remarkable tool in radiometric instrument design.

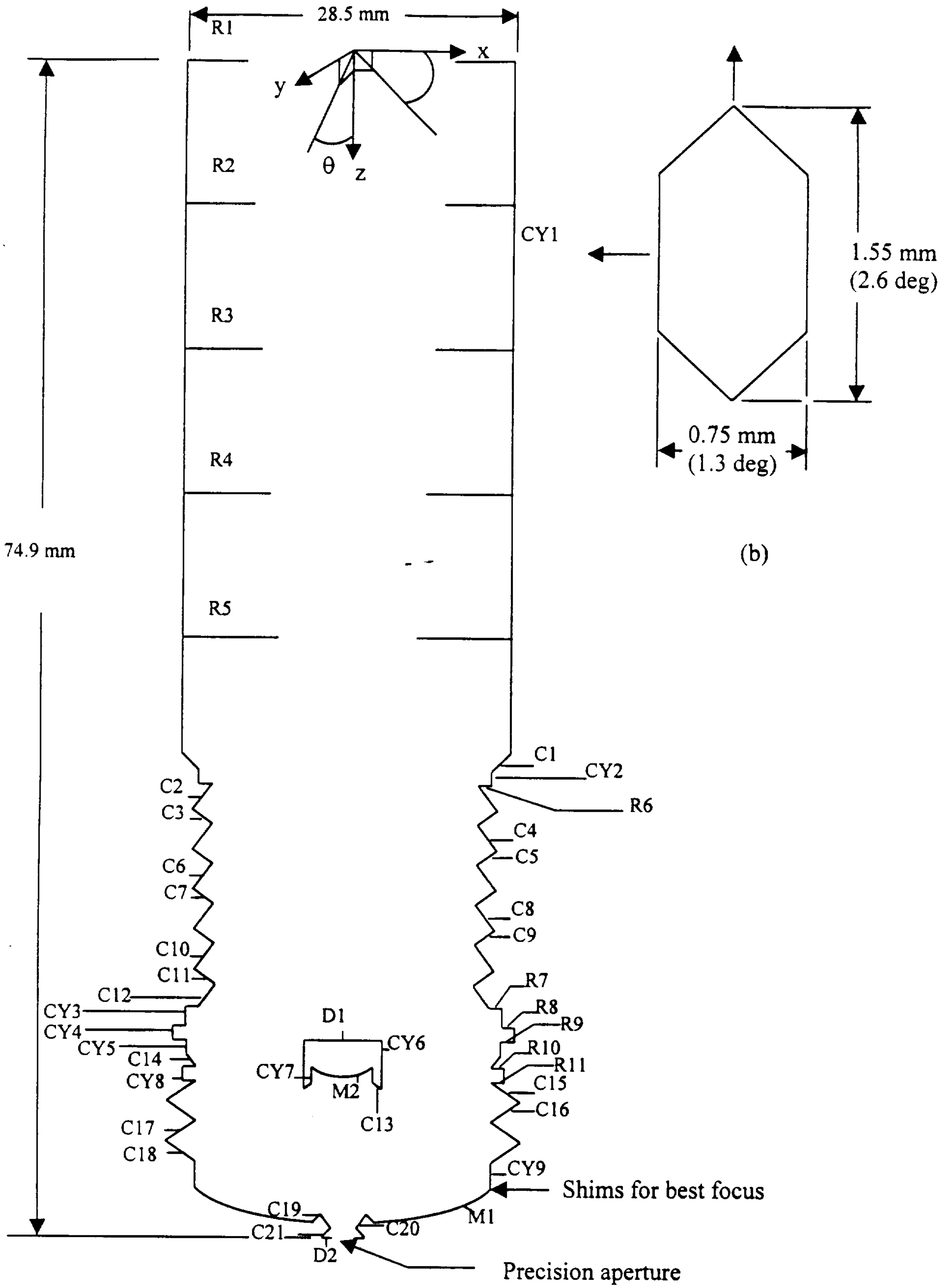

(a)

(b)

Figure 5.1 (a) Illustration of components of CERES geometry, excluding the "spider legs" which support the secondary mirror (not drawn to scale), and (b) the precision aperture in CERES telescope.

In addition to the ease of performing radiometric analyses, this new ray-trace environment is equipped with a useful graphical user interface. After entering the telescope geometry, it can be viewed by specifying all of the surfaces as diffuse and firing rays into the telescope. Figure 5.2 shows the CERES telescope with the primary mirror removed, as produced by this graphical user interface.

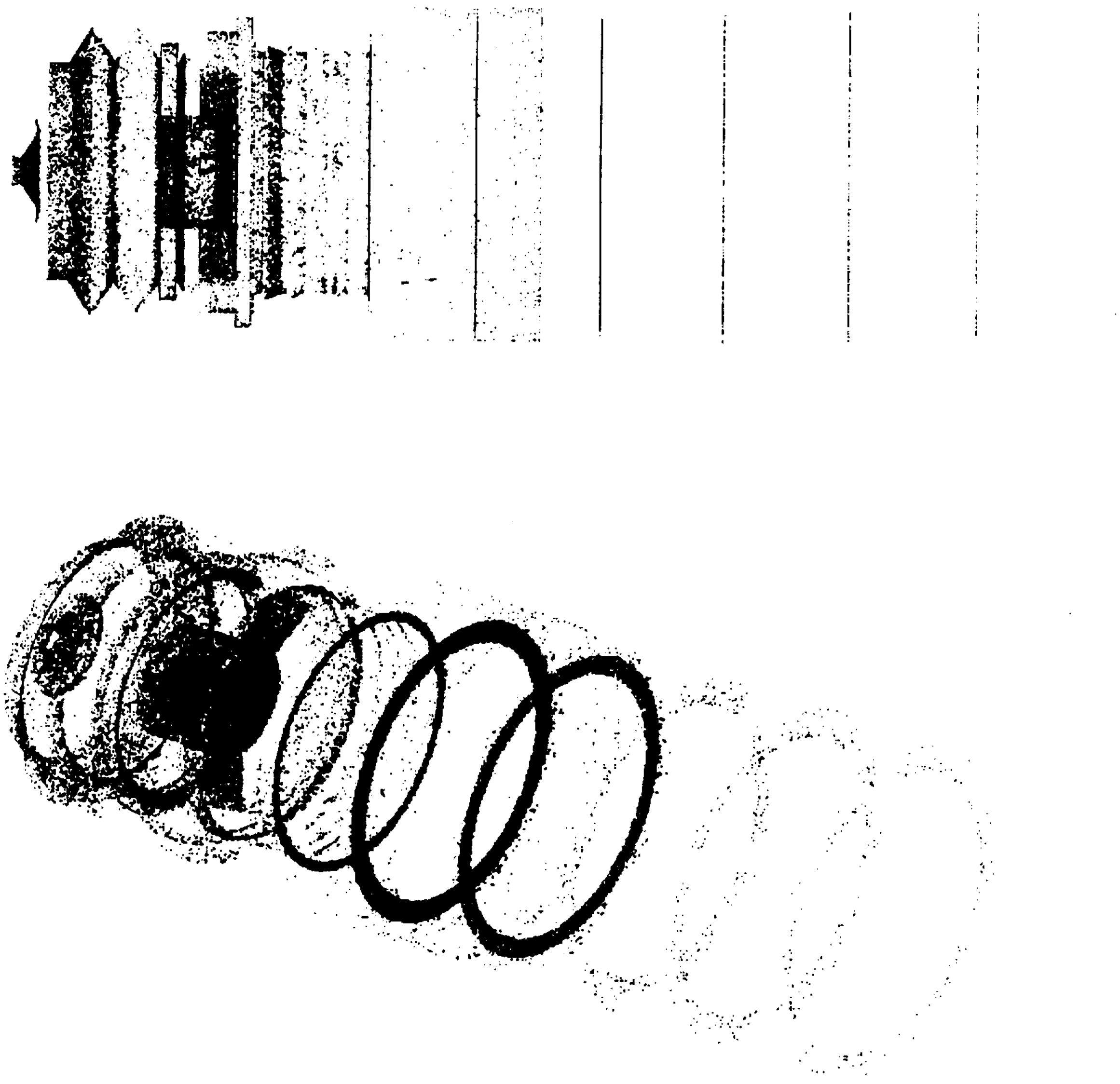

Figure 5.2 CERES telescope geometry, as produced by graphical user interface of the new ray-trace environment.

5.1.2 Addition of shims for blur circle minimization

As described in Chapter 3.0, the presence of spherical aberration in an optical system causes the spot size at the point of "best focus" to be finite. This spot of finite diameter is called the blur circle. It is desired that the location of the minimum blur circle occur at the plane containing the precision aperture so that the edges of the Optical Point Spread Function demonstrate the steepest drop-off possible (i.e. approach a "top-hat" response). The location of the "best focus" is very sensitive to the distance between the primary and secondary mirrors. Upon placing the parts between these mirrors, tolerance stack-up occurs so that the location of the minimum blur circle will likely not occur at the plane containing the precision aperture. The spacing between the mirrors is thus increased by the addition of very thin shims until the blur circle is a minimum at the precision aperture. This addition of shims was simulated using the computer model of the CERES telescope. The distance between the mirrors was gradually increased, and a scattergram representing the blur circle was plotted until the distance providing the minimum blur circle was found. The change in the image at the focal plane due to slight changes in the primary-to-secondary mirror spacing is illustrated in Figure 5.3. The quantity δ refers to the total thickness of the shims added. When δ = 0.28 mm, the minimum blur circle is obtained, as illustrated in Figure 5.3 (b). Note that the structure which supports the secondary mirror, the "spider", is imaged in the defocused images shown in Figures 5.3 (a) and (c).

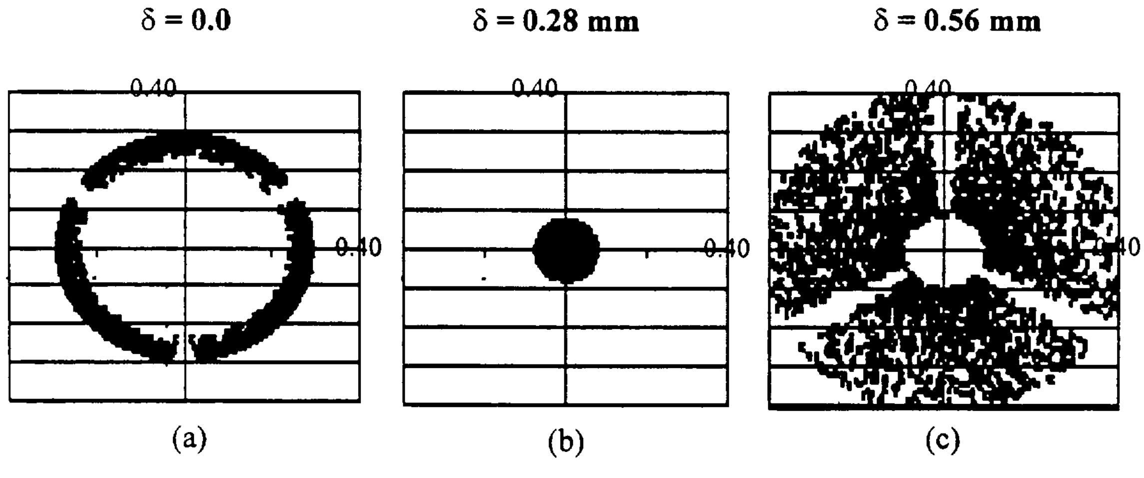

δ = 0.0 δ = 0.28 mm δ = 0.56 mm

(a) (b) (c)

Figure 5.3 Illustration of change in the images at the precision aperture for different shim thicknesses, where δ is the shift due to the addition of shims (dimensions in mm). (a) Defocused image, (b) image at best focus where the blur circle diameter is a minimum, and (c) defocused image.

5.2 Capabilities of the current CERES instrument

5.2.1 Determination of the Optical Point Spread Function of the current CERES instrument

The OPSF (Optical Point Spread Function) of an instrument shows how collimated energy entering from various angles is transmitted through the instrument. The OPSF has previously been determined for the CERES telescope with only a single aperture using Bongiovi's model [Priestley, 1997]. This OPSF exhibits attenuation at the edges of the field due to the finite blur circle. If the blur circle were infinitely small, as in an ideal optical system, this edge attenuation would be absent from the OPSF. This ideal OPSF would be perfectly flat across the aperture area, and would drop immediately to zero beyond the edges. Instead, attenuation occurs before the physical edge of the field stop is reached, and radiation arrives at the detector beyond the projection of the area of the field stop on the detector. A complete description of the significance of the blur circle is presented by Priestley [1997].

Equivalence is assumed in the determination of the OPSF of the CERES telescope. This assumption implies that regardless of the point at which a given amount of energy arrives at a thermistor bolometer detector, the response of the detector is the same.

In order to determine the OPSF over more than one aperture using the new radiative model, collimated radiation was allowed to arrive at angles θ, ϕ (see Figure 5.1 (a)) and traced through the instrument. The output file for a given combination of angles consists of the x, y coordinates of all energy bundles arriving at the plane containing the precision aperture. In order to determine how much of this arriving energy enters one of the precision apertures, each output file must be opened and read, line by line. If the coordinates of a line of output fall within the area defined by of one of the precision apertures, then an energy bundle will reach the detector below, and a counter for that aperture is incremented. After all lines of all output files have been read, the results are the number of energy bundles arriving to each detector for each set of input angles θ, ϕ. This is the information needed to construct the OPSF of the instrument. The FORTRAN code used to perform this post processing is provided in Appendix C. Figures 5.4 and 5.5 show the resulting OPSF of the current CERES instrument with five (5) apertures and two (2) apertures, respectively. Section 5.2.3 provides an interpretation of these figures.

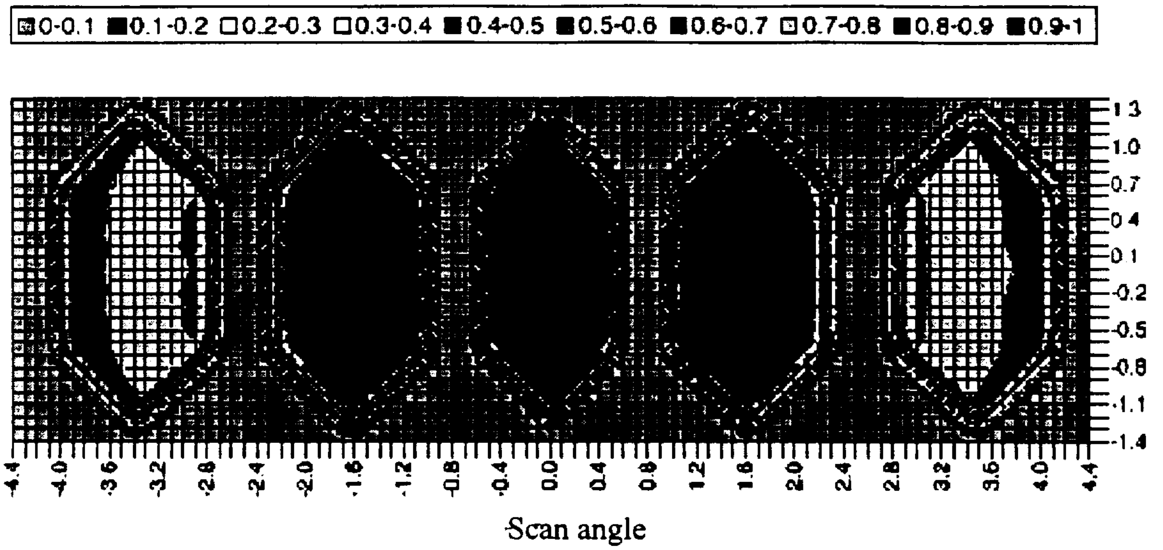

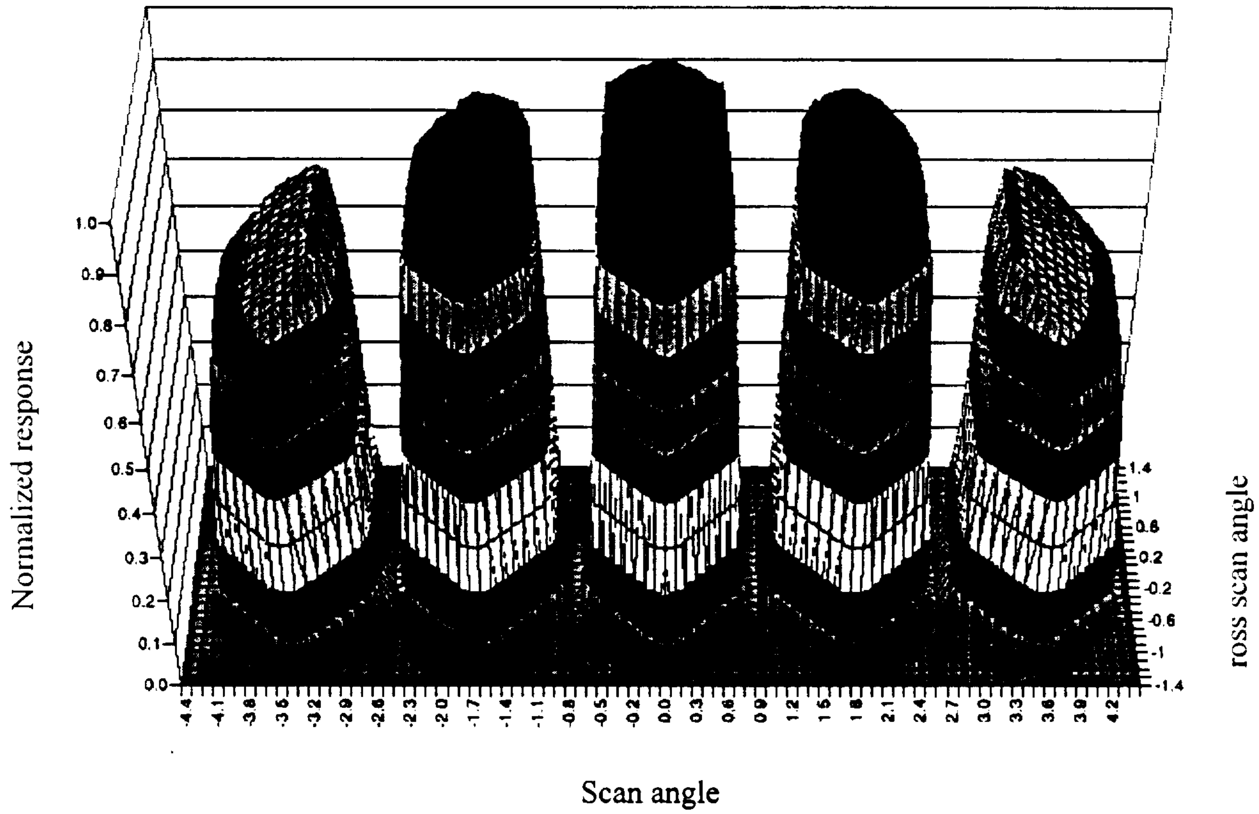

Figure 5.4 OPSF for the current CERES telescope (minus the primary mirror insert) with five (5) precision apertures.

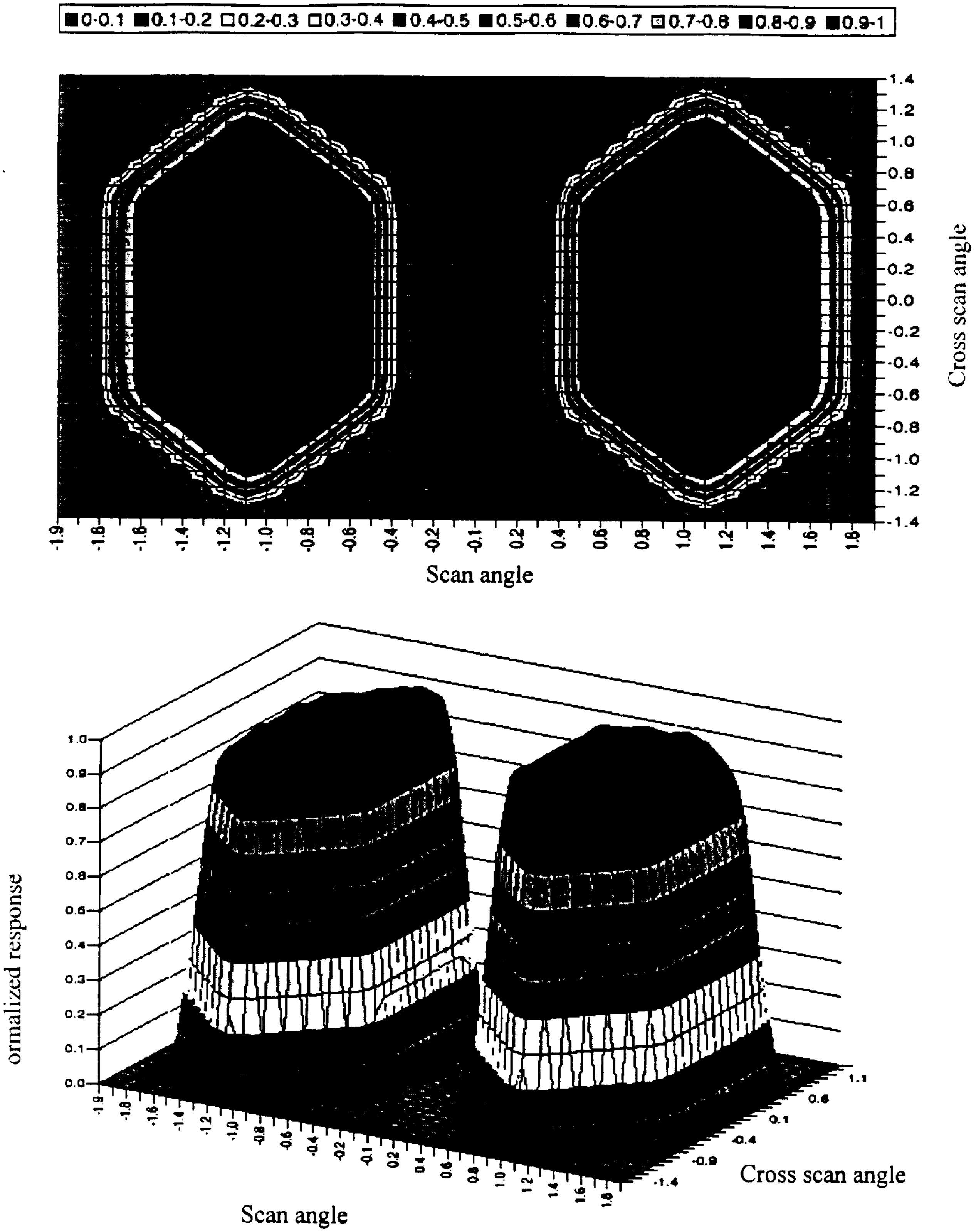

Figure 5.5 OPSF for the current CERES telescope with two (2) precision apertures.

5.2.2 Validation of results

The minimum blur circle found in the current study is 0.14 mm in diameter, comparing relatively well with the 0.122 mm diameter blur circle reported by TRW [Carman, 1993]. There is some discrepancy between the OPSF previously determined [Priestley, 1997], and the results of the current research effort in that the cutoff at the edges of the previous OPSF is not as steep as that of the results presented in this thesis. It is believed that this discrepancy occurred because the code used in the previous study did not model the telescope at best focus. Figure 5.6 compares results from the current and previous studies to those predicted by linear optics, and experimental data borrowed from Priestley [1997]. The curve predicted by linear optics was constructed by moving a blur circle of 0.14 mm in diameter across the detector and plotting the fraction of the blur circle area which would fall within the precision aperture. Figure 5.7 shows very good agreement between the results predicted by linear optics and current results, and reasonable agreement with experimental data.

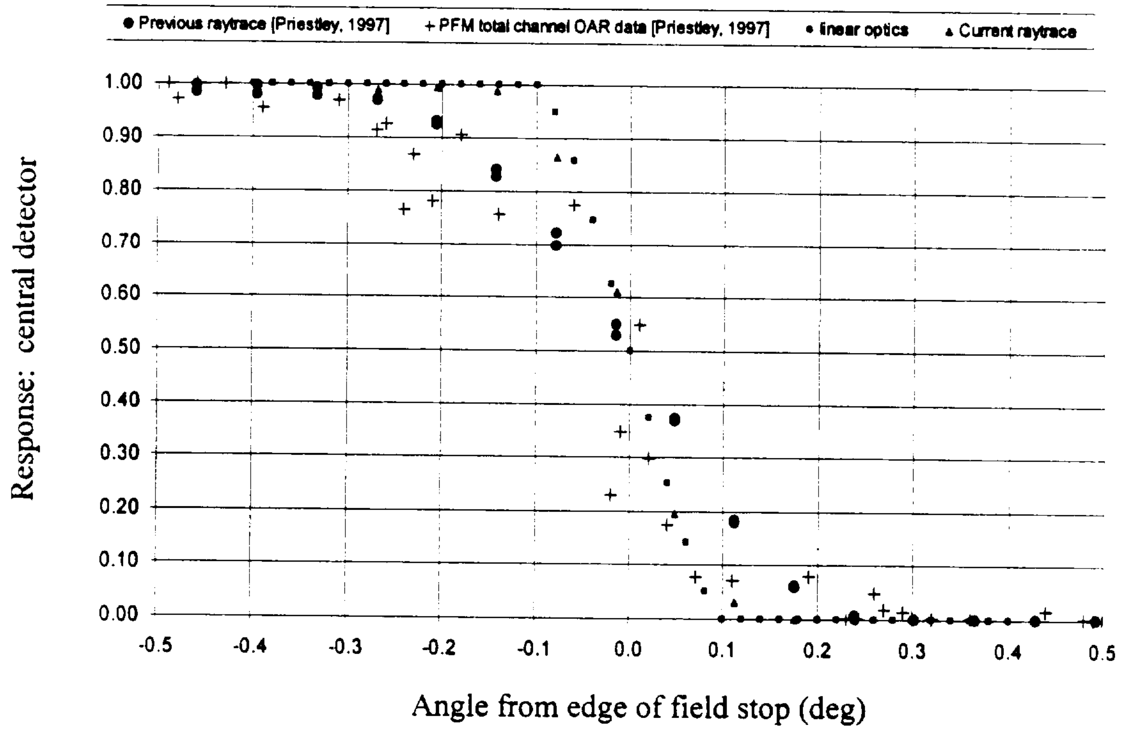

Figure 5.6 Comparison of current results with previous results, linear optics, and experimental data.

5.2.3 Conclusions: Use of existing CERES instrument with spherical mirrors

Figure 5.4 illustrates that the placement of five detectors in the current CERES instrument does not yield acceptable performance. A flat response across all detectors is desired, but a drop off in the response occurs at the two detectors furthest from the central axis. Note that the only modification to the current CERES telescope involved the removal of the primary mirror insert. Figure 5.5 shows that the placement of two detectors within the current CERES telescope does yield acceptable results, as the response is flat over the two detectors. It can be concluded that the capability of the current CERES instrument can be doubled by the addition of another detector in each telescope without sacrificing the quality of the OPSF. As previously mentioned, this modification would pose other challenges such as the possibility of optical cross-talk between channels.

5.3 Replacement of spherical mirrors with hyperbolic mirrors

5.3.1 Optical prescription for hyperbolic mirrors

In initial discussions of the potential next-generation design concept, PERSEPHONE, NASA engineers hypothesized that the replacement of spherical mirrors with hyperbolic mirrors within the same telescope could yield an instrument with good throughput over a significantly larger field of view, and with the same or smaller size blur circle. The basic parameters and layout of the current and potential future mirror systems are illustrated in Figure 5.7. The primary-to-secondary mirror spacing (vertex-to-vertex) is to be held the same, and only the curvatures and conic constants of the mirrors are to be changed. NASA engineers performed a preliminary study to determine the set of hyperbolic mirrors which met the required spacing and restricted mirror diameters that would yield the best performance. The constraints were entered into a commercial ray-trace code which iterates until finding the optimal combination resulting in the minimum blur circle. The recommended prescription is provided in Table 5.1.

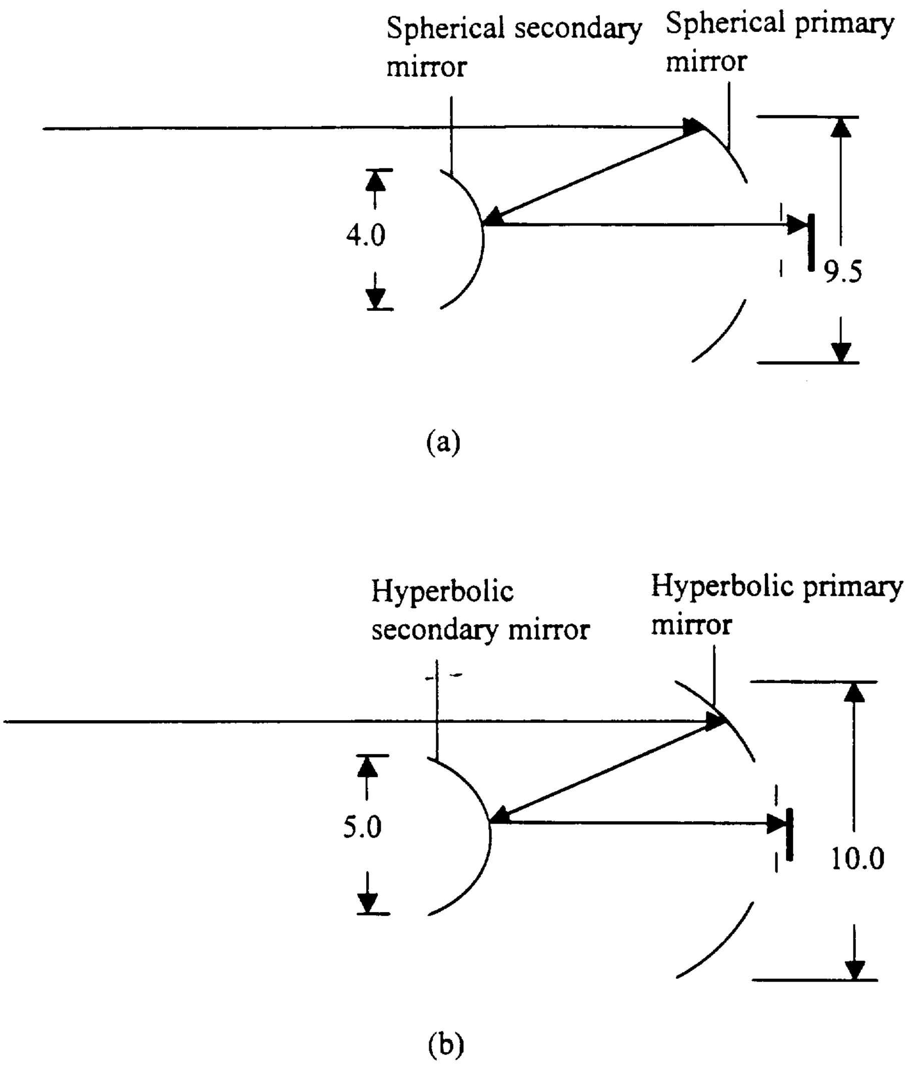

Figure 5.7 (a) Illustration of current CERES spherical mirrors (Modified Cassegrain), and (b) illustration of the new optical prescription with hyperbolic mirrors (Ritchey Crétian Cassegrain) (dimensions in mm).

Table 5.1 Optical prescription for hyperbolic mirrors.

	Primary Mirror	**Secondary Mirror**
r_v (vertex radius)	36.042 mm	32.284 mm
Max R (maximum mirror radius)	10.0 mm	5.0 mm
C.C. (conic constant)	-1.3329	-22.4729
Primary-to-secondary (vertex-to-vertex) spacing:		10.89 mm
Primary vertex-to-detector plane spacing:		2.0 mm

This combination of mirrors is said to yield blur circle sizes of 0.058 mm diameter on-axis, and 0.080 mm at 2.34 mm off-axis. The first objective in conducting this study was to use the new ray-trace tool to duplicate these results using only the mirrors. Upon successfully modeling this mirror combination, the next objective was to determine the Optical Point Spread Function of the hyperbolic mirrors and compare results with that obtained for the spherical mirrors.

In order to model the desired combination of mirrors, the parameters in Table 5.1 had to be converted into input required by the new MCRT environment. Details of this conversion are provided for two reasons: (1) in order to document the approach for future researchers, and (2) in order to clarify the appropriate use of several equations found in [Walkup, 1993], a reference commonly used by members of the Thermal Radiation Group.

5.3.2 Conversion of known parameters to required parameters

In order to specify hyperbolic mirrors using the new MCRT environment, the user must supply the parameters a, b, and c_h, parameters in the standard equation for a hyperboloid given by

$$\left(\frac{z}{c_h}\right)^2 - \left(\frac{y}{b}\right)^2 - \left(\frac{x}{a}\right)^2 = 1.0, \tag{5.1}$$

where a=b for symmetrical optics. The parameters a and c_h are illustrated in Figure 5.8. Note that a is <u>not</u> the outer radius of the mirror slice, as stated by Walkup [1993].

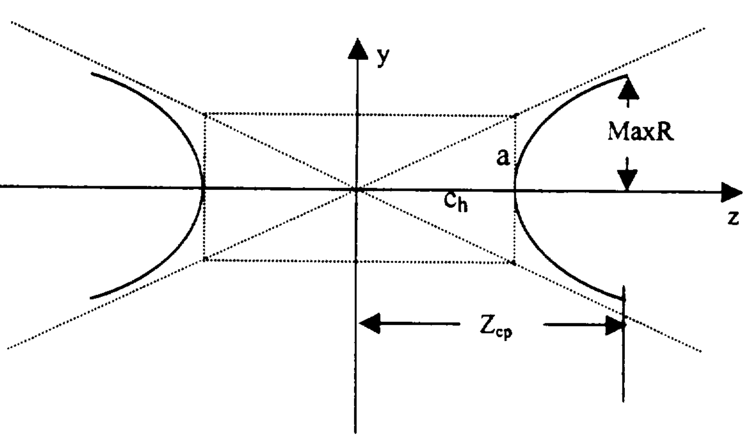

Figure 5.8 Illustration of parameters required for entry of hyperbolic mirrors into new MCRT environment.

Using the two expressions relating the parameters for a hyperboloid,

$$r_v = \frac{a^2}{c_h} \tag{5.2}$$

and

$$C.C. = -\frac{a^2 + c_h^2}{c_h^2}, \tag{5.3}$$

we have two equations and two unknowns. Therefore the parameters c_h and a can be determined. Because these are symmetrical optics, a = b. Finally, the dimension z_{cp}, is a required parameter, and could be found by substituting b = 0, a = Max R, and the value of c_h previously determined into equation 5.1. Using these parameters, the prescribed hyperbolic mirror combination was modeled with the new MCRT environment.

5.3.3 Results

The only results provided from the preliminary study conducted by NASA involved the size of the blur circle at several points on the focal plane. The central blur circle diameter was stated to be 0.058 mm when the vertex-to-vertex distance between mirrors, Δz, was 10.89. A similar result was obtained when the prescribed mirror combination was modeled using the new ray-trace tool, but the shape of this blur circle indicated that the mirrors are not at their best focus when $\Delta z = 10.89$ mm. Increasing Δz slightly resulted in a much smaller blur circle, as shown in Figure 5.9. The configuration yielding the smallest blur circle, where $\Delta z = 10.93$ mm, was used for the remainder of the studies conducted.

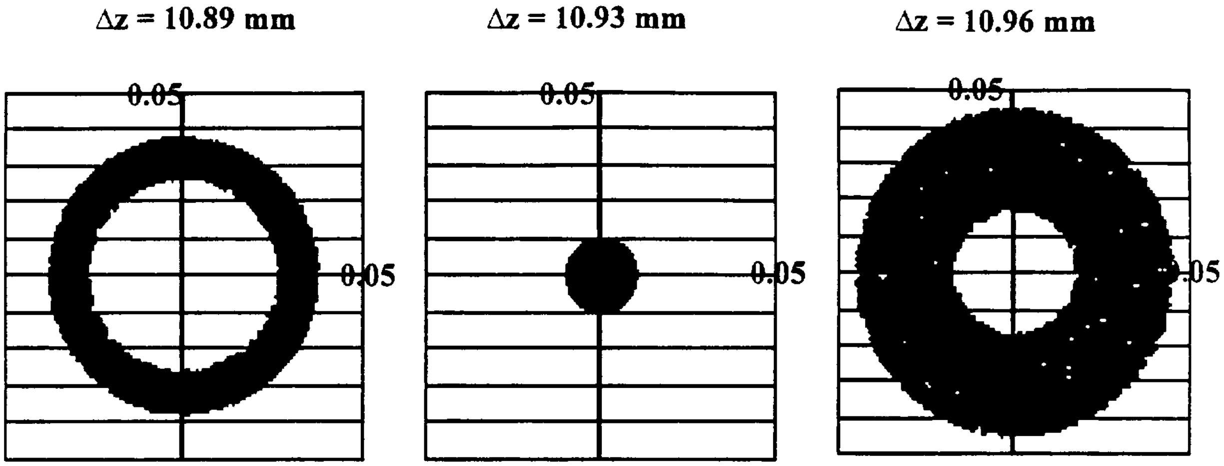

(a) (b) (c)

Figure 5.9 Illustration of blur circle minimization (where Δz indicates the distance between the primary and secondary mirrors) (dimensions in mm). (a) Defocused image, (b) image at best focus where the blur circle diameter is a minimum, and (c) defocused image.

The Optical Point Spread Function (OPSF) for the hyperbolic mirror combination was produced using the new MCRT environment. These results are shown in Figure 5.10 (b) compared to an OPSF generated for the spherical mirrors used in CERES, removed from the telescope (Figure 5.10 (a)). Only one half of the OPSFs are shown, as symmetry about the central axis is expected. Results presented in Figures 5.10 (a) and (b) serve to compare the performance of the spherical and hyperbolic mirror combinations alone, independent of the influence of the telescope geometry. Note that these OPSFs differ from those that would be obtained if the mirrors were placed within the telescope.

It is important to realize that the outer diameters of the hyperbolic mirrors are larger than those of the spherical mirrors; thus, some slight changes in the telescope would be required in order to use the recommended hyperbolic mirrors. NASA stated that this increase in diameter was a requirement for proper performance of the hyperbolic mirrors, and hyperbolic mirrors of the same diameters as the current spherical mirrors would not provide acceptable results.

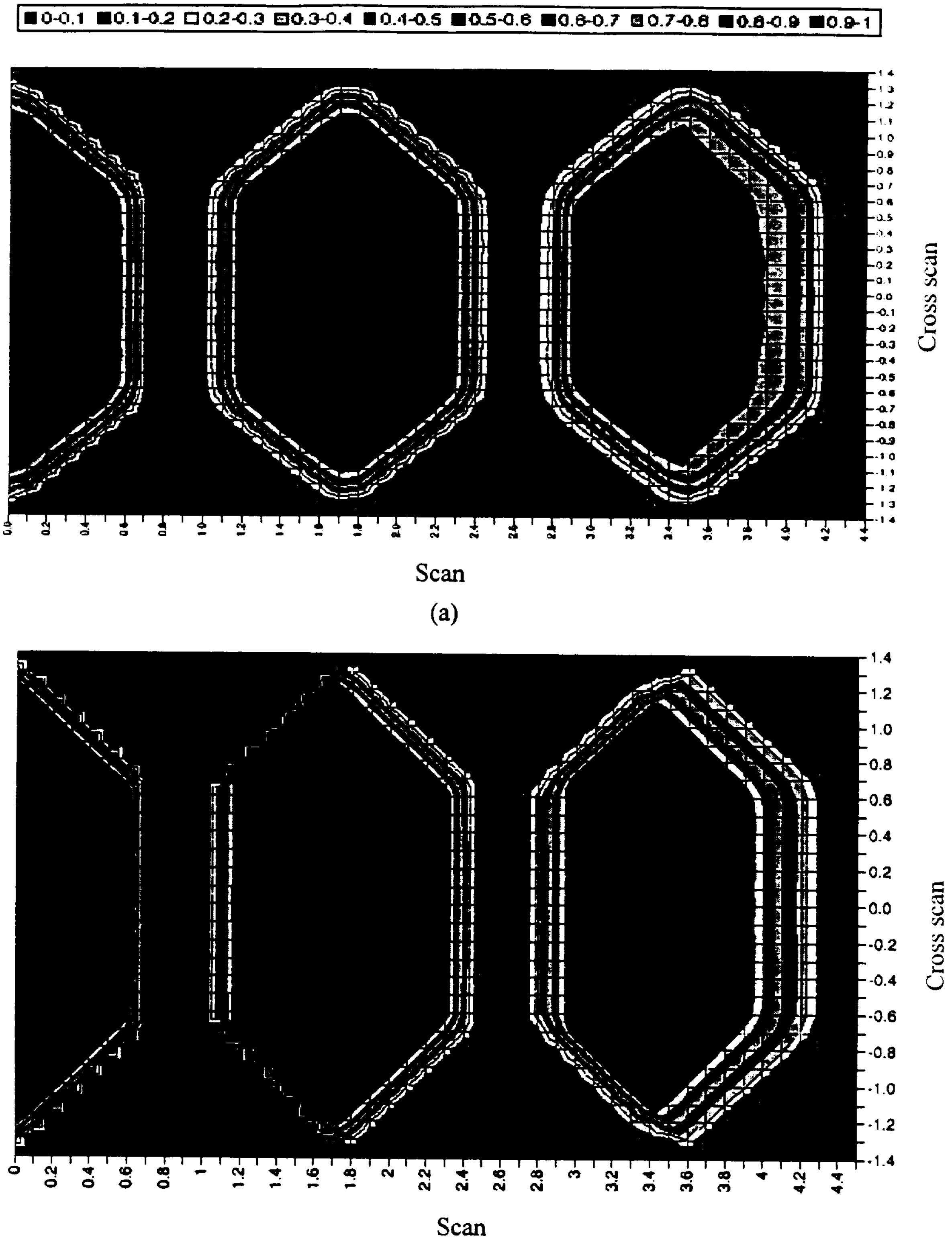

Figure 5.10 (a) OPSF of the current CERES spherical mirrors only, and
(b) OPSF of the prescribed hyperbolic mirrors only (profile view).

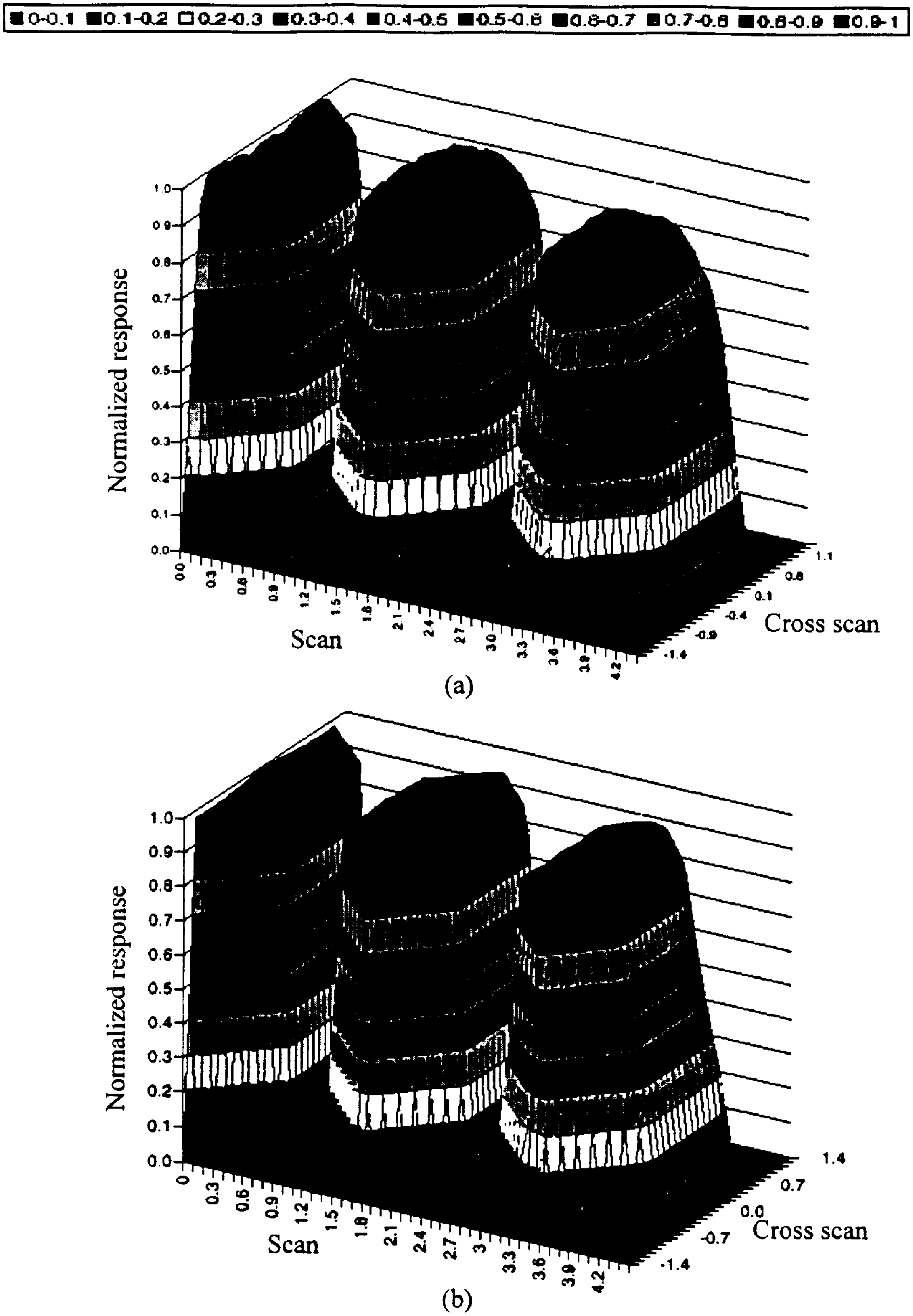

Figure 5.11 (a) OPSF of the current CERES spherical mirrors only, and (b) OPSF of the prescribed hyperbolic mirrors only (relief view).

5.3.4 Conclusions: Hyperbolic mirrors

Figures 5.10 and 5.11 indicate that the hyperbolic mirrors provide the ability to produce a uniform flux over a larger area at the focal plane. Comparison of the OPSF of the spherical mirrors alone, shown in Figures 5.10 (a) and 5.11 (a), with that of the CERES telescope with the spherical mirrors (Figure 5.4) indicates that the drop-off in response is largely due to the manner in which radiation is transmitted through the telescope. (Here we are careful to distinguish between the full CERES telescope model; which includes baffles, secondary-mirror support struts, and other structural members; and an ideal optical system having the same prescription but consisting of only the two mirrors and the precision apertures). The drop-off due to the real telescope geometry would be expected in an instrument containing the hyperbolic mirrors as well, thus results **do not** show that a change in the mirrors will permit the use of five detectors in a given telescope. What is demonstrated is the improved performance of hyperbolic mirrors over spherical mirrors. Note, however that the current spherical mirror combination involves 45 percent obscuration while the hyperbolic mirror combination involves 55 percent obscuration. The result of such an increase in obscuration is less energy throughput and more problems with diffraction.

5.4 Potential future investigations

Future studies could involve the placement of the hyperbolic mirrors into an appropriately modified CERES telescope, and the determination of the resulting Optical Point Spread Function. The new MCRT environment could be used to study the effect of slight modifications of the interior telescope surfaces on the throughput to the detectors.

Another potential study could involve a different detector arrangement within the telescope. For example, instead of inserting extra detectors in a row, the detectors could be placed in some alternative arrangement which provides an optimal throughput to all detectors. One potential rearrangement for the insertion of four precision apertures is illustrated in Figure 5.12.

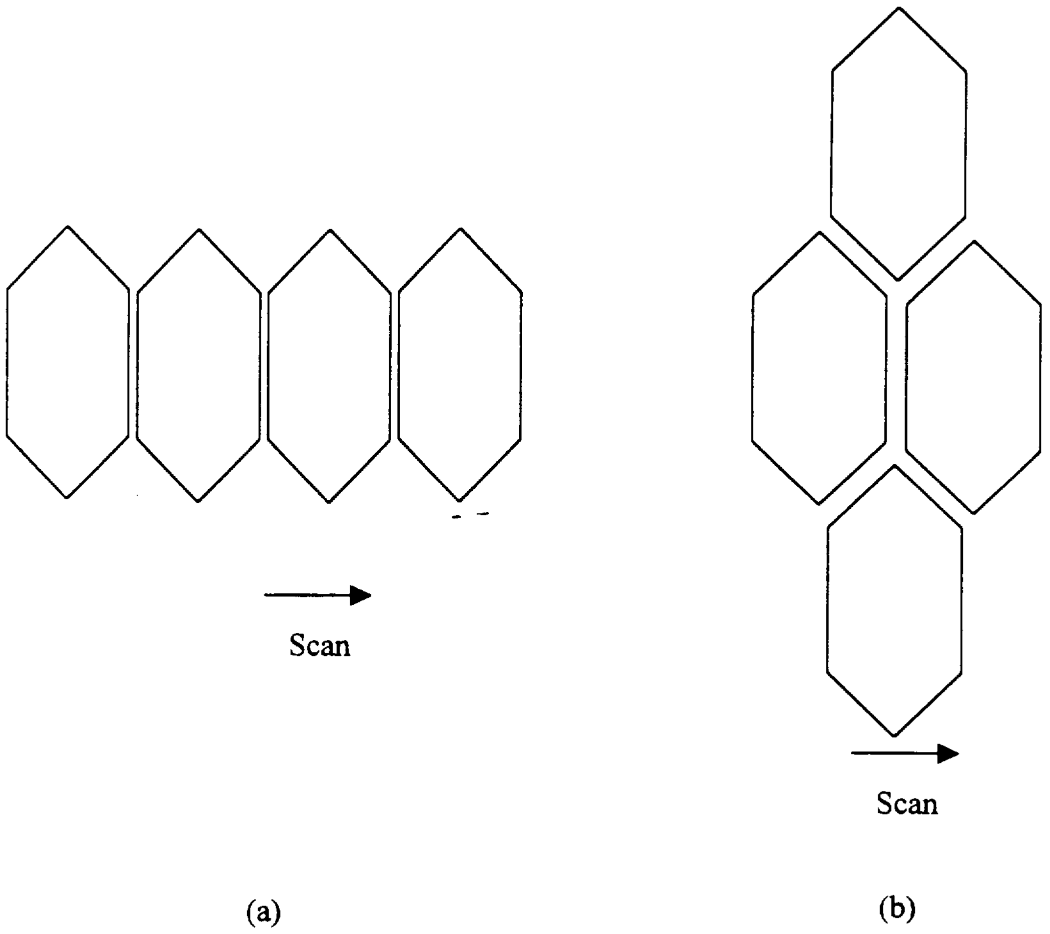

Figure 5.12 (a) Arrangement of precision apertures that has been considered, and (b) a potential arrangement of precision apertures for future study.

6.0 CONCLUSIONS AND RECOMMENDATIONS

6.1 Conclusions: modeling diffraction in the MCRT environment

Two diffraction models for use in the Monte-Carlo ray-trace (MCRT) environment have been described and tested: Model 1, a statistical approach, and Model 2, application of the modified Huygens-Fresnel principle. The derivation and application of these models, and the results that they predict are presented in detail in Chapter 4.0.

The concepts upon which Model 1, the statistical approach, is based were originally proposed by Heinisch and Chou in 1971. The details of the implementation of this model have evidently never been thoroughly documented in the public domain, so they were rediscovered and documented in this thesis. The statistical approach is useful for predicting diffraction in both the Fraunhofer and Fresnel regimes, but does not keep track of phase and thus cannot exactly predict the details, such as the secondary maxima of the expected diffraction patterns. Intensity distributions predicted by Model 1 are smooth curves, which approximate the diffraction patterns predicted by theory. The statistical approach was tested by applying it to a practical example involving the diffraction of radiant energy as it passes through the infinite-slit aperture of a cavity detector developed within the Thermal Radiation Group. This case involves the diffraction of energy along the same coordinate direction due to the two edges of the slit, a situation not discussed in the cited references. A study was conducted to determine the best approach to model this type of situation and it was determined that the final angle of diffraction of an entering energy bundle is best described by the algebraic sum of the angles of diffraction due to each edge.

Model 2 involves the application of the Huygens-Fresnel principle, modified by a correcting obliquity factor. This model is capable of predicting the diffraction pattern, including the secondary maxima, for a limited range of Fraunhofer diffraction configurations. A case study involving diffraction by an infinite slit was conducted to determine the general range of applicability of this model. The results from this study suggest that Model 2 will approximate the diffraction pattern of radiant energy entering an aperture, including the secondary maxima, only if the ratio of the slit width to the wavelength of the entering energy, a/λ, is much less than one. Results indicate that as long as a/λ exceeds one, the application of Model 2 will not lead to highly erroneous results but the details of the secondary fringes may be lost. However, if a/λ is less than one, Model 2 should not be applied as its underlying principles are no longer sound.

6.2 Conclusions: CERES follow-on instrument

A radiative model of the current CERES telescope was developed using a new Monte-Carlo ray-trace environment being developed by a doctoral student in the Thermal Radiation Group. This model was used to study the feasibility of partitioning the current CERES telescope so that it serves multiple detectors. Also studied was the replacement of the spherical mirrors currently used in CERES with hyperbolic mirrors in order to achieve acceptable radiative throughput over a larger field of view.

The Optical Point Spread Function (OPSF) at a single detector placed on the CERES optical axis was determined using this new radiative model. This result was used to benchmark the new ray-trace environment and to validate the new code describing the CERES instrument by comparing it to the OPSF previously obtained by members of the TRG.

Results from this study indicate that the radiation throughput to two detectors placed in the CERES telescope is similar to that arriving at the single detector that lies on the optical axis in the current CERES instrument. However, if more than two detectors are placed into the telescope, the throughput drops off, resulting in an unacceptable OPSF at all but the central detector. It was also determined that hyperbolic mirrors do achieve acceptable radiative throughput over a larger field of view than do spherical mirrors, and their use is suggested if more than two detectors are to be placed in each telescope.
These results are presented in Chapter 5.0.

6.3 Potential future investigations of diffraction models

Useful future work could involve the development of an approach to scale ray-trace results to match the analytical curve for the statistical method, as the current method involves simply scaling the results "by eye" until the area under the ray-trace curve appears to match that of the analytical curve. The model based upon the modified Huygens-Fresnel principle (Model 2), and the cause of the oscillating intensity pattern it predicts, should be further investigated. Other case studies similar to the one presented in Section 4.3.6 could be conducted to determine the generality of the restrictions placed on the applicability of this model. Another unexplored aspect of the diffraction of radiant energy by an aperture involves the behavior of radiation as it approaches an aperture (prior to entry through the aperture), and the possibility of backwards diffraction. The geometric theory of diffraction described in Chapter 3.0 does model both forward and backward diffraction of energy as it approaches an aperture, and may be capable of properly modeling this behavior.

6.4 Potential future investigations of CERES follow-on instrument

Future studies could involve the placement of the hyperbolic mirrors into an appropriately modified CERES telescope, and the determination of the resulting Optical Point Spread Function. The new MCRT environment could be used to study the effect of slight modifications of the interior telescope surfaces on the throughput to the detectors. Another potential study could involve a different detector arrangement within the telescope. For example, instead of inserting extra detectors in a row, the detectors could be placed in some alternative arrangement, which provides an optimal throughput to all detectors.

REFERENCES

Anon., InterNetwork, Inc., 1993, EOS A Mission to Planet Earth, The National Aeronautics and Space Administration.

Ahrens, Donald C., **Meteorology Today**, West Publishing Company, St.Paul, MN, 1992.

Balanis, C.A., and Peters, L. Jr., *Analysis of aperture radiation from an axially slotted circular conducting cylinder using geometrical theory of diffraction*, **IEEE Transactions on antennas and propagation**, Vol. AP-17. No. 1, 1968, pp. 93-97.

Barkstrom, Bruce R., Personal communication (presentation entitled *Follow on CERES*), May, 1998.

Barkstrom, Bruce R., Martin Mlynczak, Kory Priestley, Edward Kist, David Kratz, Greg Stover, Bruce Wielicki, J. Robert Mahan, G. Louis Smith *Development of a Radiometric Test Model and Conceptual Design for PERSEPHONE, a Platform for Earth Radiation Studies emphasizing the Energetics of the atmosPHeric and OceaNic Environment*, Proposal submitted for the Instrument Incubator Project, Summer 1998.

Boivin, L. P., *Radiometric errors caused by diffraction from circular apertures: edge effects*, **Applied Optics**, Vol. 16, No. 2, 1976, pp. 377-383.

Bongiovi, Robert P. III, **A parametric study of the radiative and optical characteristics of a scanning radiometer for earth radiation budget applications using the Monte-Carlo method**, Master of Science Thesis, Department of Mechanical Engineering, Virginia Polytechnic Institute and State University, Blacksburg VA, 1993.

Born, Max, **Principles of Optics: Electromagnetic theory of propagation, interference and diffraction of light, Fourth Edition**, Pergamon Press, Oxford, 1970.

Bouwkamp, Christoffell, J., *Theoretical and numerical treatment of diffraction through a circular aperture*, **IEEE Transactions on antennas and propagation**, Vol. Ap-18, No. 2, 1970, pp. 152-176.

Boyce, Bruce M., *GUERAP II, a computer program for the analysis of the stray radiation rejection capabilities of optical systems*, SPIE, Vol. 107: Stray light problems in optical systems, 1977, pp. 72-79.

Braun, W. C., *The effects of diffraction on the field of view of an optical instrument*, **Applied Optics**, Vol. 9, No. 8, 1970, pp. 1862-1867.

Burroughs, William James, **Does the weather really matter? The social implications of climate change**, Cambridge University Press, Cambridge, United Kingdom, 1997.

Carman, S., *DRL 61, 55067.300.009B, Clouds and the Earth's Radiant Energy System (CERES), Optical and radiometric analyses, Revision B*, TRW Applied Technology Division, Space and Electronics Group, Redondo Beach, CA, 5 November 1993.

Chou, Tien S., *A Monte- Carlo approach to optical analysis*, **Optical Engineering**, Vol. 13, No. 4, 1974, pp. 299-302.

Coffey, Katherine L., K.J. Priestley, J.R. Mahan, and María Cristina Sánchez, *Diffraction models of radiation entering an aperture for use in a Monte-Carlo ray-trace environment,* SPIE 43rd Annual Meeting, San Diego, CA, July 19-24, 1998.

Deepak, Adarsh, and Richard R. Adams, *Photography and photographic-photometry of the solar aureole*, **Applied Optics**, Vol. 22, No. 11, 1983, pp. 1646-1654.

Gibbons, J. D. and Chakraborti, S., **Nonparametric Statistical Inference, Third Edition**, Mercel Dekker Incorporated, New York, NY, 1992.

Graves, Billy, Terrry T. Crow, Clayborne D. Taylor, *On the electromagnetic field penetration through apertures*, **IEEE Transactions on antennas and propagation**, Vol. EMC-18, No. 4, 1976, pp. 154-162.

Haeffelin, Martial P.A., J. Robert Mahan, Kory J. Priestley, *Predicted dynamic electrothermal performance of thermistor bolometer radiometers for Earth radiation budget applications*, **Applied Optics**, Vol. 36, No. 28, pp. 7129-7142, 1997.

Haeffelin, Martial P.A., **A Study of Earth Radiation Budget Radiometric Channel Performance and Data Interpretation Protocols**, Ph. D. Dissertation, Department of Mechanical Engineering, Virginia Polytechnic Institute and State University and *Laboratoire d'Optiques Dynamiques, Université de Lille I (France)*, 1996.

Haskell, Richard E., *A simple experiment on Fresnel diffraction*, **American Journal of Physics**, Vol. 38, No. 8, 1970, pp. 1039-1042.

Hecht, Eugene and Zajac, Alfred, **Optics**, Addison-Wesley Publishing Company, Inc., 1974.

Heinisch, R. P. and Chou, T. S., *Numerical experiments in modeling diffraction phenomena*, **Applied Optics**, Vol.10, No. 10, 1971, pp. 2248-2251.

Hubing, Todd H., *Survey of electromagnetic modeling techniques*, University of Missouri-Rolla Electromagnetic Compatibility Laboratory, Sept. 1991.

Intergovernmental Panel on Climate Change (IPPC), Technical report, 1997, www.gcrio.orc/ippc/techrepI.html, as accessed 06/1998.

Keller, Joseph B., *Geometrical Theory of Diffraction*, **Journal of the Optical Society of America**, Vol. 52, No. 2, 1962, pp. 116-130.

Keller, Joseph B., *Diffraction by an aperture*, **Journal of Applied Physics**, Vol. 28, No. 4, 1957, pp. 426-444.

Laufer, Gabriel, **Introduction to Optics and Lasers in Engineering**, Cambridge University Press, New York, NY, 1996.

Lenoble, Jacqueline, **Atmospheric Radiative Transfer**, A. Deepak Publishing, Hampton, VA, 1993.

Likeness, Barry K., *Stray light simulation with advanced Monte-Carlo techniques*, SPIE, Vol. 107, 1977, pp. 80-88.

Mahan, J. R., Langley, Lawrence W., *The Geo-synchronous Earth Radiation Budget Instrument: A Thermopile Linear-Array Thermal Radiation Detector*, A proposal submitted to NASA Langley Research Center, Hampton, VA, June 28, 1996.

Mahan, J. R., Stéphanie A. Weckmann, María Cristina Sánchez, Ira J. Sorensen, Katherine L. Coffey, Edward H. Kist, Jr., and Edward L. Nelson, *Optical and electrothermal design of a linear-array thermopile detector for geostationary earth radiation budget applications*, European Syposium on Remote Sensing (Europto Series), Consference on Sensors, Systems and Next-Generation Satellites, Barcelona, Spain, September 21-24, 1998.

Mayes, T. W. and Melton, B. F., *Fraunhofer diffraction of visible light by a narrow slit*, **American Journal of Physics**, Vol. 62, No. 5, 1994, pp. 397-403.

Meekins, Jeffrey L., **Optical analysis of the ERBE scanning thermistor bolometer radiometer using the Monte-Carlo method**, Master of Science Thesis, Department of Mechanical Engineering, Virginia Polytechnic Institute and State University, Blacksburg VA, 1990.

Morbey, Christopher and Hutchings, J. B., *Telescope baffle performance for Lyman Far Ultraviolet Spectrographic Explorer*, **Applied Optics**, Vol. 32, No. 19, 1993, pp. 3570-3584.

Nakajima, Teruyki, Masayuki Tanaka, and Toyotato Yamauchi, *Retrieval of the optical properties of aerosols from aureole and extinction data*, **Applied Optics**, Vol 22, No. 19, 1983, pp. 2951-2959.

Plank, Max, **The Theory of Heat Radiation**, Dover Publications, Inc., New York, NY, 1959.

Priestley, Kory J. **Use of First-Principle Numerical Models to Enhance the Understanding of the Operational Analysis of Space-Based Earth Radiation Budget Instruments**, Ph.D. Dissertation, Department of Mechanical Engineering, Virginia Polytechnic Institute and State University, Blacksburg VA, 1997.

Riedl, Max J., **Optical design fundamentals for infrared systems**, Vol. TT 20, SPIE Optical Engineering Press, Bellingham, Washington, 1997.

Sánchez, María Cristina, **Optical analysis of a linear-array thermal radiation detector for geostationary earth radiation budget applications**, Master of Science Thesis, Department of Mechanical Engineering, Virginia Polytechnic Institute and State University, Blacksburg, VA 1998.

Serway, Raymond A., **Principles of Physics**, Saunders College Publishing, 1994.

Sinnott, Roger W., *Astronomical computing*, Sky and Telescope, September, 1987, pp. 294-296.

Smith, Louis G., Robert B. Lee III, Bruce R. Barkstrom, Bruce A. Wielicki, Kory J. Priestley, Susan Thomas, Jack Paden, Robert S. Wilson, D. K. Pandy, and K. Lee Thornhill, *Overview of CERES Sensors and In-Flight Performance*, SPIE 43rd Annual Meeting, San Diego, CA, July 19-24, 1998.

Sorensen, Ira J., **Optimal design and characterization of a linear-array thermopile scanning radiometer for earth radiation budget applications**, Master of Science

Thesis, Department of Mechanical Engineering, Virginia Polytechnic Institute and State University, Blacksburg VA, 1998.

Tschunko, H.F.A., and P.J. Sheehan, *Aperture configuration and imaging performance*, **Applied Optics**, Vol. 10, No. 6, 1971, pp. 1432-1438.

Walker, Bruce H., **Optical engineering fundamentals**, SPIE Optical Engineering Press, 1998.

Walkup, Michael D., **A Monte-Carlo optical workbench for radiometric imaging system design**, Master of Science Thesis, Department of Mechanical Engineering, Virginia Polytechnic Institute and State University, Blacksburg VA, 1996.

Weckmann, Stéphanie A., **Dynamic electrothermal model of a sputtered thermopile thermal radiation detector for earth radiation budget applications**, Master of Science Thesis, Department of Mechanical Engineering, Virginia Polytechnic Institute and State University, Blacksburg, VA 1997.

Weckmann, Stéphanie, Ira Sorensen, J.-R. Mahan, E. L. Nelson, Lawrence W. Langley, Gary Halama, and Edward H. Kist, Jr., *Analysis and testing of a new thermopile linear-array thermal radiation detector for Earth radiation budget applications,* American Society for Photogammetry and Remote Sensing and Resource Technology Institute Annual Conference, Tampa, FL, April 2-4, 1998.

Weckmann, Stéphanie, María Cristina Sánchez, J. R. Mahan, Lawrence W. Langley, E. L. Nelson, and Katherine L. Coffey, *A thermopile linear array thermal radiation detector for monitoring the Earth radiation budget*, American Society for Photogammetry and Remote Sensing and Resource Technology Institute Annual Conference, Tampa, FL, April 2-4, 1998.

Wielicki, Bruce A., R. N. Green, *Cloud identification for ERBE radiative flux retrieval*, **Journal of Applied Meteorology**, Vol. 28, 1989, pp. 1133-1146.

Wielicki, Bruce A., Robert D. Cess, Michael D. King, David A. Randall, Edwin F. Harrison, *Mission to Planet Earth: Role of Clouds and Radiation in Climate*, **Bulletin of the American Meteorological Society**, Vol. 76, No. 11, 1995, pp. 2125-2153.

Wielicki, Bruce A., Bruce R. Barkstrom, Edwin F. Harrison, Robert B. Lee III., G. Louis Smith, John E. Cooper , *Clouds and the Earth's Radiant Energy System (CERES): An Earth Observing System Experiment*, **Bulletin of the American Meteorological Society**, Vol. 77, No. 5, 1996, pp. 853-868.

Wyatt, Clair L., **Radiometric system design**, Macmillan Publishing Company, New York, 1987.

This program, written in FORTRAN, demonstrates the application of the statistical approach to the modeling of diffraction. It predicts the spatial distribution of diffracted energy as it passes through a single infinite slit, and arrives at an observation screen some distance away. The following describes the variables used throughout the program. This particular version is for the ***splitting rays approach****.*

```
* NY is an array that divides the observation screen into strips. Each element in this array serves as a
* "bin" which keeps track of the number of bundles reaching that strip.

* LAMDA is the wavelength of the entering monochromatic radiation.

* W is the width of the rectangular slit.

* Z is the distance from the aperture to the observation screen.

* R is the change in vertical location that the entering energy bundle undergoes between its point of entry
* and its arrival to the observation screen.

* DIST is the total distance traveled by energy bundle from aperture before being intercepted by the
* observation screen.

* YO is the coordinate of the bottom edge of the rectangular aperture.

* Y is the coordinate of the entering energy bundle in the plane containing the aperture.

* YSCREEN is the coordinate of the energy bundle when it strikes the observation plane. Note that the
* YSCREEN coordinate is such that YSCREEN=0 occurs at the aperture center.

* YSCMIN, YSCMAX determine the minimum and maximum values of Y for which the number of
*  energy bundles striking at the observation screen will be recorded.

* H is the number of strips into which the observation screen will be divided.

* INCREM is the width of each of the strips on the observation screen.

* NUMRAYS is the number of energy bundles to be directed from the aperture to the observation screen.

* DEL1,DEL2 are the distances from the point of entry to the two aperture edges.

* RANMAR calls a random number from the subroutine rmarin(ij, kl).

* XVAL(ERFX) is the subroutine which determines the values of x when erf(x) is known, and returns this
* value to the main program.

* ERFX1,ERFX2 are the arguments sent to XVAL for the determination of x where erf(x) is known.

* SD1,SD2 are the standard deviations for the diffraction angles calculated for each of the two edges.

* K is the wavenumber, given by 2*PI/LAMDA.

* PHI1,PHI2 are the two diffraction angles due to each aperture side.

* YDIV is the variable used to determine the "bin" into which to store energy bundles incident to the
*  observation screen.
```

```
PROGRAM DIFFRACT1

C$  NOEXTENSIONS NOWARNINGS

*   Initialize arrays, Note that array NY is of size H, where H is the number of strips into which
*   observation screen is divided.

    DIMENSION NY(1000)

*   Initialize variables used in program

    DOUBLE PRECISION LAMDA, W,Z,Y,R1,YO,DEL1,DEL2,RANMAR,ARG2
   *PI,ERFX1,ERFX2,SD1,SD2,K,PHI1,PHI2,PHIDIFF1,YSCREEN1,ARG1,
   *YSCMIN,YSCMAX,INCREM,NY,DIST1,PHIDIFF2,R2,DIST2,YSCREEN2

    REAL XVAL

    INTEGER N,YDIV,H,NUMRAYS

    DATA LAMDA,W,Z,PI/100.0,60.0,60.25,3.141593/

    H=1000
    YO=-W/2
    YSCMAX=80.0
    YSCMIN=-80.0
    INCREM=(YSCMAX-YSCMIN)/H
    NUMRAYS=2000000
    K=(2*PI)/LAMDA

*   Open file that will store output from execution of code.
    OPEN(15,FILE='sr100',STATUS='OLD')

*   Initialize the values in the matrix containing the number of energy bundles arriving at screen, which is
*   divided into H strips.

    DO 5 I=1,H
    NY(I)=0
5   CONTINUE

*   Assign seeds for random number generator.
    I=1
    J=3
    CALL RMARIN(I,J)

*   Begin Monte-Carlo solution.  This loop causes NUMRAYS rays to be fired in randomly and uniformly
*   from aperture.

    DO 10 J=1,NUMRAYS

*   Calculate point of entry of the current energy bundle.

    Y=YO + RANMAR()*W

*   Calculate distance from point of entry of the current energy bundle and the two aperture edges.

    DEL1=(W/2)+ABS(Y)
```

```
      DEL2=(W/2)-ABS(Y)

*     Calculate the standard deviation for distribution of diffraction angles.

      SD1=ATAN(1.0/(2.0*DEL1*K))
      SD2=ATAN(1.0/(2.0*DEL2*K))

*     Calculate the angle of diffraction caused by each of the aperture edges.  The subprogram XVAL must
*     be called in order to determine the value of x, where erf(x) is known.

      ERFX1= 2.0*RANMAR()-1.0
      ARG1=XVAL(ERFX1)
      PHI1=ATAN(ARG1*SQRT(2.0)*SD1)

*     Calculate the angle of diffraction caused by the other aperture edge.

      ERFX2= 2.0*RANMAR()-1.0
      ARG2=XVAL(ERFX2)
      PHI2=ATAN(ARG2*SQRT(2.0)*SD2)

*     Calculate the angle of diffraction caused by each edge.

      PHIDIFF1=PHI1
      PHIDIFF2=PHI2

*     Calculate the change in vertical location of the entering energy bundle, R.

      R1=TAN(PHIDIFF1)*Z
      R2=TAN(PHIDIFF2)*Z

*     Calculate the total distance traveled by the energy bundle before reaching the screen, DIST.

      DIST1=SQRT(Z**2+ R1**2)
      DIST2=SQRT(Z**2+ R2**2)

*     Calculate the coordinate at which each energy bundle arrives at the observation screen.

      YSCREEN1=Y+R1
      YSCREEN2=Y+R2

*     Increment counter for correct strip on observation screen for ray1.

     IF (ABS(YSCREEN1).LE.YSCMAX) THEN
      IF (YSCREEN1.LT.0) THEN
         YDIV =INT(YSCREEN1/INCREM)-1
         YDIV=((H/2)+1)+YDIV
       ELSE IF (YSCREEN1.GE.0) THEN
         YDIV =INT(YSCREEN1/INCREM)+1
         YDIV=YDIV+(H/2)
       END IF
      NY(YDIV)=NY(YDIV)+1
      END IF
```

```
*   Increment counter for correct strip on observation screen for ray2.

    IF (ABS(YSCREEN2).LE.YSCMAX) THEN
      IF (YSCREEN2.LT.0) THEN
        YDIV =INT(YSCREEN2/INCREM)-1
        YDIV=((H/2)+1)+YDIV
      ELSE IF (YSCREEN2.GE.0) THEN
        YDIV =INT(YSCREEN2/INCREM)+1
        YDIV=YDIV+(H/2)
      END IF
    NY(YDIV)=NY(YDIV)+1
    END IF

10    CONTINUE
*   After all rays have been fired, store the results in an output file.
      DO 40 I=1,H
      WRITE(15,*)NY(I),(YSCMIN+INCREM*(I-1)),'  -',(YSCMIN+INCREM*(I))
40    CONTINUE

      END


*  Subroutine that determines x, when erf(x) is known

     FUNCTION XVAL(ERFX)

*  This subprogram is used to solve for x, knowing erf(x), which is sent from the main program.  A
*  truncated infinite series is used to approximate the error function, which can be solved for x
*  using the bisection method.

*   Initialize all variables

      INTEGER NUM,I,NEG
      DOUBLEPRECISION SD,A,B,TOL,P,PO,PI,CHK,ERFX,FP,FA,FB
      REAL XVAL
      DATA TOL/0.0001/, PI/3.141593/, NUM/1000/

      IF (ERFX.LT.0) THEN
       NEG=1
       ERFX=ABS(ERFX)
      ELSE IF (ERFX.GT.0) THEN
       NEG=2
      END IF

     IF (ERFX.LE.0.992869) THEN

*   Initialize endpoints (x=a, lower endpoint; x=b, upper endpoint)
      A=-1
      B=2.0

*   Initialize counter
      I=0

*   Begin loop to continue for a maximum of NUM iterations
      DO WHILE (I.LT.NUM)
       CHK= ABS((B-A)/2)
```

```
*   Determine midpoint
      P= A + ((B-A)/2)

*   Solve error function for current midpoint and endpoints using a truncated (15 terms) infinite series
*   approximating erf(x).

     FP=(2/SQRT(PI))*(P-(P**3)/(3*1)+(P**5)/(5*2)-(P**7)/(7*6)
    *+(P**9)/(9*24)-(P**11)/(11*120)+(P**13)/(13*720)-
    *(P**15)/(15*5040) +(P**17)/(17*40320)-(P**19)/(19*362880)
    *+(P**21)/(21*3628800)-(P**23)/(23*39916800))-ERFX

     FA=(2/SQRT(PI))*(A-(A**3)/(3*1)+(A**5)/(5*2)-(A**7)/(7*6)
    *+(A**9)/(9*24)-(A**11)/(11*120)+(A**13)/(13*720)-
    *(A**15)/(15*5040) + (A**17)/(17*40320) -(A**19)/(19*362880)
    *+(A**21)/(21*3628800)-(A**23)/(23*39916800))-ERFX

     FB=(2/SQRT(PI))*(B-(B**3)/(3*1)+(B**5)/(5*2)-(B**7)/(7*6)
    *+(B**9)/(9*24)-(B**11)/(11*120)+(B**13)/(13*720)-
    *(B**15)/(15*5040) + (B**17)/(17*40320) -(B**19)/(19*362880)
    *+(B**21)/(21*3628800)-(B**23)/(23*39916800))-ERFX

       IF (FP.EQ.0) THEN
        XVAL=P
        GO TO 10
       ELSE IF (CHK.LT.TOL) THEN
        XVAL=(A+B)/2
        GO TO 10
       ELSE IF ((FA*FP).LT.0) THEN
        B=P
       ELSE IF ((FB*FP).LT.0) THEN
        A=P
       END IF

    END DO

     ELSE
      XVAL=2
      END IF

10   IF (NEG.EQ.1) THEN
      XVAL=-XVAL
      ERFX=-ERFX
     END IF

     END

*  Subroutine that generates Random Numbers

      SUBROUTINE RMARIN(ij, kl)

C This is the initialization routine for the random number generator ranmar(). NOTE: The seed variables
C can have values between:
C    0 <= IJ <= 31328
C    0 <= KL <= 30081

C The random number sequences created by these two seeds are of sufficient length to complete an entire
```

```
C calculation with. For example, if sveral different groups are working on different parts of the same
C calculation, each group could be assigned its own IJ seed. This would leave each group with 30000
C choices for the second seed. That is to say, this random number generator can create 900 million different
C subsequences -- with each subsequence having a length of approximately 10^30.
C Use IJ = 1802 & KL = 9373 to test the random number generator. The subroutine ranmar should be used
C to generate 20000 random numbers. Then display the next six random numbers generated multiplied by
C 4096*4096. If the random number generator is working properly, the random numbers should be:
C        6533892.0  14220222.0  7275067.0
C        6172232.0  8354498.0   10633180.0

C   implicit real*8 (a-h, o-z)
    real*8 u(97), c, cd, cm, s, t
    integer ii, i, j, ij, jj, k, kl, l, m, i97, j97
    logical test
    common /raset1/ u, c, cd, cm, i97, j97, test
    test = .false.
c
    if( IJ .lt. 0  .or.  IJ .gt. 31328  .or.
   S    KL .lt. 0  .or.  KL .gt. 30081 ) then
      write (*, *) ' The first random number seed must have a'
      write (*, *) ' value between 0 and 31328.'
      write (*, *)
      write (*, *) ' The second seed must have a value between 0'
      write (*, *) ' and 30081.'
      write (*, *) 'Stopping...'
      stop
    endif
c
    i = mod(IJ/177, 177) + 2
    j = mod(IJ    , 177) + 2
    k = mod(KL/169, 178) + 1
    l = mod(kl,     169)
c
    do 2 ii = 1, 97
      s = 0.0
      t = 0.5
      do 3 jj = 1, 24
        m = mod(mod(i*j, 179)*k, 179)
        i = j
        j = k
        k = m
        l = mod(53*l+1, 169)
        if (mod(l*m, 64) .ge. 32) then
          s = s + t
        endif
        t = 0.5 * t
3     continue
      u(ii) = s
2     continue
c
    c = 362436.0 / 16777216.0
    cd = 7654321.0 / 16777216.0
    cm = 16777213.0 /16777216.0
c
    i97 = 97
    j97 = 33
```

```
c
    test = .true.
c
    return
    end
    real*8 function ranmar()
c
c This is the random number generator proposed by George Marsaglia
c in Florida State University Report: FSU-SCRI-87-50
c
c    implicit real*8 (a-h, o-z)
    real*8 u(97), uni, c, cd, cm
    integer i97, j97
    logical test
    common /raset1/ u, c, cd, cm, i97, j97, test
c
    if(.not.test) then
      write (*, *)
      write (*, *) 'ranmar error #1: must call the'
      write (*, *) 'initialization routine rmarin before'
      write (*, *) 'calling ranmar.'
      write (*, *) 'Stopping...'
      stop
    endif
c
    uni = u(i97) - u(j97)
    if( uni .lt. 0.0 ) uni = uni + 1.0
    u(i97) = uni
    i97 = i97 - 1
    if(i97 .eq. 0) i97 = 97
    j97 = j97 - 1
    if(j97 .eq. 0) j97 = 97
    c = c - cd
    if( c .lt. 0.0 ) c = c + cm
    uni = uni - c
    if( uni .lt. 0.0 ) uni = uni + 1.0
c
    ranmar = uni
c
    return
    end
```

This portion of a program, written in FORTRAN, demonstrates the application of the statistical approach to the modeling of diffraction. It predicts the spatial distribution of diffracted energy as it passes through a single infinite slit, and arrives at an observation screen some distance away. The subroutines called can be found with the first code (for the splitting rays approach) in Appendix A. This particular version is for the ***summing angles approach****.*

```
PROGRAM DIFFRACT2
C$  NOEXTENSIONS NOWARNINGS
*   Initialize variables used in program

*   Initialize arrays
    DIMENSION NY(1000)

*   Note that array NY is of size H, where H is the number of strips into which observation screen is
*   divided.

    DOUBLE PRECISION LAMDA, W,Z,Y,R1,YO,DEL1,DEL2,RANMAR,
   *PI,ERFX1,ERFX2,SD1,SD2,K,PHI1,PHI2,PHIDIFF,YSCREEN,ARG1,
   *YSCMIN,YSCMAX,INCREM,NY,DIST,R,ARG2
    REAL XVAL
    INTEGER N,YDIV,H,NUMRAYS

    DATA LAMDA,W,Z,PI/100.0,60.0,60.25,3.141593/
    H=1000
    YO=-W/2
    YSCMAX=80.0
    YSCMIN=-80.0
    INCREM=(YSCMAX-YSCMIN)/H
    NUMRAYS=2000000
    K=(2*PI)/LAMDA

*   Open file that will store output from execution of code.
    OPEN(15,FILE='sumr100',STATUS='OLD')

*   Initialize the values in the matrix containing the number of energy bundles arriving at screen, which is
*   divided into H strips.

    DO 5 I=1,H
    NY(I)=0
5   CONTINUE

*   Assign seeds for random number generator.
    I=1
    J=3
    CALL RMARIN(I,J)

*   Begin Monte-Carlo solution. This loop causes NUMRAYS rays to be fired in randomly and uniformly
*   from aperture.

    DO 10 J=1,NUMRAYS

*   Calculate point of entry of the current energy bundle.
     Y=YO + RANMAR()*W

*   Calculate distance from point of entry of the current energy bundle and the two aperture edges.
     DEL1=(W/2)+ABS(Y)
```

```
      DEL2=(W/2)-ABS(Y)

*     Calculate the standard deviation for distribution of diffraction angles.

      SD1=ATAN(1.0/(2.0*DEL1*K))
      SD2=ATAN(1.0/(2.0*DEL2*K))

*     Calculate the angle of diffraction caused by each of the aperture edges.  The subprogram XVAL must
*     be called in order to determine the value of x, where erf(x) is known.

      ERFX1= 2.0*RANMAR()-1.0
      ARG1=XVAL(ERFX1)
      PHI1=ATAN(ARG1*SQRT(2.0)*SD1)

*     Calculate the angle of diffraction caused by the other aperture edge.

      ERFX2= 2.0*RANMAR()-1.0
      ARG2=XVAL(ERFX2)
      PHI2=ATAN(ARG2*SQRT(2.0)*SD2)

*     Calculate the angle of diffraction due to the presence of both sides of the aperture by summing the two
*     angles.

      PHIDIFF=PHI1+PHI2

*     Calculate the change in vertical location of the entering energy bundle, R.

      R=TAN(PHIDIFF)*Z

*     Calculate the total distance traveled by the energy bundle before reaching the screen, DIST.

      DIST=SQRT(Z**2+ R**2)

*     Calculate the coordinate at which each energy bundle arrives at the observation screen.

      YSCREEN=Y+R

*     Increment counter for correct strip on observation screen.

     IF (ABS(YSCREEN).LE.YSCMAX) THEN
      IF (YSCREEN.LT.0) THEN
      YDIV =INT(YSCREEN/INCREM)-1
       YDIV=((H/2)+1)+YDIV
      ELSE IF (YSCREEN.GE.0) THEN
      YDIV =INT(YSCREEN/INCREM)+1
       YDIV=YDIV+(H/2)
      END IF
      NY(YDIV)=NY(YDIV)+1
      END IF

10    CONTINUE
*     After all rays have been fired, store the results in an output file.
       DO 40 I=1,H
       WRITE(15,*)NY(I),(YSCMIN+INCREM*(I-1)),'  -',(YSCMIN+INCREM*(I))
40     CONTINUE
     END
```

This portion of a program, written in FORTRAN, demonstrates the application of the statistical approach to the modeling of diffraction. It predicts the spatial distribution of diffracted energy as it passes through a single infinite slit, and arrives at an observation screen some distance away. The subroutines called can be found with the first code (for splitting rays approach) in Appendix A.. This particular version is for the ***closest edge effect*** *approach.*

```
PROGRAM DIFFRACT3
C$  NOEXTENSIONS NOWARNINGS


*   Initialize arrays, note that array NY is of size H, where H is the number of strips into which
*   observation screen is divided.
    DIMENSION NY(1000)

*   Initialize variables used in program

    DOUBLE PRECISION LAMDA, W,Z,Y,R1,YO,DEL1,DEL2,RANMAR,ARG2
   *PI,ERFX1,ERFX2,SD1,SD2,K,PHI1,PHI2,PHIDIFF1,YSCREEN1,ARG1,
   *YSCMIN,YSCMAX,INCREM,NY,DIST1,PHIDIFF2,R2,DIST2,YSCREEN2
    REAL XVAL
    INTEGER N,YDIV,H,NUMRAYS

    DATA LAMDA,W,Z,PI/100.0,60.0,60.25,3.141593/
    H=1000
    YO=-W/2
    YSCMAX=80.0
    YSCMIN=-80.0
    INCREM=(YSCMAX-YSCMIN)/H
    NUMRAYS=2000000
    K=(2*PI)/LAMDA

*   Open file that will store output from execution of code.
    OPEN(15,FILE='ns100',STATUS='OLD')

*   Initialize the values in the matrix containing the number of energy bundles arriving at screen, which is
*   divided into H strips.

    DO 5 I=1,H
    NY(I)=0
5   CONTINUE

*   Assign seeds for random number generator.
    I=1
    J=3
    CALL RMARIN(I,J)

*   Begin Monte-Carlo solution. This loop causes NUMRAYS rays to be fired in randomly and uniformly
*   from aperture.

    DO 10 J=1,NUMRAYS

*   Calculate point of entry of the current energy bundle.
     Y=YO + RANMAR()*W

*   Calculate distance from point of entry of the current energy bundle and the two aperture edges.
     DEL1=(W/2)+ABS(Y)
```

```
      DEL2=(W/2)-ABS(Y)

      IF (DEL1.LT.DEL2)THEN
      SD1=ATAN(1.0/(2.0*DEL1*K))
      ERFX1= 2.0*RANMAR()-1.0
      ARG1=XVAL(ERFX1)
      PHI1=ATAN(ARG1*SQRT(2.0)*SD1)
      PHIDIFF1=PHI1
      R1=TAN(PHIDIFF1)*Z
      DIST1=SQRT(Z**2+ R1**2)
      YSCREEN1=Y+R1
     IF (ABS(YSCREEN1).LE.YSCMAX) THEN
      IF (YSCREEN1.LT.0) THEN
      YDIV =INT(YSCREEN1/INCREM)-1
       YDIV=((H/2)+1)+YDIV
      ELSE IF (YSCREEN1.GE.0) THEN
      YDIV =INT(YSCREEN1/INCREM)+1
       YDIV=YDIV+(H/2)
      END IF
      NY(YDIV)=NY(YDIV)+1
      END IF


      ELSE
     SD2=ATAN(1.0/(2.0*DEL2*K))
      ERFX2= 2.0*RANMAR()-1.0
      ARG2=XVAL(ERFX2)
      PHI2=ATAN(ARG2*SQRT(2.0)*SD2)
       PHIDIFF2=PHI2
      R2=TAN(PHIDIFF2)*Z
      DIST2=SQRT(Z**2+ R2**2)
      YSCREEN2=Y+R2

     IF (ABS(YSCREEN2).LE.YSCMAX) THEN
      IF (YSCREEN2.LT.0) THEN
      YDIV =INT(YSCREEN2/INCREM)-1
       YDIV=((H/2)+1)+YDIV
      ELSE IF (YSCREEN2.GE.0) THEN
      YDIV =INT(YSCREEN2/INCREM)+1
       YDIV=YDIV+(H/2)
      END IF
      NY(YDIV)=NY(YDIV)+1
      END IF
      END IF

10    CONTINUE

*    After all rays have been fired, store the results in an output file.

     DO 40 I=1,H
     WRITE(15,*)NY(I),(YSCMIN+INCREM*(I-1)),'  -',(YSCMIN+INCREM*(I))
40    CONTINUE
     END
```

This portion of a program, written in FORTRAN, demonstrates the application of the statistical approach to the modeling of diffraction. It predicts the spatial distribution of diffracted energy as it passes through a single infinite slit, and arrives at an observation screen some distance away. The subroutines called can be found with the first code (for splitting rays approach) in Appendix A. This particular version is for the ***furthest edge effect*** *approach.*

PROGRAM DIFFRACT4

```
C$   NOEXTENSIONS NOWARNINGS


*    Initialize arrays, note that array NY is of size H, where H is the number of strips into which
*    observation screen is divided.
     DIMENSION NY(1000)

*    Initialize variables used in program

     DOUBLE PRECISION LAMDA, W,Z,Y,R1,YO,DEL1,DEL2,RANMAR,
    *PI,ERFX1,ERFX2,SD1,SD2,K,PHI1,PHI2,PHIDIFF1,YSCREEN1,ARG1,ARG2
    *YSCMIN,YSCMAX,INCREM,NY,DIST1,PHIDIFF2,R2,DIST2,YSCREEN2
     REAL XVAL
     INTEGER N,YDIV,H,NUMRAYS

     DATA LAMDA,W,Z,PI/100.0,60.0,60.25,3.141593/
     H=1000
     YO=-W/2
     YSCMAX=80.0
     YSCMIN=-80.0
     INCREM=(YSCMAX-YSCMIN)/H
     NUMRAYS=2000000
     K=(2*PI)/LAMDA

*    Open file that will store output from execution of code.
     OPEN(15,FILE='fs100',STATUS='OLD')

*    Initialize the values in the matrix containing the number of energy bundles arriving at screen, which is
*    divided into H strips.

     DO 5 I=1,H
     NY(I)=0
5    CONTINUE

*    Assign seeds for random number generator.
     I=1
     J=3
     CALL RMARIN(I,J)

*    Begin Monte-Carlo solution. This loop causes NUMRAYS rays to be fired in randomly and uniformly
*    from aperture.

     DO 10 J=1,NUMRAYS

*    Calculate point of entry of the current energy bundle.
      Y=YO + RANMAR()*W

*    Calculate distance from point of entry of the current energy bundle and the two aperture edges.
      DEL1=(W/2)+ABS(Y)
```

```
       DEL2=(W/2)-ABS(Y)

       IF (DEL1.GT.DEL2)THEN
       SD1=ATAN(1.0/(2.0*DEL1*K))
       ERFX1= 2.0*RANMAR()-1.0
       ARG1=XVAL(ERFX1)
       PHI1=ATAN(ARG1*SQRT(2.0)*SD1)
       PHIDIFF1=PHI1
       R1=TAN(PHIDIFF1)*Z
       DIST1=SQRT(Z**2+ R1**2)
       YSCREEN1=Y+R1
      IF (ABS(YSCREEN1).LE.YSCMAX) THEN
       IF (YSCREEN1.LT.0) THEN
       YDIV =INT(YSCREEN1/INCREM)-1
        YDIV=((H/2)+1)+YDIV
       ELSE IF (YSCREEN1.GE.0) THEN
       YDIV =INT(YSCREEN1/INCREM)+1
        YDIV=YDIV+(H/2)
       END IF
       NY(YDIV)=NY(YDIV)+1
       END IF


       ELSE
      SD2=ATAN(1.0/(2.0*DEL2*K))
       ERFX2= 2.0*RANMAR()-1.0
       ARG2=XVAL(ERFX2)
       PHI2=ATAN(ARG2*SQRT(2.0)*SD2)
        PHIDIFF2=PHI2
       R2=TAN(PHIDIFF2)*Z
       DIST2=SQRT(Z**2+ R2**2)
       YSCREEN2=Y+R2

      IF (ABS(YSCREEN2).LE.YSCMAX) THEN
       IF (YSCREEN2.LT.0) THEN
       YDIV =INT(YSCREEN2/INCREM)-1
        YDIV=((H/2)+1)+YDIV
       ELSE IF (YSCREEN2.GE.0) THEN
       YDIV =INT(YSCREEN2/INCREM)+1
        YDIV=YDIV+(H/2)
       END IF
       NY(YDIV)=NY(YDIV)+1
       END IF
       END IF

10     CONTINUE

*    After all rays have been fired, store the results in an output file.

      DO 40 I=1,H
      WRITE(15,*)NY(I),(YSCMIN+INCREM*(I-1)),'  -',(YSCMIN+INCREM*(I))
40     CONTINUE
      END
```

This FORTRAN program is used to model diffraction through an infinite slit and is based on modified Huygen-Fresnel principle. The phase of an energy bundle upon its arrival to the observation screen is proportional to its optical length, and is summed with the phase of the others arriving at the same "bin" of the observation screen. The final sum of these phases at a is squared to provide the normalized intensity at that bin. Plotting this intensity of all bins yields a diffraction pattern. The subroutine rmarin is not provided here, as it can be found in Appendix A. The following defines the variables used in this program.

- NY is an array that divides the observation screen into strips. Each element in this array serves as a "bin" which keeps track of the number of bundles reaching that strip. This array is never actually used in the determination of the intensity pattern, but serves to verify that all of the bins are receiving the same number of energy bundles.
- LAMDA is the wavelength of the entering monochromatic radiation.
- W is the width of the rectangular slit.
- Z is the distance from the aperture to the observation screen.
- R is the change in vertical location of the entering energy bundle.
- DIST is the net distance traveled by energy bundle from aperture before being intercepted by observation screen.
- YO is the coordinate of the left hand bottom corner of the rectangular aperture.
- Y is the coordinate of the entering energy bundle in the plane containing the aperture.
- YSCREEN is the coordinate of the energy bundle when it strikes the observation screen. Note that the YSCREEN coordinate is such that YSCREEN=0 occurs at the aperture center.
- YSCMIN, YSCMAX determine the minimum and maximum values of Y for which the "number of energy bundles striking" at the observation screen will be recorded.
- H is the number of strips into which the observation screen will be divided.
- INCREM is the width of each of the strips on the observation screen.
- RANMAR calls a random number from the subroutine rmarin(ij, kl).
- K is the wavenumber, given by 2*PI/LAMDA.
- YDIV is the variable used to determine the "bin" into which to store energy bundles incident to the observation screen.

```
      PROGRAM SLITMONTECARLO
      dimension ny(10000), beta(10000)

      double precision lamda, w, z, y, r, yo, ranmar, pi, phidiff, yscreen, beta, k, yscmax, increm, dist,
     *    phimin, phimax, delphi,betaold,yscmin,obf
      integer n,ydiv,h,numrays,q,I,j
      open(01,file='out.dat',status='old')

      data lamda,w,z,pi/0.00000058, 0.0003,16.0,2.0,3.14159/
      yo=-w/2.0d0

*     Note that h must be evenly divisible by 2
      h=10000

*     Limit range of interest; specifying min/max y of interest.
      yscmax=0.009d0
      yscmin=-yscmax

      numrays=100000
      k=2.0d0*pi/lamda
```

```
*     Initialize the values in the matrix containing the number of energy bundles arriving at screen in a certain strip.
      do 3 j=1,h
       ny(j)=0.0d0
       beta(j)=0.0d0
3     continue

*     Initialize random number generator.
      i=1
      j=3
      increm=(yscmax-yscmin)/h
      call rmarin(i,j)


      do 5 q=1,numrays
*     Calculate the random point of entry of current energy bundle.  Note that the following restricts the direction of
*     emission so that all energy bundles will arrive at the observation screen, but maintains a diffuse emission where all
*     diffraction angles within the limited range will be equally probable.

       y=yo+ranmar()*w
       phimax=datan((yscmax)/z)
       phidiff=-phimax+2*phimax*ranmar()
       r=dtan(phidiff)*z
       yscreen=y+r
       dist=dsqrt(z**2+r**2)

*     Increment the number falling into a bin, keeping with the numbering scheme.
      if(abs(yscreen).le.yscmax)then
       if(yscreen.lt.0.0d0)then
       ydiv=int(abs(yscreen/increm))+1
       ydiv=(h/2)-ydiv+1
       else if (yscreen.ge.0.0d0) then
       ydiv=int(yscreen/increm)+1
       ydiv=ydiv+(h/2)
      end if
      ny(ydiv)=ny(ydiv)+1
*     Increment the phase of the appropriate bin.
      betaold=beta(ydiv)

*     Define the obliquity factor.
      obf=0.5d0*(1.0d0+dcos(phidiff))

*     Note that here dcos(2d0*dist*pi/lamda)) is used instead of dsin (2d0*dist*pi/lamda)), as defined by equation 4.33.
*     Either provide similar results, whereby the peaks fall within the envelope of the analytical solution, however use of
*     cos results in a pattern with the central oscillation at a peak, where use of sin results in the central oscillation at a
*     valley.
      beta(ydiv)=(obf*dcos(2d0*dist*pi/lamda))/(2d0*dist*pi/lamda)
      beta(ydiv)=beta(ydiv)+betaold
      end if
5     continue

      do 4 j=1,h
      write(01,*)sngl(atan((yscmin+increm*j)/z)),sngl(abs(beta(j)**2))
4     continue
      end
```

```
/*The following code was written in C programming language. It serves to define the geometry for the radiative model of the current CERES telescope and can be modified to model potential next-generation instruments. It calls C++ library functions written by TRG doctoral student, Félix Nevárez. This code generates output which can be used to determine the Optical Point Spread Function of the CERES instrument. Each surface within the telescope is modeled, and is referenced by a combination of letters and numbers. This labeling corresponds to the labeled Figure 5.1 (a) of the CERES telescope found in this thesis. Note that all dimensions are in inches, scaled by a factor of ten (10).*/

#include "raytracer.h"
#include "math.h"
#define PI 3.14159265359

main()
{
/*s is the scaling factor to scale all telescope dimensions*/
double s=10;
/*sh is the shift added by the insertion of shims to achieve best focus*/
double sh=.0110 ;
/*apw is the width of a precision aperture*/
double apw=0.0296;
/*d is the distance between precision apertures*/
double d=0.01;
/*theta is direction 1 of incoming rays*/
double theta;
/*phi is direction 2 of incoming rays*/
double phi;

/* Begin defining the CERES telescope geometry*/

/*CY1(Baffle)*/
makeACylinder(0.561*s);
setProperties(0.9,0.1);
setClipPlane (0.0,0.0,(0.0+o),0.0,0.0,1.0);
setClipPlane(0.0,0.0,(1.771+o)*s,0.0,0.0,-1.0);
noOutput();
nextOBJ();

/*R1(Baffle)*/
makeARing(0.0,0.0,(0.0+o)*s,0.0,0.0,1.0,0.4665*s,0.5610*s);
setProperties(0.99,0.1);
noOutput();
nextOBJ();

/*R2(Baffle)*/
makeARing(0.0,0.0,(0.39+o)*s ,0.0,0.0,1.0,0.4570*s,0.5610*s);
setProperties(0.99,0.1);
noOutput();
nextOBJ();

/*R3(Baffle)*/
makeARing(0.0,0.0,(0.770+o)*s,0.0,0.0,1.0,0.4475*s,0.5610*s);
setProperties(0.99,0.1);
noOutput();
nextOBJ();

/*R4(Baffle)*/
```

```
makeARing(0.0,0.0,(1.149+o)*s ,0.0,0.0,1.0,0.4385*s,0.5610*s);
setProperties(0.99,0.1);
noOutput();
nextOBJ();

/*R5(Baffle)*/
makeARing(0.0,0.0,(1.529+o)*s ,0.0,0.0,1.0,0.4290*s,0.5610*s);
setProperties(0.99,0.1);
noOutput();
nextOBJ();

/*C1(Baffle)*/
makeACone(0.3239*s,0.561*s);
setProperties(0.99,0.10);
setOrigin(0.0,0.0,(2.0949+o)*s);
setClipPlane(0.0,0.0,(1.771+o)*s,0.0,0.0,1.0);
setClipPlane(0.0,0.0,(1.8220+o)*s,0.0,0.0,-1.0);
noOutput();
nextOBJ();

/*CY2(Baffle)*/
makeACylinder(0.472*s);
setProperties(0.99,0.1);
setClipPlane(0.0,0.0,(1.8220+o)*s,0.0,0.0,1.0);
setClipPlane(0.0,0.0,(1.8540+o)*s,0.0,0.0,-1.0);
noOutput();
nextOBJ();

/*R6(Baffle)*/
makeARing(0.0,0.0,(1.854+o)*s,0.0,0.0,1.0,0.3995*s,0.472*s);
setProperties(0.99,0.1);
noOutput();
nextOBJ();

/*C2(CapReflector)*/
makeACone(0.952*s,0.424*s);
setProperties(0.99,0.1);
setOrigin(0.0,0.0,(0.9567+o)*s);
setClipPlane(0.0,0.0,(1.854+o)*s,0.0,0.0,1.0);
setClipPlane(0.0,0.0,(1.909+o)*s,0.0,0.0,-1.0);
noOutput();
nextOBJ();

/*C3(CapReflector)*/
makeACone(0.1904*s,0.424*s);
setProperties(0.001,0.9);
setOrigin(0.0,0.0,(2.0994+o)*s);
setClipPlane(0.0,0.0,(1.909+o)*s,0.0,0.0,1.0);
setClipPlane(0.0,0.0,(1.920+o)*s,0.0,0.0,-1.0);
noOutput();
nextOBJ();

/*C4(CapReflector)*/
makeACone(0.952*s,0.424*s);
setProperties(0.99,0.1);
setOrigin(0.0,0.0,(1.0227+o)*s);
```

```
setClipPlane(0.0,0.0,(1.92+o)*s,0.0,0.0,1.0);
setClipPlane(0.0,0.0,(1.975+o)*s,0.0,0.0,-1.0);
noOutput();
nextOBJ();

/*C5(CapReflector)*/
makeACone(0.1904*s,0.424*s);
setProperties(0.001,0.9);
setOrigin(0.0,0.0,(2.1654+o)*s);
setClipPlane(0.0,0.0,(1.975+o)*s,0.0,0.0,1.0);
setClipPlane(0.0,0.0,(1.986+o)*s,0.0,0.0,-1.0);
noOutput();
nextOBJ();

/*C6(CapReflector)*/
makeACone(0.952*s,0.424*s);
setProperties(0.99,0.1);
setOrigin(0.0,0.0,(1.0887+o)*s);
setClipPlane(0.0,0.0,(1.986+o)*s,0.0,0.0,1.0);
setClipPlane(0.0,0.0,(2.041+o)*s,0.0,0.0,-1.0);
noOutput();
nextOBJ();

/*C7(CapReflector)*/
makeACone(0.1904*s,0.424*s);
setProperties(0.001,0.9);
setOrigin(0.0,0.0,(2.2314+o)*s);
setClipPlane(0.0,0.0,(2.041+o)*s,0.0,0.0,-1.0);
setClipPlane(0.0,0.0,(2.052+o)*s,0.0,0.0,1.0);
noOutput();
nextOBJ();

/*C8(CapReflector)*/
makeACone(0.952*s,0.424*s);
setProperties(0.99,0.1);
setOrigin(0.0,0.0,(1.1547+o)*s);
setClipPlane(0.0,0.0,(2.052+o)*s,0.0,0.0,1.0);
setClipPlane(0.0,0.0,(2.107+o)*s,0.0,0.0,-1.0);
noOutput();
nextOBJ();

/*C9(CapReflector)*/
makeACone(0.1904*s,0.424*s);
setProperties(0.001,0.9);
setOrigin(0.0,0.0,(2.2974+o)*s);
setClipPlane(0.0,0.0,(2.107+o)*s,0.0,0.0,1.0);
setClipPlane(0.0,0.0,(2.118+o)*s,0.0,0.0,-1.0);
noOutput();
nextOBJ();

/*C10(CapReflector)*/
makeACone(0.952*s,0.424*s);
setProperties(0.99,0.1);
setOrigin(0.0,0.0,(1.2207+o)*s);
setClipPlane(0.0,0.0,(2.118+o)*s,0.0,0.0,1.0);
setClipPlane(0.0,0.0,(2.173+o)*s,0.0,0.0,-1.0);
```

```
noOutput();
nextOBJ();

/*C11(CapReflector)*/
makeACone(0.1904*s,0.424*s);
setProperties(0.001,0.9);
setOrigin(0.0,0.0,(2.363+o)*s);
setClipPlane(0.0,0.0,(2.173+o)*s,0.0,0.0,1.0);
setClipPlane(0.0,0.0,(2.184+o)*s,0.0,0.0,-1.0);
noOutput();
nextOBJ();

/*C12(CapReflector)*/
makeACone(0.924*s,0.411*s);
setProperties(0.99,0.1);
setOrigin(0.0,0.0,(1.287+o)*s);
setClipPlane(0.0,0.0,(2.184+o)*s,0.0,0.0,1.0);
setClipPlane(0.0,0.0,(2.211+o)*s,0.0,0.0,-1.0);
noOutput();
nextOBJ();

/*R7(CapReflector)*/
makeARing(0.0,0.0,(2.211+o)*s,0.0,0.0,1.0,0.411*s,0.4745*s);
setProperties(0.99,0.1);
noOutput();
nextOBJ();

/*CY3(CapReflector)*/
makeACylinder(0.4745*s);
setProperties(0.99,0.1);
setClipPlane(0.0,0.0,(2.211+o)*s,0.0,0.0,1.0);
setClipPlane(0.0,0.0,(2.221+o)*s,0.0,0.0,-1.0);
noOutput();
nextOBJ();

/*R8(CapReflector)*/
makeARing(0.0,0.0,(2.221+o)*s,0.0,0.0,1.0,0.4745*s,0.522*s);
setProperties(0.01,0.9);
noOutput();
nextOBJ();

/*CY4(CapReflector)*/
makeACylinder(0.522*s);
setProperties(0.01,0.9);
setClipPlane (0.0,0.0,(2.221+o)*s,0.0,0.0,1.0);
setClipPlane(0.0,0.0,(2.263+o)*s,0.0,0.0,-1.0);
noOutput();
nextOBJ();

/*R9(CapReflector)*/
makeARing(0.0,0.0,(2.263+o)*s ,0.0,0.0,1.0,0.4725*s,0.5220*s);
setProperties(0.01,0.9);
noOutput();
nextOBJ();

/*CY5(TelescopeHousing)*/
```

```
makeACylinder(0.4725*s);
setProperties(0.99,0.1);
setClipPlane (0.0,0.0,(2.263+o)*s,0.0,0.0,1.0);
setClipPlane(0.0,0.0,(2.386+o)*s,0.0,0.0,-1.0);
noOutput();
nextOBJ();

/*D1(Spider)*/
makeADisk(0.0,0.0,(2.263+o)*s,0.0,0.0,1.0,0.185*s);
setProperties(0.99,0.1);
noOutput();
nextOBJ();

/*leg1(Spider)*/
makeAPlane(0.0,0.0,(2.263+0.113+o)*s,0.0,0.0,1.0);
setProperties(0.99,0.1);
setClipPlane(0.03*s,-0.4725*s,(2.263+0.113+o)*s,0.0,1.0,0.0);
setClipPlane(0.03*s,-0.4725*s,(2.263+0.113+o)*s,-1.0,0.0,0.0);
setClipPlane(-0.03*s,0.0,(2.263+0.113+o)*s,1.0,0.0,0.0);
setClipPlane(0*s,-0.185*s,(2.263+0.113+o)*s,0.0,-1.0,0.0);
noOutput();
nextOBJ();

/*leg2(Spider)*/
makeAPlane(0.0,0.0,(2.263+0.113+o)*s,0.0,0.0,1.0);
setProperties(0.99,0.1);
setClipPlane(0.160*s,0.0925*s,(2.263+0.113+o)*s,0.866,0.5,0.0);
setClipPlane(0.459*s,0.23045*s,(2.263+0.113+o)*s,-0.5,0.866,0.0);
setClipPlane(0.459*s,0.23045*s,(2.263+0.113+o)*s,-0.866,-0.5,0.0);
setClipPlane(0.429*s,0.28225*s,(2.263+0.113+o)*s,0.5,-0.866,0.0);
noOutput();
nextOBJ();

/*leg3(Spider)*/
makeAPlane(0.0,0.0,(2.263+0.113+o)*s,0.0,0.0,1.0);
setProperties(0.99,0.1);
setClipPlane(-0.160*s,0.0925*s,(2.263+0.113+o)*s,-0.866,0.5,0.0);
setClipPlane(-0.459*s,0.23045*s,(2.263+0.113+o)*s,0.5,0.866,0.0);
setClipPlane(-0.459*s,0.23045*s,(2.263+0.113+o)*s,0.866,-0.5,0.0);
setClipPlane(-0.429*s,0.28225*s,(2.263+o+0.113)*s,-0.5,-0.866,0.0);
noOutput();
nextOBJ();

/*side1toleg1(Spider)*/
makeAPlane(0.03*s,0.0,(2.263+0.113+o)*s,-0.9659,0.0,0.2588);
setProperties(0.001,0.9);
setClipPlane(0.03*s,-0.4725*s,(2.263+0.113+o)*s,0.0,1.0,0.0);
setClipPlane(0.0,0.0,(2.263+0.113+o)*s,0.0,0.0,-1.0);
setClipPlane(0.0,0.0,(2.263+o)*s,0.0,0.0,1.0);
setClipPlane(0*s,-0.185*s,(2.263+0.113+o)*s,0.0,-1.0,0.0);
noOutput();
nextOBJ();

/*side2toleg1(Spider)*/
makeAPlane(-0.03*s,0.0,(2.263+0.113+o)*s,-0.9659,0.0,-0.2588);
setProperties(0.001,0.9);
```

```
setClipPlane(0.03*s,-0.4725*s,(2.263+0.113+o)*s,0.0,1.0,0.0);
setClipPlane(0.03*s,0.0,(2.263+0.113+o)*s,0.0,0.0,-1.0);
setClipPlane(0.0,0.0,(2.263+o)*s,0.0,0.0,1.0);
setClipPlane(0*s,-0.185*s,(2.263+0.113+o)*s,0.0,-1.0,0.0);
noOutput();
nextOBJ();


/*side1toleg2(Spider)*/
makeAPlane(0.429*s,0.28225*s,(2.263+0.113+o)*s,0.48295,-0.866,0.2588);
setProperties(0.001,0.9);
setClipPlane(0.160*s,0.0925*s,(2.263+0.113+o)*s,0.866,0.5,0.0);
setClipPlane(0.0,0.0,(2.263+o)*s,0.0,0.0,1.0);
setClipPlane(0.4092*s,0.23625*s,(2.263+o+0.113)*s,-0.866,-0.5,0.0);
setClipPlane(0.0,0.0,(2.263+o+0.113)*s,0.0,0.0,-1.0);
noOutput();
nextOBJ();

/*side2toleg2(Spider)*/
makeAPlane(0.459*s,0.23045*s,(2.263+0.113+o)*s,-0.48295,0.866,0.2588);
setProperties(0.001,0.9);
setClipPlane(0.160*s,0.0925*s,(2.263+0.113+o)*s,0.866,0.5,0.0);
setClipPlane(0.0,0.0,(2.263+o)*s,0.0,0.0,1.0);
setClipPlane(0.4092*s,0.23625*s,(2.263+0.113+o)*s,-0.866,-0.5,0.0);
setClipPlane(0.0,0.0,(2.263+0.113+o)*s,0.0,0.0,-1.0);
noOutput();
nextOBJ();


/*side1toleg3(Spider)*/
makeAPlane(-0.459*s,0.23045*s,(2.263+0.113+o)*s,0.48295,0.866,0.2588);
setProperties(0.001,0.9);
setClipPlane(-0.160*s,0.0925*s,(2.263+0.113+o)*s,-0.866,0.5,0.0);
setClipPlane(-0.4092*s,0.23625*s,(2.263+o+0.113)*s,0.866,-0.5,0.0);
setClipPlane(0.0,0.0,(2.263+o)*s,0.0,0.0,1.0);
setClipPlane(0.0,0.0,(2.263+o+0.113)*s,0.0,0.0,-1.0);
noOutput();
nextOBJ();

/*side2toleg3(Spider)*/
makeAPlane(-0.429*s,0.28225*s,(2.263+0.113+o)*s,-0.48295,-0.866,0.2588);
setProperties(0.001,0.9);
setClipPlane(-0.160*s,0.0925*s,(2.263+0.113+o)*s,-0.866,0.5,0.0);
setClipPlane(-0.4092*s,0.23625*s,(2.263+0.113+o)*s,0.866,-0.5,0.0);
setClipPlane(0.0,0.0,(2.263+o)*s,0.0,0.0,1.0);
setClipPlane(0.0,0.0,(2.263+o+0.113)*s,0.0,0.0,-1.0);
noOutput();
nextOBJ();

/*CY6(Spider)*/
makeACylinder(0.185*s);
setProperties(0.99,0.1);
setClipPlane (0.0,0.0,(2.263+o)*s,0.0,0.0,1.0);
setClipPlane(0.0,0.0,(2.506+o)*s,0.0,0.0,-1.0);
noOutput();
nextOBJ();
```

```
/*CY7(Spider)*/
makeACylinder(0.16*s);
setProperties(0.99,0.1);
setClipPlane (0.0,0.0,(2.448+o)*s,0.0,0.0,1.0);
setClipPlane(0.0,0.0,(2.4762+o)*s,0.0,0.0,-1.0);
noOutput();
nextOBJ();

/*C13(Spider)*/
makeACone(0.2205*s,0.185*s);
setProperties(0.99,0.1);
setOrigin(0.0,0.0,(2.2855+o)*s);
setClipPlane(0.0,0.0,(2.4762+o)*s,0.0,0.0,1.0);
setClipPlane(0.0,0.0,(2.506+o)*s,0.0,0.0,-1.0);
noOutput();
nextOBJ();

/*M2(SecondaryMirror)*/
makeASphere(1.318*s);
setProperties(0.001,1.0);
setOrigin(0.0,0.0,(1.14+o)*s);
setClipPlane(0.0,0.0,(2.448+o)*s,0.0,0.0,1.0);
noOutput();
nextOBJ();

/*C14(TelescopeHousing)*/
makeACone(0.2483*s,0.4725*s);
setProperties(0.99,0.1);
setOrigin(0.0,0.0,(2.6343+o)*s);
setClipPlane(0.0,0.0,(2.386+o)*s,0.0,0.0,1.0);
setClipPlane(0.0,0.0,(2.448+o)*s,0.0,0.0,-1.0);
noOutput();
nextOBJ();

/*R10(TelescopeHousing)*/
makeARing(0.0,0.0,(2.448+o)*s ,0.0,0.0,1.0,0.3545*s,0.4295*s);
setProperties(0.99,0.1);
noOutput();
nextOBJ();

/*CY8(TelescopeHousing)*/
makeACylinder(0.4295*s);
setProperties(0.99,0.1);
setClipPlane (0.0,0.0,(2.448+o)*s,0.0,0.0,1.0);
setClipPlane(0.0,0.0,(2.498+o)*s,0.0,0.0,-1.0);
noOutput();
nextOBJ();

/*R11(TelescopeHousing)*/
makeARing(0.0,0.0,(2.498+o)*s ,0.0,0.0,1.0,0.365*s,0.4295*s);
setProperties(0.99,0.1);
noOutput();
nextOBJ();

/*C15(TelescopeHousing)*/
```

```
makeACone(0.2807*s,0.486*s);
setProperties(0.99,0.1);
setOrigin(0.0,0.0,(2.2873+o)*s);
setClipPlane(0.0,0.0,(2.498+o)*s,0.0,0.0,1.0);
setClipPlane(0.0,0.0,(2.568+o)*s,0.0,0.0,-1.0);
noOutput();
nextOBJ();

/*C16(TelescopeHousing)*/
makeACone(0.2807*s,0.486*s);
setProperties(0.99,0.1);
setOrigin(0.0,0.0,(2.8487+o)*s);
setClipPlane(0.0,0.0,(2.568+o)*s,0.0,0.0,1.0);
setClipPlane(0.0,0.0,(2.638+o)*s,0.0,0.0,-1.0);
noOutput();
nextOBJ();

/*C17(TelescopeHousing)*/
makeACone(0.2807*s,0.486*s);
setProperties(0.99,0.1);
setOrigin(0.0,0.0,(2.4273+o)*s);
setClipPlane(0.0,0.0,(2.638+o)*s,0.0,0.0,1.0);
setClipPlane(0.0,0.0,(2.708+o)*s,0.0,0.0,-1.0);
noOutput();
nextOBJ();

/*C18(TelescopeHousing)*/
makeACone(0.2807*s,0.486*s);
setProperties(0.99,0.1);
setOrigin(0.0,0.0,(2.9887+o)*s);
setClipPlane(0.0,0.0,(2.708+o)*s,0.0,0.0,1.0);
setClipPlane(0.0,0.0,(2.778+o)*s,0.0,0.0,-1.0);
noOutput();
nextOBJ();

/*CY9(TelescopeHousing)*/
makeACylinder(0.365*s);
setProperties(0.99,0.1);
setClipPlane (0.0,0.0,(2.778+o)*s,0.0,0.0,1.0);
setClipPlane(0.0,0.0,(2.831+o+sh)*s,0.0,0.0,-1.0);
noOutput();
nextOBJ();

/*M1(PrimaryMirror)*/
makeASphere(1.446*s);
setProperties(0.001,1.0);
setOrigin(0.0,0.0,(1.432+o+sh)*s);
setClipPlane(0.0,0.0,(2.831+o+sh)*s,0.0,0.0,1.0);
setClipPlane(0.0,0.0,(2.867+o+sh)*s,0.0,0.0,-1.0);
noOutput();
nextOBJ();

/*C19(PrimaryMirrorInsert)*/
makeACone(0.0466*s,0.174*s);
setProperties(0.001,0.9);
setOrigin(0.0,0.0,(2.820+o+sh)*s);
```

```
setClipPlane(0.0,0.0,(2.857+o+sh)*s,0.0,0.0,1.0);
setClipPlane(0.0,0.0,(2.867+o+sh)*s,0.0,0.0,-1.0);
noOutput();

/*C20(PrimaryMirrorInsert)*/
makeACone(0.082*s,0.135*s);
setProperties(0.001,0.9);
setOrigin(0.0,0.0,(2.939+o+sh)*s);
setClipPlane(0.0,0.0,(2.857+o+sh)*s,0.0,0.0,1.0);
setClipPlane(0.0,0.0,(2.915+o+sh)*s,0.0,0.0,-1.0);
noOutput();

/*C21(PrimaryMirrorInsert)*/
makeACone(0.109*s,0.0509*s);
setProperties(0.001,0.9);
setOrigin(0.0,0.0,(2.831+o+sh)*s);
setClipPlane(0.0,0.0,(2.915+o+sh)*s,0.0,0.0,1.0);
setClipPlane(0.0,0.0,(2.9404+o+sh)*s,0.0,0.0,-1.0);
noOutput();

/*Precision Aperture*/
/*If number of precision apertures =1*/
/*D2 1precisionaperture*/
makeADisk(0.0,0.0,(2.9404+o+sh)*s,0.0,0.0,-1.0,0.3*s);
setProperties(0.001,0.9);
setClipPlane(0.0148*s,0.0,0.0,-1.0,0.0,0.0);
setClipPlane(0.0,0.0296*s,0.0,-1.0,-1.0,0.0);
setClipPlane(0.0,0.0296*s,0.0,1.0,-1.0,0.0);
setClipPlane(-0.0148*s,0.0,0.0,1.0,0.0,0.0);
setClipPlane(0.0,-0.0296*s,0.0,1.0,1.0,0.0);
setClipPlane(0.0,-0.0296*s,0.0,-1.0,1.0,0.0);
clipAsAHole();


/*If number of precision apertures =2*/
/*D2 2precisionapertures*/
makeADisk(0.0,0.0,(2.9404+o+sh)*s,0.0,0.0,-1.0,0.03950*s);
setProperties(0.001,0.9);
setClipPlane((0.0148+(apw+d)/2)*s,0.0,0.0,-1.0,0.0,0.0);
setClipPlane((apw+d)*s/2,0.0296*s,0.0,-1.0,-1.0,0.0);
setClipPlane((apw+d)*s/2,0.0296*s,0.0,1.0,-1.0,0.0);
setClipPlane((((apw+d)/2)-0.0148)*s,0.0,0.0,1.0,0.0,0.0);
setClipPlane((apw+d)*s/2,-0.0296*s,0.0,1.0,1.0,0.0);
setClipPlane((apw+d)*s/2,-0.0296*s,0.0,-1.0,1.0,0.0);
clipAsAHole();
setClipPlane((0.0148-(apw+d)/2)*s,0.0,0.0,-1.0,0.0,0.0);
setClipPlane(-(apw+d)*s/2,0.0296*s,0.0,-1.0,-1.0,0.0);
setClipPlane(-(apw+d)*s/2,0.0296*s,0.0,1.0,-1.0,0.0);
setClipPlane((-((apw+d)/2)-0.0148)*s,0.0,0.0,1.0,0.0,0.0);
setClipPlane(-(apw+d)*s/2,-0.0296*s,0.0,1.0,1.0,0.0);
setClipPlane(-(apw+d)*s/2,-0.0296*s,0.0,-1.0,1.0,0.0);
clipAsAHole();

/*If number of precision apertures =3*/
/*D2 3precisionapertures*/
makeADisk(0.0,0.0,(2.9404+o+sh)*s,0.0,0.0,-1.0,0.3*s);
```

```
setProperties(0.001,0.9);
setClipPlane(0.0148*s,0.0,0.0,-1.0,0.0,0.0);
setClipPlane(0.0,0.0296*s,0.0,-1.0,-1.0,0.0);
setClipPlane(0.0,0.0296*s,0.0,1.0,-1.0,0.0);
setClipPlane(-0.0148*s,0.0,0.0,1.0,0.0,0.0);
setClipPlane(0.0,-0.0296*s,0.0,1.0,1.0,0.0);
setClipPlane(0.0,-0.0296*s,0.0,-1.0,1.0,0.0);
clipAsAHole();
setClipPlane((0.0148+apw+d)*s,0.0,0.0,-1.0,0.0,0.0);
setClipPlane((apw+d)*s,0.0296*s,0.0,-1.0,-1.0,0.0);
setClipPlane((apw+d)*s,0.0296*s,0.0,1.0,-1.0,0.0);
setClipPlane((apw+d-0.0148)*s,0.0,0.0,1.0,0.0,0.0);
setClipPlane((apw+d)*s,-0.0296*s,0.0,1.0,1.0,0.0);
setClipPlane((apw+d)*s,-0.0296*s,0.0,-1.0,1.0,0.0);
clipAsAHole();
setClipPlane((0.0148-apw-d)*s,0.0,0.0,-1.0,0.0,0.0);
setClipPlane(-(apw+d)*s,0.0296*s,0.0,-1.0,-1.0,0.0);
setClipPlane(-(apw+d)*s,0.0296*s,0.0,1.0,-1.0,0.0);
setClipPlane((-apw-d-0.0148)*s,0.0,0.0,1.0,0.0,0.0);
setClipPlane(-(apw+d)*s,-0.0296*s,0.0,1.0,1.0,0.0);
setClipPlane(-(apw+d)*s,-0.0296*s,0.0,-1.0,1.0,0.0);
clipAsAHole();

/*If number of precision apertures =4*/
/*D2 4precisionapertures*/
makeADisk(0.0,0.0,(2.9404+o+sh)*s,0.0,0.0,-1.0,0.1*s);
setProperties(0.001,0.9);
setClipPlane((0.0148+(apw+d)/2)*s,0.0,0.0,-1.0,0.0,0.0);
setClipPlane((apw+d)*s/2,0.0296*s,0.0,-1.0,-1.0,0.0);
setClipPlane((apw+d)*s/2,0.0296*s,0.0,1.0,-1.0,0.0);
setClipPlane((((apw+d)/2)-0.0148)*s,0.0,0.0,1.0,0.0,0.0);
setClipPlane((apw+d)*s/2,-0.0296*s,0.0,1.0,1.0,0.0);
setClipPlane((apw+d)*s/2,-0.0296*s,0.0,-1.0,1.0,0.0);
clipAsAHole();
setClipPlane((0.0148-(apw+d)/2)*s,0.0,0.0,-1.0,0.0,0.0);
setClipPlane(-(apw+d)*s/2,0.0296*s,0.0,-1.0,-1.0,0.0);
setClipPlane(-(apw+d)*s/2,0.0296*s,0.0,1.0,-1.0,0.0);
setClipPlane((-((apw+d)/2)-0.0148)*s,0.0,0.0,1.0,0.0,0.0);
setClipPlane(-(apw+d)*s/2,-0.0296*s,0.0,1.0,1.0,0.0);
setClipPlane(-(apw+d)*s/2,-0.0296*s,0.0,-1.0,1.0,0.0);
clipAsAHole();
setClipPlane((0.0148+3*(apw+d)/2)*s,0.0,0.0,-1.0,0.0,0.0);
setClipPlane((apw+d)*3*s/2,0.0296*s,0.0,-1.0,-1.0,0.0);
setClipPlane((apw+d)*3*s/2,0.0296*s,0.0,1.0,-1.0,0.0);
setClipPlane(((3*(apw+d)/2)-0.0148)*s,0.0,0.0,1.0,0.0,0.0);
setClipPlane((apw+d)*s*3/2,-0.0296*s,0.0,1.0,1.0,0.0);
setClipPlane((apw+d)*3*s/2,-0.0296*s,0.0,-1.0,1.0,0.0);
clipAsAHole();
setClipPlane((0.0148-3*(apw+d)/2)*s,0.0,0.0,-1.0,0.0,0.0);
setClipPlane(-(apw+d)*3*s/2,0.0296*s,0.0,-1.0,-1.0,0.0);
setClipPlane(-(apw+d)*3*s/2,0.0296*s,0.0,1.0,-1.0,0.0);
setClipPlane((-((apw+d)*3/2)-0.0148)*s,0.0,0.0,1.0,0.0,0.0);
setClipPlane(-(apw+d)*s*3/2,-0.0296*s,0.0,1.0,1.0,0.0);
setClipPlane(-(apw+d)*s*3/2,-0.0296*s,0.0,-1.0,1.0,0.0);
clipAsAHole();
```

```
/*If number of precision apertures =5*/
/*D2 5precisionapertures*/
makeADisk(0.0,0.0,(2.9404+o+sh)*s,0.0,0.0,-1.0,0.03950*s);
setProperties(0.001,0.9);
setClipPlane(0.0148*s,0.0,0.0,-1.0,0.0,0.0);
setClipPlane(0.0,0.0296*s,0.0,-1.0,-1.0,0.0);
setClipPlane(0.0,0.0296*s,0.0,1.0,-1.0,0.0);
setClipPlane(-0.0148*s,0.0,0.0,1.0,0.0,0.0);
setClipPlane(0.0,-0.0296*s,0.0,1.0,1.0,0.0);
setClipPlane(0.0,-0.0296*s,0.0,-1.0,1.0,0.0);
clipAsAHole();
setClipPlane((0.0148+apw+d)*s,0.0,0.0,-1.0,0.0,0.0);
setClipPlane((apw+d)*s,0.0296*s,0.0,-1.0,-1.0,0.0);
setClipPlane((apw+d)*s,0.0296*s,0.0,1.0,-1.0,0.0);
setClipPlane((apw+d-0.0148)*s,0.0,0.0,1.0,0.0,0.0);
setClipPlane((apw+d)*s,-0.0296*s,0.0,1.0,1.0,0.0);
setClipPlane((apw+d)*s,-0.0296*s,0.0,-1.0,1.0,0.0);
clipAsAHole();
setClipPlane((0.0148-apw-d)*s,0.0,0.0,-1.0,0.0,0.0);
setClipPlane(-(apw+d)*s,0.0296*s,0.0,-1.0,-1.0,0.0);
setClipPlane(-(apw+d)*s,0.0296*s,0.0,1.0,-1.0,0.0);
setClipPlane((-apw-d-0.0148)*s,0.0,0.0,1.0,0.0,0.0);
setClipPlane(-(apw+d)*s,-0.0296*s,0.0,1.0,1.0,0.0);
setClipPlane(-(apw+d)*s,-0.0296*s,0.0,-1.0,1.0,0.0);
clipAsAHole();
setClipPlane((0.0148+2*(apw+d))*s,0.0,0.0,-1.0,0.0,0.0);
setClipPlane((apw+d)*2*s,0.0296*s,0.0,-1.0,-1.0,0.0);
setClipPlane((apw+d)*2*s,0.0296*s,0.0,1.0,-1.0,0.0);
setClipPlane((2*(apw+d)-0.0148)*s,0.0,0.0,1.0,0.0,0.0);
setClipPlane((apw+d)*2*s,-0.0296*s,0.0,1.0,1.0,0.0);
setClipPlane((apw+d)*2*s,-0.0296*s,0.0,-1.0,1.0,0.0);
clipAsAHole();
setClipPlane((0.0148-2*(apw+d))*s,0.0,0.0,-1.0,0.0,0.0);
setClipPlane(-(apw+d)*2*s,0.0296*s,0.0,-1.0,-1.0,0.0);
setClipPlane(-(apw+d)*2*s,0.0296*s,0.0,1.0,-1.0,0.0);
setClipPlane((2*(-apw-d)-0.0148)*s,0.0,0.0,1.0,0.0,0.0);
setClipPlane(-(apw+d)*2*s,-0.0296*s,0.0,1.0,1.0,0.0);
setClipPlane(-(apw+d)*2*s,-0.0296*s,0.0,-1.0,1.0,0.0);
clipAsAHole();

/*Adiskforvisualization of blur circle at precision aperture*/
makeADisk(0.0,0.0,(2.9404+o+sh)*s,0.0,0.0,-1.0,0.3*s);
setProperties(1.0,1.0);
nextOBJ();

/*Loop to vary input angles for determination of OPSF*/
for (phi=88.6; phi<90.0; phi=phi+0.1)
{
for(theta=0.0; theta < 4.5; theta=theta+0.1)
{
setSourceDir(sin(theta*PI/180.0)*sin(phi*PI/180.0),cos(phi*PI/180.0),
cos(theta*PI/180.0)*sin(phi*PI/180.0));
startRayTrace(100000);
}
}
}
```

The following code was written in FORTRAN. It is used to post process the output files generated from running the provided C code (the first eleven (11) pages of Appendix C). This particular code is used for the case in which five detectors, thus five precision apertures are placed at the focal plane of the telescope. The output files generated from this code are in a form that can be directly imported into excel, and plotted to obtain the Optical Point Spread Function at each detector. Note that all dimensions are in inches and are scaled by ten (10).

```
      PROGRAM OPSF
      IMPLICIT NONE
      REAL*8 APW,D,XPOS,YPOS,ZPOS,AP1,AP2,AP3,MAX1,MAX2,MAX3,MAXNUM1,
     $MAXNUM2,MAXNUM3
       INTEGER I,NUM1,NUM2,NUM3,LINES,J,NUMTHETA,NUMPHI,N,NUMTOTAL,COUNT
     $,NUM,L,P,R,O,C
      CHARACTER*100 FICHIER
      CHARACTER*100 SC_LET
      DIMENSION AP1(15,45), AP2(15,45), AP3(15,45),MAX1(15),
     $MAX2(15),MAX3(15)

*     Open files for output (ap1, ap2, and ap3).  Open file numberb.dat which contains the ends
*     of the file names produced by Felix's code.  Numberb.dat contains lines '001.dat', '002.dat',
*     etc. up to the number of output files produced.

      OPEN(15,FILE='numberb.dat',STATUS='OLD')
      OPEN(16,FILE='ap1.dat',STATUS='OLD')
      OPEN(17,FILE='ap2.dat',STATUS='OLD')
      OPEN(18,FILE='ap3.dat',STATUS='OLD')

*     APW is the width of the precision apertures, D is the distance between them.

      APW=0.296D0
      D=0.1D0
      NUM1=0
      NUM2=0
      NUM3=0
      N=1
      COUNT=1
      NUMTHETA=45
      NUMPHI=15
      NUMTOTAL=NUMTHETA*NUMPHI

*     Initialize the value in the arrays containing maximum response for each valueof phi (max1...),
*     initialize the maximum response of each aperture (maxnum1,...) to zero.

      DO 1 C=1,NUMPHI
      MAX1(C)=0
      MAX2(C)=0
      MAX3(C)=0
1      CONTINUE
      MAXNUM1=0
      MAXNUM2=0
      MAXNUM3=0

      DO WHILE (N.LE.NUMPHI)

      DO 10 J=COUNT,NUMTHETA*N
```

```
       NUM1=0
       NUM2=0
       NUM3=0

       READ(15,*)SC_LET

      FICHIER = 'OUTPUT'
     $  //SC_LET
       OPEN(24,FILE=FICHIER,STATUS='OLD')

*    Start a loop in which each output file is opened and read.  Each output file corresponds to a given
*    theta, phi combination (see previous C code).  When reading a given output file, each
*    line contains a set of coordinates for a ray arriving at the focal plane.  If the arriving ray falls within
*    the central aperture, the counter NUM1 is incremented.  Similarly, if it falls in the second
*    aperture, NUM2 is incremented and if it falls within the third aperture, NUM3 is incremented.


       DO 235 I=1,50000

       READ(24,*, END=30)XPOS,YPOS,ZPOS
       IF(XPOS.GT.(-APW/2.0D0).AND.XPOS.LE.0)THEN
       IF(ABS(YPOS).LT.(XPOS+0.296d0))THEN
       NUM1=NUM1+1
       END IF
       END IF

       IF(XPOS.GT.0.AND.XPOS.LT.(APW/2.d0))THEN
       IF(ABS(YPOS).LT.(0.296d0-XPOS))THEN
       NUM1=NUM1+1
       END IF
       END IF

       IF(ABS(XPOS).GT.(APW/2.d0+D).AND.ABS(XPOS)
      &.LE.(APW+D))THEN
       IF(ABS(YPOS).LT.((abs(XPOS)-(APW+D))+0.296d0))THEN
       NUM2=NUM2+1
       END IF
       END IF

       IF(ABS(XPOS).GT.(APW+D).AND.ABS(XPOS).LT.
      &(1.5D0*APW+D))THEN
       IF(ABS(YPOS).LT.(0.296d0-(ABS(XPOS)-
      &(APW+D))))THEN
       NUM2=NUM2+1
       END IF
       END IF

       IF(ABS(XPOS).GT.(1.5d0*APW+2.d0*D).AND.ABS(XPOS)
      &.LE.(2.0d0*(APW+D)))THEN
       IF(ABS(YPOS).LT.(ABS(XPOS)-(2.0d0*(APW+D))+0.296d0))
      &THEN
       NUM3=NUM3+1
       END IF
       END IF

       IF(ABS(XPOS).GT.(2.0d0*(APW+D)).AND.ABS(XPOS).LT.
```

```
    &(2.5d0*APW+2.d0*D))THEN
     IF(ABS(YPOS).LT.(0.296d0-(ABS(XPOS)-(2.0d0*
    &(APW+D)))))THEN
     NUM3=NUM3+1
     END IF
     END IF
     NUM=J-NUMTHETA*(N-1)

235   CONTINUE

30   AP1(N,NUM)=NUM1
     AP2(N,NUM)=NUM2
     AP3(N,NUM)=NUM3

10   CONTINUE

     COUNT=J
     N=N+1
     END DO

*    Determine the maximum response within each of the detectors

     DO 60 R=1,NUMPHI

     DO 70 P=1,NUMTHETA
     IF (AP1(R,P).GT.MAX1(R)) THEN
     MAX1(R)=AP1(R,P)
     END IF
     IF (AP2(R,P).GT.MAX2(R))THEN
     MAX2(R)=AP2(R,P)
     END IF
     IF (AP3(R,P).GT.MAX3(R))THEN
     MAX3(r)=AP3(R,P)
     END IF
70   CONTINUE
60   CONTINUE

     DO 80 O=1,NUMPHI
     IF (MAX1(0).GT.MAXNUM1) THEN
     MAXNUM1=MAX1(O)
     END IF
     IF (MAX2(O).GT.MAXNUM2) THEN
     MAXNUM2=MAX2(O)
     END IF
     IF (MAX3(O).GT.MAXNUM3) THEN
     MAXNUM3=MAX3(O)
     END IF
80   CONTINUE

*    Write the output for the Optical Point Spread Function for each detector, normalized
*    by the maximum response within all detectors (maximum response will be at central
*    detector.

     DO 50 L=1,NUMTHETA

     WRITE(16,200)AP1(15,L)/maxnum1,AP1(14,L)/maxnum1,
```